



Thin film growth by combinatorial epitaxy for electronic and energy applications

Deepak Kumar

► To cite this version:

Deepak Kumar. Thin film growth by combinatorial epitaxy for electronic and energy applications. Material chemistry. Normandie Université, 2019. English. NNT : 2019NORMC255 . tel-02518523

HAL Id: tel-02518523

<https://theses.hal.science/tel-02518523>

Submitted on 25 Mar 2020

HAL is a multi-disciplinary open access archive for the deposit and dissemination of scientific research documents, whether they are published or not. The documents may come from teaching and research institutions in France or abroad, or from public or private research centers.

L'archive ouverte pluridisciplinaire **HAL**, est destinée au dépôt et à la diffusion de documents scientifiques de niveau recherche, publiés ou non, émanant des établissements d'enseignement et de recherche français ou étrangers, des laboratoires publics ou privés.



Normandie Université

THÈSE

Pour obtenir le diplôme de doctorat

Spécialité CHIMIE

Préparée au sein de l'Université de Caen Normandie

Thin film growth by combinatorial epitaxy for electronic and energy applications

**Présentée et soutenue par
Deepak KUMAR**

**Thèse soutenue publiquement le 19/12/2019
devant le jury composé de**

M. MANUEL BIBES	Directeur de recherche au CNRS, Université Paris-Saclay	Rapporteur du jury
M. NIELS KELLER	Directeur de recherche au CNRS, Université de Versailles Saint-Quentin	Rapporteur du jury
M. ADRIAN DAVID	Maître de conférences HDR, Université Caen Normandie	Membre du jury
M. ARNAUD FOUCHET	Chargé de recherche au CNRS, ENSICAEN	Membre du jury
Mme MARYLINE GUILLOUX-VIRY	Professeur des universités, Université Rennes 1	Président du jury

Thèse dirigée par WILFRID PRELLIER, Laboratoire de cristallographie et sciences des matériaux (Caen)



UNIVERSITÉ
CAEN
NORMANDIE



Epitaxial strain-engineered structural and magnetic
properties of PrVO_3 thin films for spintronics
applications

Deepak Kumar

December 20, 2019

The Universe is not only queerer

than we suppose,

but queerer than we can suppose

- J. B. S. Haldane

Acknowledgements

Being thankful to someone is easy, but to put it into words always remains a hard job. However, we must always find time to stop and thank the people who make difference in our lives. I had this privilege for the past three years to meet and discuss with the beautiful minds of CRISMAT laboratory.

I am very honored that Mr. Manual Bibes, Director of research CNRS, UMP Thales, Orsay and Mr. Niels Keller, Director of research CNRS, GEMAC, Versailles, have accepted to be the rapporteurs of this thesis work. My humble gratitude goes to the other jury members as well, Madame Maryline Guilloux-Viry, Professeur at the Université Rennes 1, Mr. Adrian David, associate professor at Université of Caen, Mr. Arnaud Fouchet, Chargé de recherche at CRISMAT, CNRS, and Mr. Wilfrid Prellier, Director of research at CNRS, Université Caen, to have accepted to examine this thesis work.

Once more, my sincere thank to Mr. Wilfrid Prellier, the director of CRISMAT laboratory, who welcomed me and agreed to be my thesis supervisor. His constant support in crucial times, trust, morning scientific discussions at the cafeteria made it possible to work efficiently. I again thank Mr. Adrian David and Mr. Arnaud Fouchet for their boundless fruitful discussions and invaluable assistance throughout these years.

I am grateful to all the researchers, doctrant, permanent staffs of CRISMAT, especially thin film group, for their all help in carrying out this work. My warm thanks also goes to my office colleagues for their humorous discussions over coffee breaks.

Contents

1	HISTORY OF CORRELATED PEROVSKITES: ABO_3 IN A NUTSHELL	11
1.1	Presentation of the perovskite family: RVO_3 as a special case	12
1.1.1	ABO_3 : Physical properties, distortion	12
1.1.2	RVO_3 : Structure and magnetic properties	16
1.2	Basic physics to understand the thesis	19
1.2.1	Magnetic moment dynamic	19
1.2.2	Ferromagnetism and Antiferromagnetism in short	22
1.2.3	Magnetic anisotropy	24
1.2.4	Epitaxial strain: Compressive and tensile strain	26
1.3	PrVO_3	28
1.3.1	Bulk PrVO_3	28
1.3.2	Effect of doping	29
1.3.3	The perovskite oxide thin films: Interfacial effect	31

2	EXPERIMENTAL TECHNIQUES: GROWTH AND CHARACTERIZATION OF THIN FILMS	41
2.1	Thin film elaboration	42
2.1.1	Typical growth modes of thin film	43
2.1.2	Pulsed Laser Deposition (PLD)	44
2.1.3	Growth conditions	46
2.2	Characterization techniques	47
2.2.1	Structural characterization techniques	47
2.2.2	Atomic Force Microscopy (AFM)	55
2.2.3	X-ray Photoelectron Spectroscopy (XPS)	56
2.2.4	Physical Property Measurement System (PPMS)	57
2.2.5	Superconducting Quantum Interference Device (SQUID) magnetometer	60
2.2.6	Magnetism of Reference substrates	64
3	STRAIN ENGINEERING IN PrVO_3 THIN FILMS: USING STO, LSAT, LAO, YAO SUBSTRATES	72
3.1	Prerequisite	72
3.1.1	Preliminary growth conditions	73
3.1.2	Derivation of lattice misfit	74
3.2	Preliminary structural analysis by XRD	75

3.2.1	<i>Out-of-plane</i> structure	77
3.2.2	<i>In-plane</i> structure	78
3.3	Study of microstructure by TEM: Determination of the epitaxial relationship . .	81
3.4	Resistivity measurements	83
3.5	Magnetic properties	84
3.5.1	Hysteresis cycles	84
3.5.2	Magnetic orderings in PrVO ₃ films: <i>MT</i> measurements	88
3.6	DFT calculations	93
3.7	Conclusions and perspectives	97
4	STRAIN ENGINEERING IN PrVO₃ THIN FILMS: FILM THICKNESS AND CRYSTAL ORIENTATION DEPENDENCE	100
4.1	Strain engineering via changing PrVO ₃ film thickness	101
4.1.1	Growth conditions	101
4.1.2	Preliminary structural observations by XRD	102
4.1.3	Magnetic properties	107
4.2	Crystal surface orientation dependent properties of PrVO ₃ films	119
4.2.1	Growth conditions	119
4.2.2	Structure	120
4.2.3	Strain controlled epitaxial stabilization	127

4.2.4	Magnetic properties	128
5	CONCLUSIONS AND OUTLOOK	141
6	ANNEX A	153
6.1	Calculation of uncertainty in the estimation of lattice constants	153

INTRODUCTION

For the past few centuries human beings have studied the effects of pressure (hydrostatic strain) on the properties of materials. Only a few decades ago, it was shown that the biaxial strain, where a film is clamped to the substrate but free in out-of-plane direction, can alter the superconducting transition temperature [1]. Since then, the exploitation of this novel technique of *strain engineering in epitaxial thin films* has increased exponentially through these years in several areas of condensed matter physics. The epitaxial strain imparted by the substrate not only tunes the functional properties of a thin film, but also unveils many novel hidden correlated phenomena. The strain engineering of perovskite thin films is typically realized through the choice of a substrate which imposes its lattice parameter unto the film through coherent epitaxy. Depending upon the lattice misfit, the strain experienced by the film can also be accommodated by rotating or tilting the oxygen octahedra, which is the most important part of the crystal lattice in perovskites. Thus, any modification in the octahedral cage would change the electron hopping from one d -orbital to the other, leading to change in the physics and chemistry of the material. Exploring the strain predictions, nowadays, is greatly simplified by the development of the new substrates with perovskite crystal structure. The downside is that, any desired strain requires its own substrate, and thus large cost. An alternative is to grow epitaxial thin films of varying thickness on just one substrate material. Nevertheless, the latter technique is prone to create local dislocations in the film, whose density typically varies with film thickness. To achieve the highly-strained films free of such dislocations, one needs to keep them thin, below a critical thickness limit determined by Mathews and Blakeslee [2]. The use of this pioneering technique

of *strain engineering* has been reported by many semiconductor manufacturers, such as IBM and Intel. The strain engineering is used in the Complementary Metal-Oxide-Semiconductor (CMOS) technologies, as the P-type MOS (PMOS) performance is best served when applying compressive strain to the channel, and N-type MOS (NMOS) receives benefit from the tensile strain.

This thesis work falls in the vicinity of physics of condensed matter, and includes a small contribution of chemistry. I have devoted most of my studies on the synthesis of PrVO_3 thin films, on various commercially available single crystal substrates, their structural and magnetic characterization. Thus, the framework of this thesis is arranged in the four principal parts.

The first part is dedicated to the presentation of the scientific context of this thesis, namely, study of the perovskite-type compounds, their lattice distortion, generalities of the PrVO_3 compound in bulk, effects of doping in the bulk PrVO_3 compound, PrVO_3 as a thin film, and finally, the chemical strain engineering in PrVO_3 films by monitoring the contents of oxygen vacancies.

The second part deals with the experimental techniques involved in the thesis work, and presents in detail the working principles of the techniques.

The third part of the manuscript aims to present the strain engineering in PrVO_3 thin films by growing films on various single crystal substrates, and presents the strain-dependent structural and magnetic properties of PrVO_3 films. Strong correlations between structural and magnetic properties of the PrVO_3 films are also established. Finally, the DFT calculations performed to validate the experimental results are also discussed.

The fourth part of the thesis is divided into two principal sections: The first one aims to present the film thickness-dependent structural and magnetic properties of PrVO_3 thin films. A strong paramagnetic-like response of thinner films, and a double-hysteresis (with two magnetic phases) ferromagnetic-like behavior of thick films, is extracted and explained by using a “dead-layer” present at the surface of the film. These results are further confirmed by the XPS of a 50 nm thin film, which clearly shows a gradient in the valence state of V. The second one details the growth of PrVO_3 films on SrTiO_3 substrates with different surface orientations. The study reveals a whopping enhancement of magnetization in PrVO_3 films when the substrate orientation is changed from SrTiO_3 (001) to SrTiO_3 (111). A strong perpendicular magnetic anisotropy and

uniaxial anisotropy presented by the films are also discussed.

Chapter 1

HISTORY OF CORRELATED PEROVSKITES: ABO_3 IN A NUTSHELL

The objective of this chapter is to present the scientific context on which this thesis is build upon. This chapter begins with an overview of the perovskites including their crystallographic structure, physical properties, followed by the presentation of PrVO_3 (PVO), a compound predominantly studied in this thesis. Finally, it ends with the exploration of the effects of interface in vanadate thin films, and the preliminary case of PVO thin films grown on SrTiO_3 (STO) substrate is discussed in detail.

1.1 Presentation of the perovskite family: RVO_3 as a special case

The perovskites acquire their name from the calcium titanium oxide ($CaTiO_3$) structure, which was first discovered in the Ural mountains of Russia by Gustav Rose in 1839 and named after a Russian nobleman, mineralogist Count Lev Aleksevich Von Perovski [3, 4].

The perovskites acquire the general formula ABX_3 , where A and B are cations of different sizes, and X is an anion, which is often oxygen but can also be replaced by large ions such as halides, sulphides and nitrides [5]. The perovskites broadly exist in various forms *viz.* ABO_3 perovskite (ex: $SrTiO_3$, $CaTiO_3$), A_2BO_4 layered perovskite (ex: Sr_2RuO_4), $A_2BB'O_6$ double perovskite (ex: Ba_2TiRuO_6), and $A_2A'B_2B'O_9$ triple perovskite (ex: $La_2SrCo_2FeO_9$), etc [6, 7, 8, 9]. Nevertheless, since my thesis work on $PrVO_3$ compound is mostly related to the ABO_3 -type perovskite class, I would primarily emphasize on ABO_3 perovskite structure, their physical properties, deformation and so on.

1.1.1 ABO_3 : Physical properties, distortion

Due to their simple crystal structure and great potential for a variety of device applications, the ABO_3 perovskites have been investigated experimentally and theoretically in the last few years [10, 11, 12, 13]. From the structural point of view, the ideal ABO_3 perovskite refers to the cubic crystal structure $Pm\bar{3}m$, so called *aristotype*, and is composed of a three-dimensional network of corner sharing BO_6 octahedra. The atomic arrangements in ABO_3 type perovskite oxide structure are shown in Fig. 1.1, where A and B are cations, and O is the anion. The A site cation is typically larger than B cation.

In general, the A cation is surrounded by twelve oxygen anions, and located in the center of the cube at position $(1/2, 1/2, 1/2)$. The B cations are located at the corners of the cube, and at the center of BO_6 octahedra. Whereas, the O anions are placed at the centers of the twelve cube edges, giving corner-shared strings of BO_6 octahedra (Fig. 1.1). The ideal ABO_3 perovskite

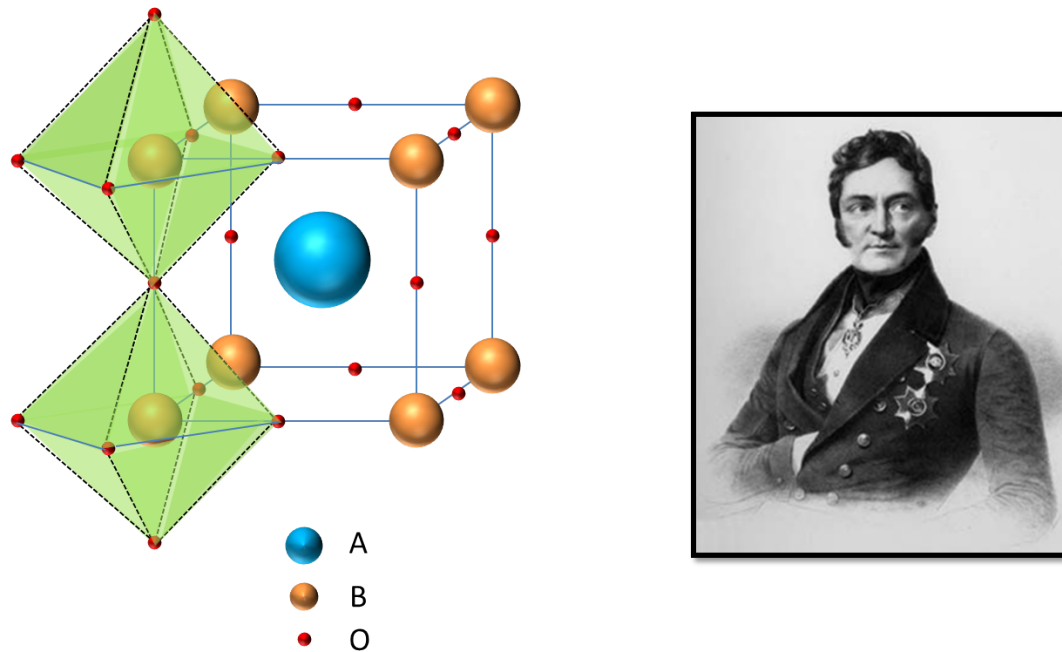


Figure 1.1: Representation of an ideal ABO_3 perovskite structure, along with Lev Aleksevich von Perovski.

structure can also undergo deformations leading to derived structures, routinely called as the *hettotypes* [14].

Distortion of octahedra

While the perovskites were in their infancy, the founder of the science of crystal chemistry, V.M. Goldschmidt, studied a large number of synthetic perovskites with different compositions, and established the principles of material synthesis. Later, he established a factor, which determines how far from ideal packing can the ionic sizes move, and still be “tolerated” by the perovskite structure, widely known as the *tolerance factor* (tf), and follows as [15]

$$tf = \frac{(r_A + r_O)}{\sqrt{2}(r_B + r_O)} \quad (1.1)$$

Where, r_A , r_B , and r_O are the ionic radii of cations A, B and anion O, respectively. Geometrically speaking, when tf is equal to one, an ideal cubic perovskite structure is formed (ex: $SrTiO_3$). On the other hand, if value of tf is far from one, crystal structure of lower symmetry is formed (ex: $PrVO_3$, orthorhombic with $tf \sim 0.94$). It has been suggested that, this lowering in symmetry often results from the distortion of octahedron, which occurs because the ionic radius of A-site is too small to fully occupy the available volume. As shown by Glazer in the early 70s, that depending on the nature of cations A and B, all perovskite-type compounds adopt the derived and deformed structures, with respect to the cubic perovskite $Pm\bar{3}m$.

The deformation of octahedron generally has several causes: (1) Off-centering of the cations, (2) Rotation of BO_6 octahedron, (3) Jahn-Teller deformations in the BO_6 octahedron (Fig. 1.2). The off-centering mainly occurs due to larger A and smaller B ion, which leads to a contraction of BO_6 octahedron. On the other hand, octahedral rotation typically occurs in the case where A cation is too small for cubic BO_6 corner-sharing network. The Jahn-Teller distortion often occurs in every perovskites that contain orbitally degenerate electronic state in transition metal cation B. Nevertheless, the major deformation in the perovskites is the rotation of octahedron, which has direct impact on the electronic properties of the material. This is due to the fact that octahedral

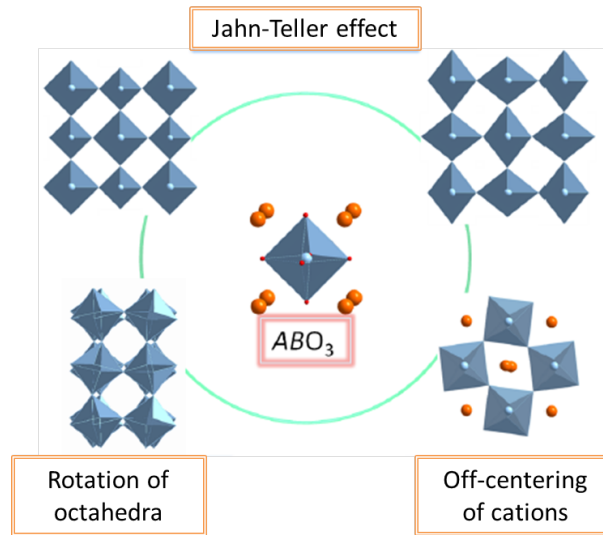


Figure 1.2: Various deformations within the perovskite family.

rotations influence the B–O bond length and B–O–B bond angle due to shift of oxygen ions from the edges of cubic perovskite structure.

The octahedral rotation can efficiently be described by the Glazer notations [17]. This notation includes two factors: the first one determines the amplitude of rotation, and second, the angle of rotation of the octahedra. First, the amplitude of rotation is described in terms of pseudocubic a , b , c , reference structure as in $a^n b^n c^n$ nomenclature. A similar letter in $a^n b^n c^n$ notation signify an equal degree of octahedral rotation. For instance, aaa means that the angles α , β and γ have the same values, aba means α and γ have same values, but β is different. Second, the phase of rotation is classified in terms of $n = +$ or $-$, where, “+” means an in-phase rotation of octahedron with respect to others along the same axis, and “-” means antiphase rotation (Fig. 1.3). For example, $a^+ a^+ c^-$ means that the octahedral rotation around a and b pseudo-cubic axis is similar, and is in-phase, relative to each other, whereas rotation around c axis is different and is out-of-phase with the other two axes. In some cases, the value of n can be 0 (zero) and represents no

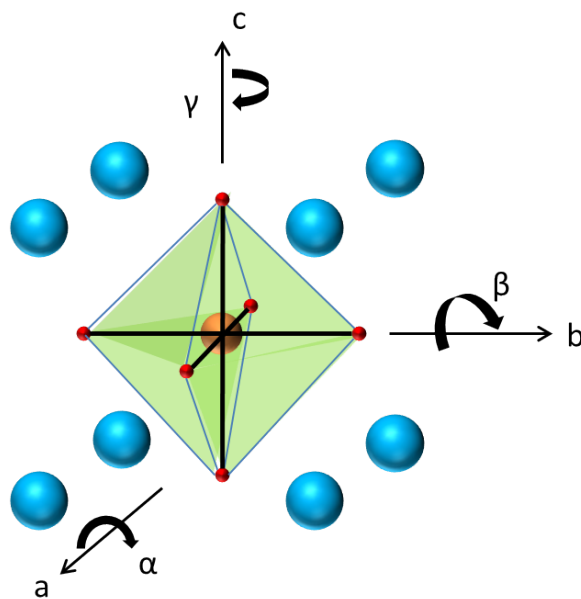


Figure 1.3: Schematic representation of rotation of oxygen octahedron around the pseudocubic axes, a , b , and c .

octahedral rotation at all (ex. $SrTiO_3$).

So far, we have discussed the perovskites in general, their basic properties, the “rules” that govern a kind of octahedral distortion, based on the *tolerance factor*, that eventually determines the crystal structure. In the next section, I will narrow the discussion to the rare earth vanadates, RVO_3 , which is a salient part of my thesis, and described as special case of ABO_3 perovskites.

1.1.2 RVO_3 : Structure and magnetic properties

RVO_3 compounds referred to rare earth vanadates, where, cation A is replaced by a large rare earth element, R, and cation B by vanadium (V). Both the cations in RVO_3 perovskite exist in 3+ valence states, which makes them $3d^2$ orbital system, because two electrons are present in the outermost shell of V^{3+} ion. The RVO_3 -type perovskites are often Mott insulator due to V^{3+} ionic state, whereas, on the contrary, V^{4+} perovskites generally have metallic character, for example $SrVO_3$. In the periodic table, the rare earth elements (also called rare earth metals) are located on the bottom, ranging from Lanthanum (La) to Lutetium (Lu), electronic configuration $[Xe] 4f^0 6s^2$ (La) to $[Xe] 4f^{14} 6s^2$ (Lu), where [Xe] is Xenon.

Structure of RVO_3 based compounds

In practice, perovskite-type vanadium oxides RVO_3 have a $Pbnm$ orthorhombic crystal structure with lattice constants of $a \sim b \sim c/\sqrt{2}$ at room temperature [67, 19, 20]. The core of physics in RVO_3 perovskite system that provoke intriguing phenomena is the so called collective Jahn-Teller distortion [21, 22]. According to Jahn-Teller theorem, a non-linear molecule with degenerate electronic states cannot be stable, unless it undergoes structural distortion to remove the degeneracy. The V^{3+} cation has two electrons in d atomic orbital, making them $3d^2$ orbital, or t_{2g}^2 orbital by means of crystal field. Accordingly, V^{3+} is Jahn-Teller active and must undergo distortion in order to remove the degeneracy and lower the system energy. This will consequently

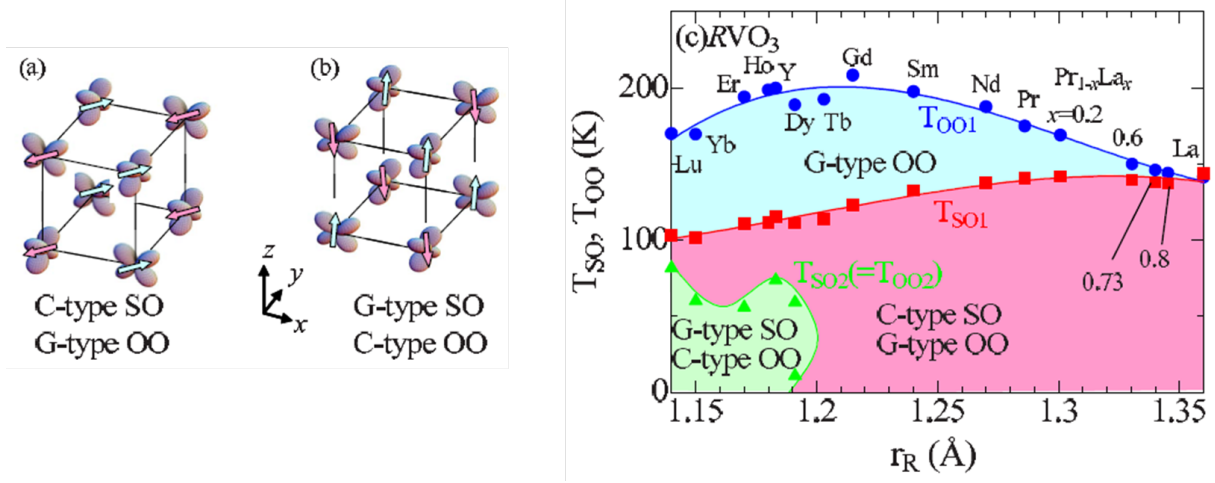


Figure 1.4: Schematic representation of (a) C-type SO and G-type OO, (b) G-type SO and C-type OO, (c) spin-orbital phase diagram of RVO_3 [19].

favor a lower symmetry structure. Therefore, an RVO_3 - a Jahn-Teller active system, undergoes a structural deformation from orthorhombic $Pbnm$ to lower symmetric monoclinic $P2_1/b$ at temperature, $T = 141$ K–200 K. This structural deformation is mainly due to the tilting of VO_6 octahedra. The outcome of this distortion is that, one electron of the t_{2g} orbital occupies the d_{xy} atomic orbital and the other, either d_{yz} , or, d_{zx} orbital, simply a rearrangement of orbitals to lower energy.

Magnetic properties

All RVO_3 compounds undergo distinct spin ordering (SO) and orbital ordering (OO) depending upon the ionic radii of R cation (r_R) [67, 19, 23, 24, 25, 26]. In particular, as temperature is decreased from 300 K, all RVO_3 compounds experience a structural phase transition from $Pbnm$ orthorhombic to $P2_1/b$ monoclinic crystal structure, accompanied with the G-type OO at T_{oo} , and also a magnetic transition from paramagnetic state to antiferromagnetic C-type SO at T_{so} . A schematic representation of (a) C-type SO and G-type OO, and (b) G-type SO and C-type OO is shown in Fig. 1.4. The C-type SO represents scenario, where V^{3+} spins are

antiferromagnetically aligned in ab plane, and ferromagnetically along c -axis, whereas in G-type SO, spins are aligned in a staggered way along all orthogonal directions.

These aforementioned SO and OO in RVO_3 robustly depend upon the radii r_R . Typically, as r_R increases from Lu to La, the GdFeO_3 -type orthorhombic distortion decreases, along with a suppression of VO_6 octahedra tilting, and Jahn-Teller distortion [67]. The decreasing V–O–V bond angle distortion leads to enhancement of the transfer or exchange intergral, J , in exchange energy term, $U = -2JS_i \cdot S_j$, increasing the magnetic and orbital exchange interaction between the nearest neighbour V - site [27]. This is illustrated in Fig. 1.4 (c), where the magnetic C-SO temperature increases, as r_R is changed from Lu to La.

The RVO_3 perovskites with smaller r_R , such as $\text{R} = \text{Dy}$ to Lu , and Y , exhibit additional G-type spin ordering at lower temperature in their ground state. By Analogy, G-type SO is accompanied by the C-type OO, and the structure changes back from the intermediate-temperature $P2_1/b$ monoclinic to a lower temperature $Pbnm$ orthorhombic symmetry.

1.2 Basic physics to understand the thesis

In this section of the chapter, we familiarize with few fundamental physics concepts that have been used throughout the thesis.

1.2.1 Magnetic moment dynamic

In this part, we discuss the classical expression of spin-orbit coupling, the dynamic of magnetic moment for a single spin and extend it to a whole system to explain the magnetization.

Spin-Orbit coupling

Imagine an electron in orbit around the proton (nucleus), from the electron point of view, the proton is revolving around it. The positively charged proton creates a magnetic field \mathbf{B} in the electron frame, which exerts a torque on the spinning electron, tending to align magnetic moment (μ) of electron in the direction of field. The energy associated with this torque is given by Hamiltonian H [28]:

$$H = \mu \cdot B \quad (1.2)$$

Magnetic dipole moment of electron

Consider a charge q smeared out around a ring of radius r , which rotates around the axis with time period T (Fig. 1.5). Then, the magnetic moment of electron,

$$\mu = I \cdot A$$

where, $I = q/T$ is current, and $A = \pi r^2$ is area. Therefore,

$$\mu = -\frac{q\pi r^2}{T} \quad (1.3)$$

Also, the magnetic dipole moment of a spinning charge is related to its spin angular momentum

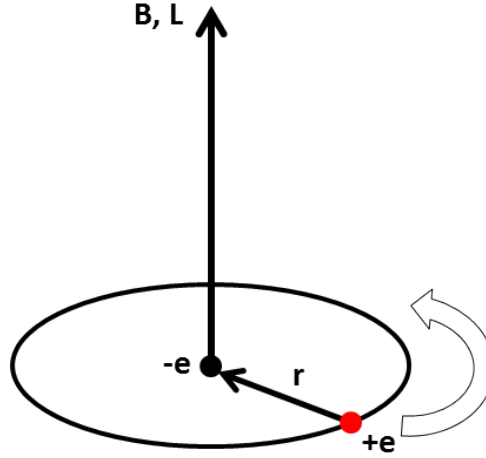


Figure 1.5: The proton, from electron's perspective.

S. If mass of ring is m , then S can be defined as the product of moment of Inertia (mr^2) and angular velocity ($2\pi/T$), i.e

$$S = \frac{2\pi mr^2}{T} \quad (1.4)$$

By simplification, the classical expression of magnetic dipole moment of electron becomes (from equation 1.2)

$$\mu = -\frac{q}{2m} \cdot S$$

But, the actual electron's magnetic moment is twice the classical answer,

$$\mu = -\frac{q}{m} \cdot S \quad (1.5)$$

Magnetic field produced by orbiting proton: intrinsic field

If we picture the proton (from electron's perspective) as a continuous current loop (Fig. 1.5), then magnetic field produced by proton can be derived using the Biot-Savart law [29]:

$$B = \frac{\mu_0 I}{2r}$$

Therefore, by simplifying and using the orbital angular momentum of electron, $L = 2\pi mr^2/T$ (similar to spin momentum), and relation $c = 1/\sqrt{\mu_0 \cdot \epsilon_0}$, where, μ_0 , ϵ_0 are the magnetic permeability, electrical permittivity of space.

$$B = \frac{1}{4\pi\epsilon_0} \frac{q}{mc^2r^3} \cdot L \quad (1.6)$$

Hence, **the spin-orbit interaction** term (from equation 1.1):

$$H = \frac{e^2}{4\pi\epsilon_0} \frac{1}{m^2c^2r^3} L \cdot S \quad (1.7)$$

This is the typical classical expression of Hamiltonian associated with spin-orbit coupling, derived assuming the electron at rest and proton presses around it. However, from a quantum mechanical point of view, that is not true, because the Hamiltonian H does not commute with L and S , and therefore spin and angular momentum are not separately conserved.

From the single spin to magnetic moment

As described in the previous section, the magnetic moment of an electron associated with its spin is $\mu_s = -\frac{q}{m} \cdot S$ (equation (1.5)), and can be written as:

$$\mu = \gamma S \quad (1.8)$$

where, γ is called the **gyromagnetic ratio** of the electron.

Therefore, the magnetization vector of a spin assembly in a volume V can be derived from the magnetic moment of single spins within this assembly:

$$M = \frac{\sum \mu}{V} \quad (1.9)$$

When a magnetic moment is placed in magnetic field, it behaves like magnetic dipole and experiences a torque (τ), given by:

$$\tau = \mu \times B = \frac{dS}{dt} \quad (1.10)$$

Also, since magnetic moment (μ) is proportional to the spin angular momentum (S) of electron. From equation (1.7),

$$\frac{d\mu}{dt} = \gamma \cdot \frac{dS}{dt}$$

Hence,

$$\frac{d\mu}{dt} = \gamma \cdot (\mu \times B) \quad (1.11)$$

The above equation / set of equations $(\frac{d\mu_x}{dt}, \frac{d\mu_y}{dt}, \frac{d\mu_z}{dt})$ are known as the Bloch equations, and describe the motion of magnetic moment under an external magnetic field.

So far, we have discussed about the spin-orbit interaction and motion of magnetic moment under an external magnetic field. We saw that the basic unit of magnetism is so-called magnetic moment, and expressed in terms of the Bohr magneton, described by $\mu_B = eh\hbar/2m = 9.27 \times 10^{-24}$ Joule/Tesla, just as e is the natural unit of electric charge. In next section, we will see, how the orientation of magnetic moments of all electrons in an atom fabricates different magnetic materials.

1.2.2 Ferromagnetism and Antiferromagnetism in short

Atoms contain many electrons, each spinning about its own axis, and moving in its own orbit. The magnetic moment associated with each kind of motion is a vector quantity, parallel to the axis of spin and normal to the plane of the orbit, respectively. The magnetic moment of the atom is the vector sum of all its electronic moments, and two possibilities arise:

- (1) The magnetic moments of all the electrons are so oriented that they cancel out each other, and atom as a whole has zero net magnetic moment. Such atoms are typically known as diamagnetic atoms.
- (2) The cancellation of the electronic moments is only partial, and atom has a net magnetic moment. Such atoms are called magnetic atoms, for example, paramagnetic, ferromagnetic, ferromagnetic, antiferromagnetic etc.

Here, we describe only two categories of magnetism which are relevant to my thesis *i.e* ferromagnetism and antiferromagnetism.

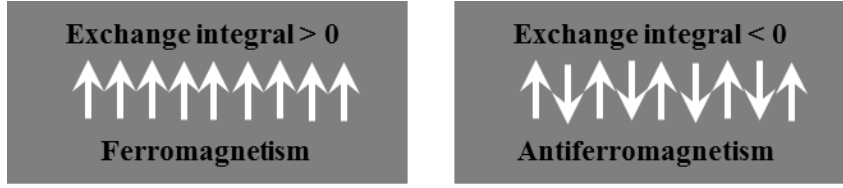


Figure 1.6: Spin moments in ferromagnets and antiferromagnets.

Ferromagnetism

In simple terms, the atomic moments in these materials are aligned parallel to each other, and the material as a whole has a spontaneous magnetic moment, *i.e.*, a magnetic moment even in zero applied magnetic field. To explain this, Pierre Weiss in 1906 made two brilliant postulates that helped to understand why ferromagnetic materials behave the way they do. First, there is an exchange field / molecular field (H_m) present in a ferromagnetic material, that is proportional to the magnetization of the sample by the relation $H_m = \lambda M$, where λ is molecular field constant. Weiss showed that λ can also be described in terms of the Curie temperature of the material as $T_c = C\lambda$, where C is the Curie constant. Therefore, the strength of molecular field can be estimated, if T_c and C are known. There is, also, a strong quantum mechanical force between these moments, often called *exchange interaction* and governed by the Heisenberg model. According to this model, the energy of interaction between atoms i, j , bearing electron spins S_i, S_j is given by:

$$U = -2JS_i.S_j$$

where, J is the exchange integral and is related to the overlap of the charge distribution of the atoms i, j (Fig. 1.6). The Second postulate was that, a ferromagnet in the demagnetized state is divided into a number of small regions called domains. Each domain is spontaneously magnetized to the saturation value M_s , but the directions of magnetization of the various domains are such that the specimen as a whole has no net magnetization. When the applied magnetic field is high enough to rotate all the magnetic domains parallel to the applied field, the material is saturated.. [30, 31]

Antiferromagnetism

In an antiferromagnet, the magnetic moments are ordered in an antiparallel arrangement, with zero net magnetic moment below the ordering temperature (Fig. 1.6). Although, a spin canting often causes a net magnetization to develop, and such materials are commonly known as canted-antiferromagnets.

1.2.3 Magnetic anisotropy

The *magnetic anisotropy* in simple terms means that the magnetic properties depend on the direction in which they are measured. There are typically four kinds of anisotropy in a material, and any one may become predominant in special circumstances.

1. Crystal anisotropy:

An anisotropy caused by the crystalline structure of the material is called crystal anisotropy, or formally the *magnetocrystalline anisotropy*. It is an intrinsic property of material and can be seen by measuring magnetization curves along different crystal directions. This anisotropy is mainly due to the so-called *spin-orbit coupling*. When an external field tries to reorient the spin of an electron, the orbit of that electron also tends to be reoriented. But, the orbit is strongly coupled to the lattice, and therefore resists the attempt to rotate the spin axis. The energy required to rotate the spin system of a domain, far from the easy direction (called the anisotropy energy), is just the energy required to overcome the spin-orbit coupling.

Fig. 1.7 illustrates a typical situation, where for zero applied field, the magnetization M would point along an axis, called easy axis. When field is applied, the magnetization is pulled up by field and down by anisotropy. In such case, the energy of magnetization is given by [31]:

$$E = K \sin^2 \alpha - \mu_0 M H \cos(\beta - \alpha) \quad (1.12)$$

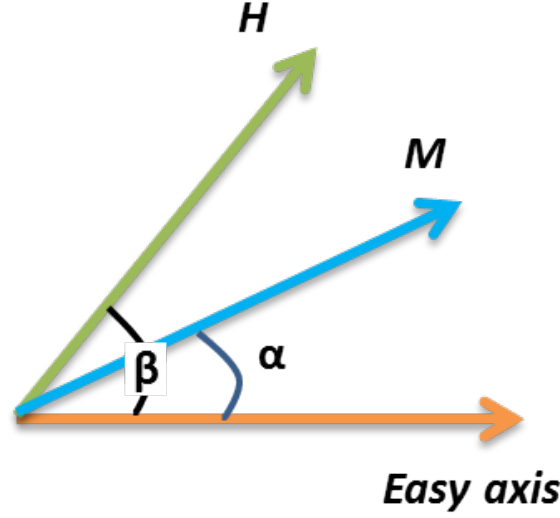


Figure 1.7: Schematic representation of applied field H , magnetization M , and the crystallographic easy axis

Where, α and β are the angle made by magnetization and applied field with the easy axis, respectively. The first term is the anisotropy energy, where, K is the anisotropy constant. The second term is Zeeman energy, and is due to applied magnetic field.

2. **Shape anisotropy:**

An isotropy caused by the asymmetric shape of the sample is called *shape anisotropy* (for example, in thin films). The energy associated with this anisotropy prefers the magnetization to lie along the long side of the sample. Therefore, to change the magnetic anisotropy from in-plane to out-of-plane, the shape anisotropy has to be compensated. This anisotropy is proportional to the magnetic moment of the material,

$$K_{shape} = -\frac{\mu_0 M_s^2}{2}$$

3. **Magnetoelastic anisotropy:**

The magnetoelastic effect is related to the spin-orbit interaction. As seen before, the spin moments are coupled to the lattice via the orbit electrons, by applying stress on the magnetic materials, the distance between atoms can be disturbed and therefore the interaction

energies. This type of anisotropy is well known in thin films where the strain is produced via lattice mismatch between film and substrate. The film elongates along one side, and the interatomic length becomes anisotropic. When out-of-plane stress is large enough, it can overcome the shape anisotropy of a thin film, and forces the magnetization of the sample to rotate along out-of-plane direction. The inherent stress/strain is the cause of this anisotropy.

1.2.4 Epitaxial strain: Compressive and tensile strain

In general, a single crystal material can be grown on top of a substrate of similar material (homoeptaxy), or, different material (heteroeptaxy). In heteroeptaxy growth, the difference in the lattice constant between the heterojunction constituent materials is referred to lattice mismatch, and is usually accommodated by building stress and dislocation defects etc, inside the grown material (film). The stress (σ) in thin film is further related to the residual strain (ϵ) via Young's modulus γ , by expression $\sigma = \gamma\epsilon$, and the nominal lattice mismatch between two material is given by:

$$\delta = \frac{a_s - a_f}{a_s} \quad (1.13)$$

where, a_s and a_f are the lattice constants of substrate and film, respectively. Note that the “lattice mismatch” is essentially the difference in lattice constants between two materials, and should not be confused with residual strain, which is actually a consequence of lattice mismatch, just as misfit dislocations are a result of lattice mismatch. The “lattice strain” (ϵ) is simply the “actual deformation” in the thin film, caused by the lattice mismatch (δ), and $\epsilon < \delta$ should always hold for a defect-free film.

From equation (1.13), if a_s is less than a_f , it produces $\delta < 0$, meaning that the film undergoes *in-plane* **compressive strain** (Fig. 1.8a). On the other hand, if a_s is bigger than a_f , producing $\delta > 0$ and means that film undergoes an *in-plane* **tensile strain** (Fig. 1.8b).

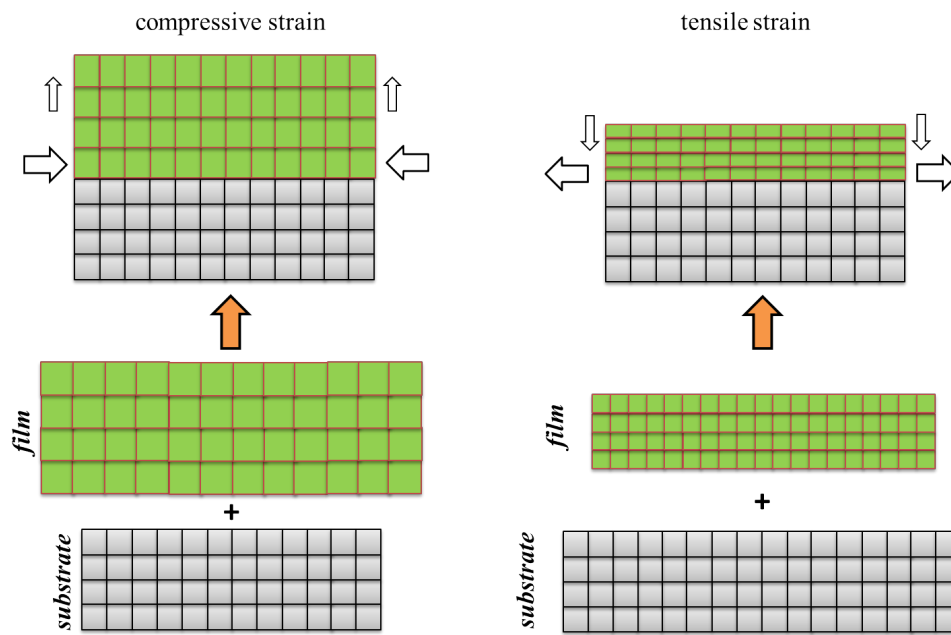


Figure 1.8: Schematic illustration of (a) compressive and (b) tensile strains. The unfilled arrows in the upper schematics represent the direction in which unit cell is moving when strained.

1.3 PrVO_3

One of the main objective of my thesis is the synthesis of the PrVO_3 in the form of thin film. In this section, we present the physical properties of PrVO_3 in the bulk form, and study its behavior when doped with other cations of similar size. Finally, we conclude the chapter with a discussion on PrVO_3 films grown under epitaxial strain.

1.3.1 Bulk PrVO_3

Structure

The first study on this compound was essentially carried out in 90's for a polycrystalline specimen [32], synthesized using the solid state reaction method, followed by its first characterization by X-ray powder diffraction. At room temperature, this compound crystallizes in an orthorhombic symmetry (space group $Pbnm$, # 62), (similar to GdFeO_3 perovskite), with $a = 5.4843 \text{ \AA}$, $b = 5.5744 \text{ \AA}$, and $c = 7.7598 \text{ \AA}$. It was reported that, PrVO_3 also undergoes a structural modification at temperature $T_s \sim 180 \text{ K}$, from an orthorhombic $Pbnm$ to monoclinic $P2_1/b$ structure [67, 19, 20, 32]. The principal cause of the deviation from the ideal perovskite structure is tilting of the VO_6 octahedra, as previously explained. The monoclinic angle $\alpha = 90.1116^\circ$ at $T = 15 \text{ K}$, was also recorded by Reehuis et. al [20]. This means that the rotation of VO_6 octahedra is more strongly emphasized around the “b” and “c” axes than around “a” axis. This structural transformation is associated with the onset of V $3d$ orbital ordering and a collective Jahn-Teller distortion of VO_6 octahedra.

Magnetism

The magnetism in PrVO_3 is effectively due to the Jahn-Teller active V^{3+} ($3d^2$) ions on the octahedral sites, with an effective magnetic moment of $\mu_{eff}(\text{V}^{3+}) = 2.83 \mu_B$ (spin only, $S = 1$, g

(Lande's g factor) = 2). Below the structural transition T_s , the superexchange interaction between V – V moments stabilizes a C-type antiferromagnetic structure of vanadium sublattice at the Néel temperature, $T_N \sim 130$ K, where, V^{3+} moments are arranged antiferromagnetically in the ab -plane, and ferromagnetically along c -axis. This fashion of vanadium moments alignment remains down to the low temperature. Upon cooling to $T \sim 60$ K, the antiferromagnetic vanadium moments are known to induce a progressive polarization of the praseodymium sublattice through exchange interaction, inducing a partial magnetic order on the Pr sublattice in a doped compound. Upon further cooling down to ~ 10 K, a magnetic order of praseodymium sublattice sets in. At 10 K, the total magnetic moment of V and Pr atom is $\mu_{tot}(V) = 1.36 \mu_B$, $\mu_{tot}(Pr) = 1.62 \mu_B$, which are still smaller than the theoretically expected moments of the V^{3+} ion = $2.83 \mu_B$, and $Pr^{3+} = 3.20 \mu_B$ ($4f^2$, $J = 4$) [20].

In the next section, we will present the spin and orbital correlations in a doped $PrVO_3$ system, when Pr^{3+} is partially replaced with a similar size Ca^{2+} cation.

1.3.2 Effect of doping

A chemical substitution of cation in place of R^{3+} primarily modify the one-electron bandwidth through changes in the crystal structure, and also brings substitutional disorder, which can strongly affect the transport and magnetic properties. In this section, we will consider example of $PrVO_3$ compound doped with a Ca^{2+} cation.

The influence of hole doping on the microscopic spin and orbital correlations in $Pr_{1-x}Ca_xVO_3$ solid solution was reported by two different groups [33, 34]. A partial replacement of the trivalent Pr^{3+} ions by divalent Ca^{2+} ions induces hole doping in the t_{2g} electronic level of V^{3+} ions, thus modifying their spin-orbit interactions. In this section, we discuss how the general properties of doped- $PrVO_3$ changes, as the doping concentration is increased.

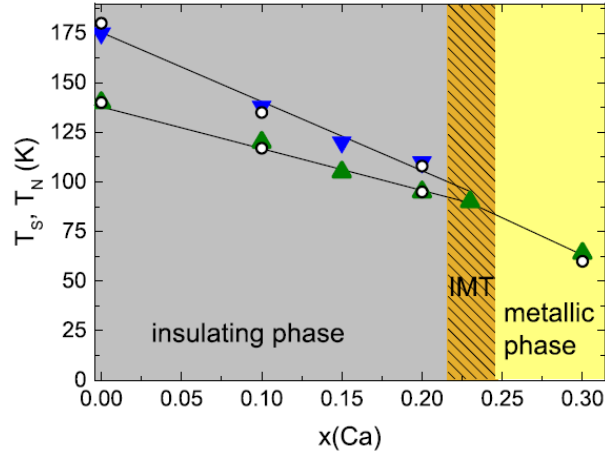


Figure 1.9: Evolution of the structural (T_s) (blue triangles) and magnetic (T_N) phase transitions (green triangles) in $\text{Pr}_{1-x}\text{Ca}_x\text{VO}_3$ system as a function of x . [34]

Physical properties

The increase of Ca concentration in $\text{Pr}_{1-x}\text{Ca}_x\text{VO}_3$ from $x = 0$ to 0.3 dramatically reduces the cell volume by 2.8 % in the orthorhombic phase at $T = 295$ K, and 3.1 % in the monoclinic phase at $T = 15$ K, respectively [34]. Although, the decrease of the b-axis is larger than c-axis in the monoclinic phase, indicating the presence of Jahn-Teller distortion of the VO_6 octahedra. Additionally, the end member PrVO_3 compound is a Mott-Hubbard insulator, but when doped with cation Ca^{2+} , it manifests intriguing phenomenon. Namely, when x is increased from 0 to 0.3, the compound shows an insulator-to-metal (IMT) transition at $x = 0.23$, and a purely metallic behavior at $x = 0.3$ (Fig. 1.9).

Magnetic properties

With increasing the Ca content up to $x = 0.2$, there is a strong decrease in the orbital ordering temperature / structural transition from $T_s = 180$ K ($x = 0$) to $T_s = 108$ K ($x = 0.2$). At $x = 0.3$, the orbital ordering disappears, indicating a quenching of the long-range orbital ordering.

Also, when x is increased from 0 to 0.2, the C-type antiferromagnetic transition temperature (T_N) reduces from 140 K to 95 K, respectively, indicating the destabilization of magnetic ordering (Fig. 1.9). Since the orbital ordering is quenched for $x = 0.3$, one might expect the magnetic spin ordering to be quenched as well. However, there is a weak magnetic contribution for $\text{Pr}_{0.70}\text{Ca}_{0.30}\text{VO}_3$ below ~ 60 K, as shown in Fig. 1.9.

1.3.3 The perovskite oxide thin films: Interfacial effect

The physical properties of a thin film often differ from that of bulk material. In thin films, various newly factors, risen such as, (1) a different microstructure produced by growth process, (2) the nature and implication of the film/substrate interface, (3) size effect phenomenon due to constraint in one dimension, make them different from their bulk counterpart.

The research on the interfacial effect in oxide thin films speeded-up about one and half decades ago, when Ohtomo and Hwang discovered a two dimensional electron gas at the interface between two band insulators, LaAlO_3 and SrTiO_3 [35]. After this, a dominating wave of great interest in thin film community was established. Below, we will describe briefly few significant thin film systems.

Famous LaAlO_3 / SrTiO_3 system

Initiated by Ohtomo et. al [35], the LaAlO_3 / SrTiO_3 system is a well known studied for its key features. Briefly, the LaAlO_3 / $\text{SrTiO}_3(001)$ interface were grown in high vacuum chamber using Pulsed Laser Deposition (PLD). The growth temperature and oxygen partial pressure were, 800 °C and 10^{-4} – 10^{-6} torr ($1\text{torr} \sim 1.33\text{mbar}$), respectively, and a KrF excimer laser with 248 nm frequency was employed. The SrTiO_3 (001) substrates were well etched in order to obtain a TiO_2 -terminated surface. Therefore, a direct deposition of LaAlO_3 on the substrate yields $(\text{LaO})^+ / (\text{TiO}_2)^0$ interface. While, the $(\text{AlO}_2)^- / (\text{SrO})^0$ interface was grown by first depositing

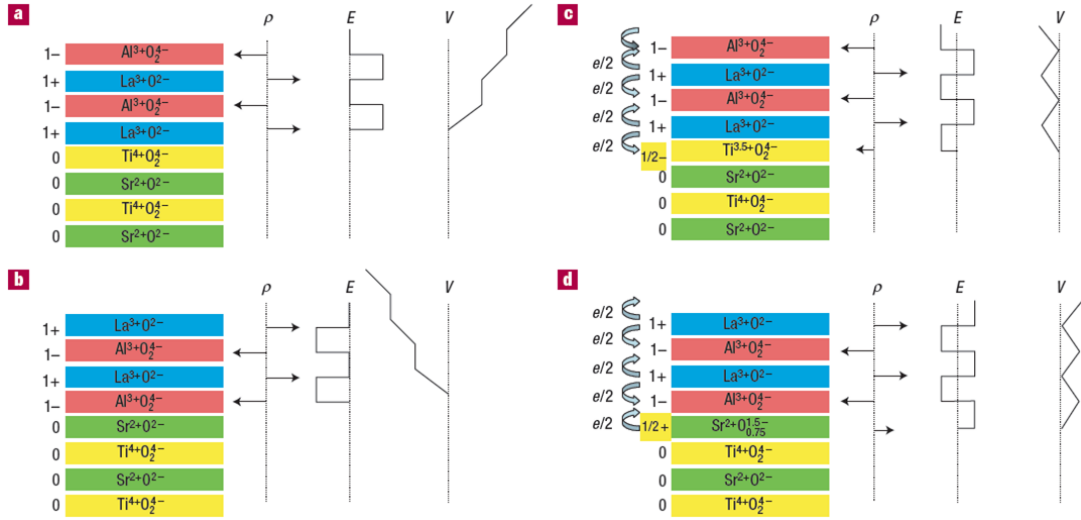


Figure 1.10: Illustration of polar catastrophe between $LaAlO_3$ and $SrTiO_3$ interface [36].

a monolayer of SrO from a single crystal target, then switching to $LaAlO_3$.

This system typically utilizes two wide band gap insulators of band gap 5.6 eV ($LaAlO_3$), and 3.2 eV ($SrTiO_3$). The $SrTiO_3$ and $LaAlO_3$ structure can be considered as an alternating stacks of $(SrO)^0$, $(TiO_2)^0$ and $(LaO)^+$, $(AlO_2)^-$ (Fig. 1.10), and therefore presents neutral layer for $SrTiO_3$ and a charged ($\pm e$) layers for $LaAlO_3$. In heteroepitaxial growth, the interface between these two materials offers an extra $\pm e/2$ (half electron or half hole) per two-dimensional unit cell, depending on the type of interface (Fig. 1.10). Experimentally, the $(AlO_2)^- / (SrO)^0$ interface is p-type and insulating, and $(LaO)^+ / (TiO_2)^0$ interface is n-type and conducting.

In next part, we will discuss briefly the epitaxial thin films of $LaVO_3$, its first growth (on $LaAlO_3$ (001) substrate), and on $SrTiO_3$ (001) substrate.

$LaVO_3 / LaAlO_3$ system

The first thin film of $LaVO_3$ was synthesized by W. Choi et. al. in the early 2000s [37], using pulsed laser ablation method, in a high vacuum ($< 2 \times 10^{-6}$ torr), and at high temperature (400–700 °C). The $LaVO_3 / LaAlO_3$ (001) films are composed of two domains of [110] and

one domain of [001], establishing epitaxial relationship: (a) $LaVO_3[110]_o \parallel LaAlO_3[001]_o$, $LaVO_3[001]_o \parallel LaAlO_3[010]_o$ (or $LaAlO_3[100]_o$), and, (b) $LaVO_3[001]_o \parallel LaAlO_3[001]_o$, $LaVO_3[100]_o \parallel LaAlO_3[110]_o$. (Here, $LaVO_3$ was considered to have $Pbnm$ space group, meaning [001] is the long axis). The films also display a p -type semiconducting behavior, resulting from the thermally activated hopping mechanism. It is noteworthy to mention that, since the lattice mismatch between $LaVO_3$ ($a_{pc} = 3.925$ Å) and $LaAlO_3$ ($a_{pc} = 3.79$ Å) is ~ 3.5 %, multiple domains are observed in the film. Below, we will see that a low lattice mismatch of ~ 0.5 % at the interface in $LaVO_3 / SrTiO_3$ system, leads to only [110]-oriented domains.

LaVO₃ / SrTiO₃ system

The first $LaVO_3$ thin film on top of $SrTiO_3$ (001) substrate was fabricated by Y. Hotta et. al. [38], where $LaVO_3$ layer was sandwiched between two layers of $LaAlO_3$, and thus acts as a quantum well. The $LaAlO_3$ layers can be effectively used to confine the d electrons in $LaVO_3$, as the band gap of $LaAlO_3$ is 5.6 eV, larger than $LaVO_3$ (1.1 eV).

A detailed structural study on $LaVO_3 / SrTiO_3$ (001) thin films was performed by H. Rotella et. al. in 2012 [98, 40], in CRISMAT laboratory. The films were grown in a high vacuum PLD chamber at 700 °C, and 10^{-5} mbar. The $LaVO_3$ films grown at higher oxygen partial pressure are typically not single phased, and seemingly present $LaVO_4$ phase. This system is similar to the earlier discussed $LaAlO_3 / SrTiO_3$ (001), in the sense that, a 2D electron gas also reside at the interface in former as a result of polar discontinuity, *i.e* $(LaO)^+ / (TiO_2)^0$, or, $(VO_2)^- / (SrO)^0$. The structural analysis reveals two [110] domains rotated 90° to each other, and the epitaxial relationship agrees with: $LaVO_3[101]_o \parallel SrTiO_3[001]_c$, $LaVO_3[010]_o \parallel SrTiO_3[100]_c$, and, $LaVO_3[101]_o \parallel SrTiO_3[001]_c$, $LaVO_3[010]_o \parallel SrTiO_3[010]_c$. (Here, the epitaxial relationship is defined considering a $Pnma$ structure of $LaVO_3$, where b is the long orthorhombic axis). Also, contrary to the semiconducting behavior presented by $LaVO_3 / LaAlO_3$ films, LVO / STO films are metallic in nature.

PrVO_3 as a thin film

The first thin films of PrVO_3 were synthesized in the CRISMAT laboratory by O. Copie in 2013 [41]. The chosen substrate for growth of film was cubic SrTiO_3 (STO) (001) ($a_s = 3.905 \text{ \AA}$). The growth temperature and oxygen partial pressure were varied between $500 \text{ }^\circ\text{C}$ and $800 \text{ }^\circ\text{C}$, and between 10^{-3} mbar and 10^{-6} mbar respectively, in order to obtain the optimized growth conditions.

Here, we will now discuss briefly the generalities of PrVO_3 thin films grown epitaxially on a typical single crystal STO (001) substrate, by pulsed laser deposition technique (*principle of this growth technique will be described in detail in the next chapter*).

Structure of film:

An epitaxial PrVO_3 (PVO) ($a_p = a/\sqrt{2} \simeq b\sqrt{2} \simeq c/2 = 3.901 \text{ \AA}$; a_p is the pseudocubic perovskite lattice constant) thin film grown on STO substrate leads to a tensile strain in the film's cell. The structural quality established by conventional x-ray diffraction and high resolution transmission electron microscopy of a PVO film grown at $600 \text{ }^\circ\text{C}$ and 10^{-5} mbar , reveal two domains 90° oriented to each other (Fig. 1.11, domain V_I and V_{II}) [41]. Both the domains are

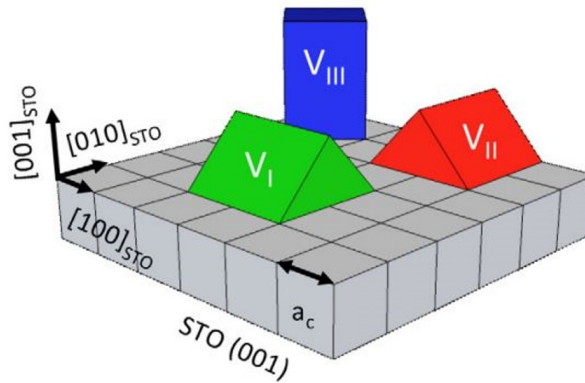


Figure 1.11: Scheme of three oriented domain of PVO film grown on top of STO substrate. The domains observed in HRTEM are mainly V_I and V_{II} . [41]

essentially arranged in such a way that, $2a_p$ (PVO) is always aligned in the substrate plane direction, but differ from 90° (Fig. 1.11). The extracted epitaxial relationship between PVO film and STO substrate is: $\text{PVO}[110]_o \parallel \text{STO}[001]_c$, $\text{PVO}[001]_o \parallel \text{STO}[100]_c$ and $\text{PVO}[110]_o \parallel \text{STO}[001]_c$, $\text{PVO}[001]_o \parallel \text{STO}[010]_c$ (o and c stands for orthorhombic and cubic, respectively). A further careful structural investigation probes that, the PVO unit cell is not orthorhombic anymore as in the parent bulk compound, but rather becomes a monoclinic ($P2_1/m$) one to facilitate the accommodation of stress imposed by STO substrate, together with monoclinic angle $\gamma = 88.8^\circ$ [42]. Additional reciprocal space maps (RSM) analysis of a 100 nm thick PVO film on STO yield, $a = 5.588 \text{ \AA}$, $b = 5.575 \text{ \AA}$, and $c = 7.805 \text{ \AA}$ ($= 2a_s$), with $\frac{a}{b} \sim 1$.

Magnetism:

While bulk PrVO_3 prefers a $P2_1/b$ monoclinic structure together with G-OO/C-SO state in the ground state, the Density Functional Theory (DFT) calculations reveal a $P2_1/m$ monoclinic structure for an epitaxial PVO film grown on STO substrate, associated with a C-OO/G-SO state [42]. Indeed, they predicts two kinds of metastable structure of PrVO_3 thin films with their own SO and OO: (1) canted films with ($a_o + b_o$) free to relax and orthogonal to the substrate plane; (2) Straight films with canted a_o , b_o and thus angle between them $\gamma < 90^\circ$. Nevertheless, a small relative energy difference of $0.5 \text{ meV f.u.}^{-1}$ between the two structure puts PrVO_3 on the verge of two order structure *i.e.* C-SO/G-OO and G-SO/C-OO. However, considering the 90° oriented domains (as observed in the experiments) prevents the canting of the structure, and thus the ground state is found to be connected with G-SO/C-OO, a phase that is never observed in the bulk [65, 97]. In a nutshell, the calculations reveal that the straight films are directly driven to a $P2_1/m$ structure (derived from orthorhombic $Pbnm$), associated with a C-OO and/or G-SO through Kügel-Khomskii rule.

To evidence the epitaxial strain effect on the magnetic properties of PrVO_3 thin films, a direct comparison between PrVO_3 in bulk and thin film form is presented (Fig. 1.12). On the one hand, bulk PrVO_3 , a canted antiferromagnet [110], is characterized by small coercivity $H_c \simeq 0.019 \text{ T}$ (Fig. 1.12(a)), on the other hand a hard ferromagnetic behavior is extracted for a PrVO_3 thin

film, with $H_c \simeq 2.8$ T. Accordingly, the spin-ordering which is strongly coupled with orbit and lattice of PrVO_3 , reduces from 135 K (PrVO_3 bulk) to 85 K (PrVO_3 film).

Chemical strain engineering in PrVO_3 thin films

One of the way of strain accommodation in epitaxial thin films is by creating defects, or, by modify the concentration of oxygen vacancies in thin films grown under high vacuum. This stands up to date a general belief in oxide community that the epitaxial strain imposed by the substrate could control the stability of oxygen vacancies in the perovskite oxide thin films. But is the converse effect true ?, *i.e.* Can we control the lattice strain by monitoring the amount of

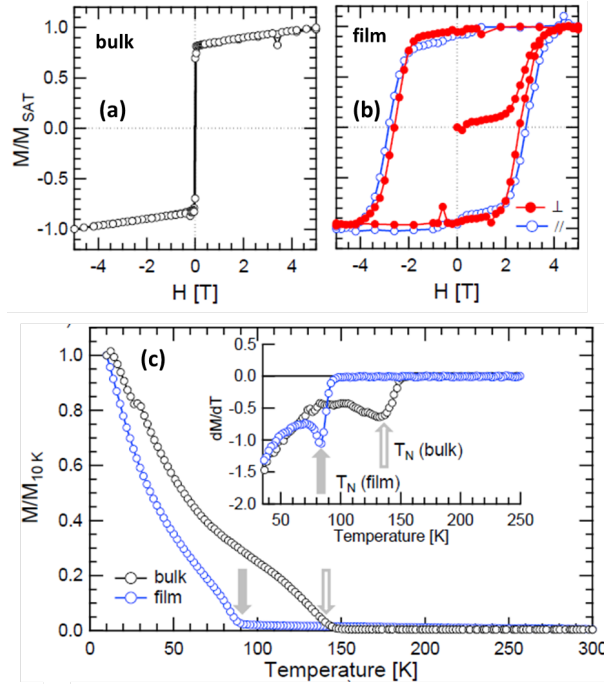


Figure 1.12: Normalized magnetization (M/M_{SAT}) as a function of applied field for (a) bulk PrVO_3 , measured at 10 K, (b) PrVO_3 thin film, measured at 10 K and with a magnetic field applied in sample plane (\parallel) and out of sample plane (\perp). (c) Comparison of M/M_{SAT} as a function of temperature, for bulk PrVO_3 and PrVO_3 thin film. [42]

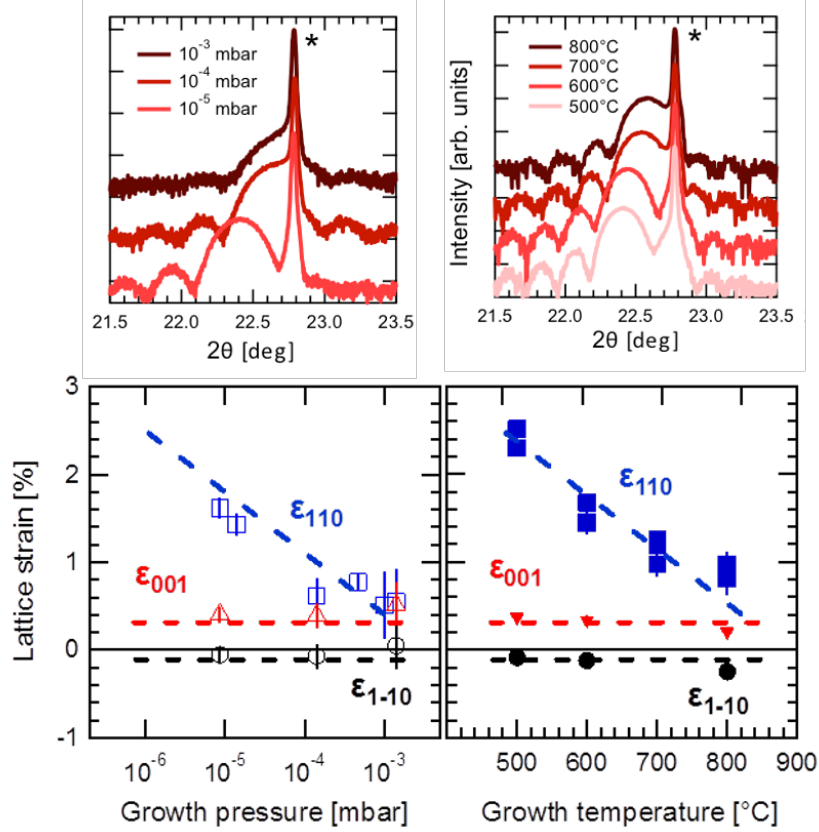


Figure 1.13: HRXRD scans of PrVO_3 films grown under different growth conditions. The *out-of-plane* lattice strain plotted as a function of the growth pressure and temperature.

oxygen vacancies in thin films. Following this, O. Copie et. al. made growth of PrVO_3 thin films on SrTiO_3 substrate, at different growth parameters (Fig. 1.13a). In the 1.3.3.4 section, we have seen that PrVO_3 films grown on (001)-oriented SrTiO_3 substrates have $[110]_o$ axis growth, with $[001]_o$ axis of PVO lying along the substrate plane. Fig. 1.13b illustrates that the two in-plane *i.e.* $[001]_o$ and $[1-10]_o$ directions of PVO are clamped by the substrate, whereas the out-of-plane direction of PVO, which is free to relax, is evolving with the growth parameters *i.e.* with the oxygen contents. This highlights the possibility to tune the chemical strain of 2–3 % in PrVO_3 films by simply controlling the oxygen contents through the growth conditions. As a result, the unit cell volume of PVO is varied with this chemical strain produced by oxygen contents. The magnetic properties of the these films performed as a function of temperature, at an *in-plane*

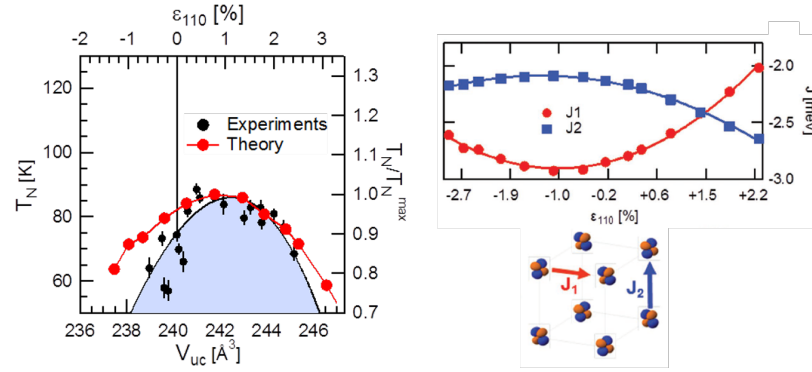


Figure 1.14: Experimental and theoretical evolution of T_N with the unit cell volume of PVO. Magnetic couplings as a function of chemical strain percentage. A representative sketch of coupling constants J_1 and J_2 [42].

applied field of 50 Oe, reveal a bell-shaped evolution of T_N of PVO films with the unit cell volume of PVO. First of all, this behavior is unexpected using any simple model. Second of all, assuming a continuous expansion of the unit cell should result in the reduction of the exchange interaction, hence, decrease in T_N . Nevertheless, the DFT calculations performed by J. Varignon and P. Ghosez completely agrees with experimentally observed trend of T_N . This is explained by utilizing two magnetic exchange constant J_1 (which governs in-plane interactions) and J_2 (out-of-plane interactions), and these two magnetic constants have a reversed behavior for tensile and a large compressive strain, and thus a decrease of T_N (Fig. 1.14).

So far, we discussed the perovskites oxides, namely, the vanadates LaVO_3 (grown on STO and LAO substrates), and PrVO_3 (as a preliminary case), as a thin film. We saw that, LaVO_3 films present different domain structures when grown under different magnitudes of epitaxial strain. Similarly, PrVO_3 show fascinating properties, such as, a low temperature hard ferromagnetic like behavior in PrVO_3 thin film, which is a canted antiferromagnet with a small coercivity in bulk, a 60 K reduction of T_N in thin films compare to bulk.

The main aim of this thesis is to investigate how praseodymium vanadate thin films behave under the application of different epitaxial strains, in line with other studies [44, 45, 46, 47]. In general, the strain in a thin film can be induced using different approaches, namely varying growth temperature [41], growth pressure [42] and chemical substitution. Due to a strong interplay between spin, orbit, and lattice in vanadates, the strain will successively modify the spin-spin and spin-orbit interactions, and eventually favor phases that are absent from the bulk. Our objective is to exploit various single crystal substrates (STO, LSAT, LAO, YAO), film thickness (10 nm to 120 nm), and substrate orientations (STO(001), (110), (111)) as a mean to tailor strain in PrVO_3 films, and study the magnetic phase diagram.

In next chapter, we present the characterisation techniques used during the course of thesis work.

Chapter 2

EXPERIMENTAL TECHNIQUES: GROWTH AND CHARACTERIZATION OF THIN FILMS

In this chapter, we present the growth technique utilized for the deposition of thin films, the method of preparation, and the characterization techniques used in the course of thesis.

2.1 Thin film elaboration

In this section, we present the preparation and growth of PrVO_3 thin films; substrate preparation, growth technique, key parameters.

Throughout this PhD work, the $10 \times 10 \times 0.5 \text{ mm}^3$ substrates (10 mm in length and breadth, and 0.5 mm in width) were employed from CRYSTEC, and finely cut to $5 \times 5 \times 0.5 \text{ mm}^3$ for the film's deposition, using WELL Precision Horizontal Diamond Wire Saw. In practice, the deposition of thin films can be accomplished in two different ways and depending on the type of process involved, they are characterized as chemical and physical deposition. The first class of deposition includes a reactive atmosphere synthesis that uses a carrier gas to move the material to be deposited from container to wafer (substrate). For instance, nano-diamond particles can be grown on a Si substrate in a chemical vapor deposition chamber, which operate at 2200°C , and under high pressure of 5–25 GPa (~ 250000 bar, to compare with PLD). In this process, the precursor gases introduced inside the chamber, are decomposed by the hot-filaments maintained at high temperature right above the substrate, and the required material is deposited on the Si substrates. The second class of deposition typically involves the mechanical and thermodynamical means to transfer the material to be deposited from a source to the substrate. The Thermal Evaporation, Sputtering, Molecular Beam Epitaxy (MBE), Pulsed Laser Deposition (PLD), are well known examples of the deposition techniques that involve a “physical process”, and often summarized as Physical Vapor Deposition (PVD) methods. The choice of any of the technique relies upon the nature of the material to be deposited, shape and size of the substrate, desired film thickness, growth environment, and so on. During my Ph.D., I used pulsed laser deposition technique, and therefore I will emphasize mainly on PLD. In the forthcoming sections, I will discuss different growth modes involving in the thin-film growth, PLD growth technique, and the characterization techniques.

2.1.1 Typical growth modes of thin film

There are three growth processes involved when a thin film is deposited on a substrate. These growth processes essentially depend on the surface energies of the substrate (γ_{ss}), film (γ_{sf}), and the film-substrate interface (γ_{isf}). The surface energy of the substrate can be measured by a contact angle measuring device, which typically defines the adhesiveness between substrate and a water droplet (for example) (Fig. 2.1).

1. **Frank-van der Merwe growth:** It is also called as Layer-by-Layer growth mode (Fig. 2.2(a)), and is essential for heterostructure growth and device requiring smooth surface morphology of intermediate layers. It is considered as the ideal growth mode, and requires a perfect lattice match between the substrate and the layer. For this kind of growth, the atoms deposited (adsorbed atoms) should be more attracted to the substrate surface than to each other, forming a complete monolayer (ML) before another one starts to grow. Mathematically, it can be defined as

$$\gamma_{ss} > \gamma_{sf} + \gamma_{isf}$$

2. **Volmer-Weber growth (VW):** The control of parameters for this kind of growth mode leads to the formation of nano-sized islands, and often called 3D island growth mode

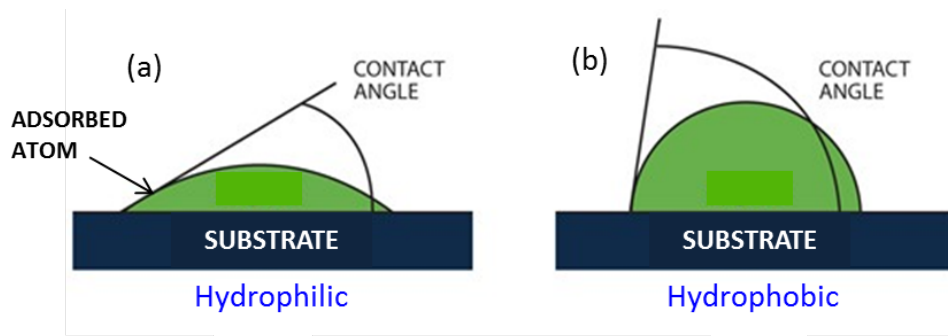


Figure 2.1: Scheme representation of (a) High surface energy (b) and the low surface energy.

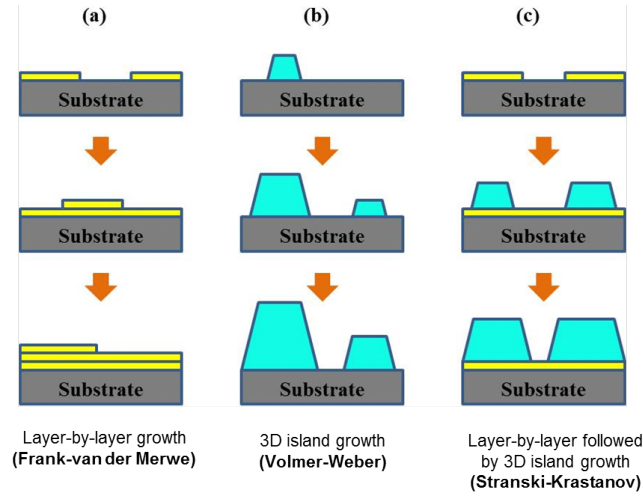


Figure 2.2: Three basic growth modes of thin film. Figure was taken from ref. [48].

(Fig. 2.2(b)). In this growth mode, the interaction of the adsorbed atoms is much stronger among themselves than with its substrate surface, which leads to the formation of clusters or 3D islands, and therefore rough surfaces. Mathematically, it can be represented as

$$\gamma_{ss} < \gamma_{sf} + \gamma_{isf}$$

3. **Stranski-Krastanov growth (SK):** This growth is characterized by mixing both the above growth processes (Fig. 2.2(C)). At the beginning, the adsorbed atoms starts to grow layer-by-layer. When a certain critical thickness is reached, they starts to form islands. The energy requirements for this growth to occur is same as Frank-van der Merwe growth, except a slight lattice mismatch between the film and the substrate is essential.

2.1.2 Pulsed Laser Deposition (PLD)

We have used the Pulsed Laser Deposition (PLD) technique for the growth of PrVO_3 thin films. This technique allows crystallizing very complex crystalline structure by ablating material from a polycrystalline target using a highly energetic pulsed laser under a controlled O_2 atmosphere

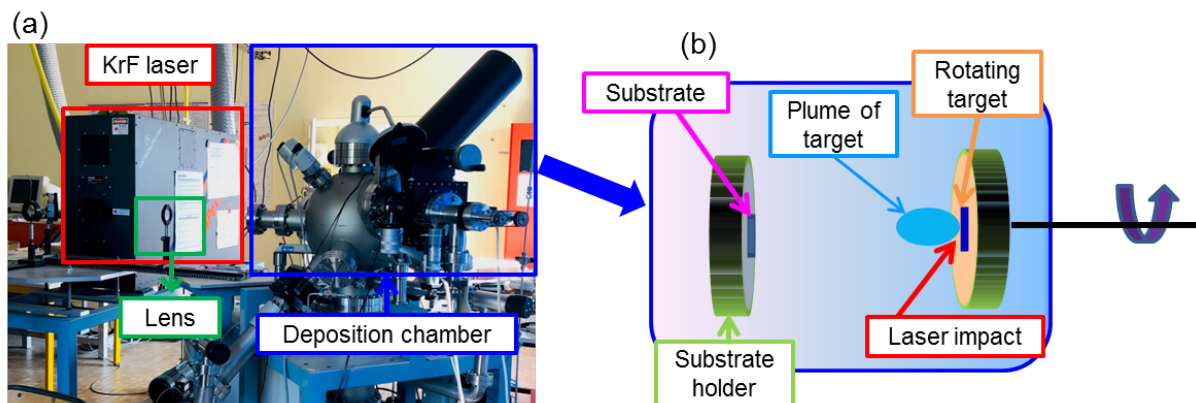


Figure 2.3: PLD set up. Picture (a) and scheme (b).

and pressure [49].

Prior to growth, the substrate is cleaned in the ethanol and acetone (3–6 minutes) in an ultrasonic bath cleaner. Then, the substrate is affixed to the substrate holder (made of Inconel alloy) using silver paste, to ensure a good thermal contact. It is then heated to 200–250 °C on a heater for ~ 15–20 minutes, to dry the silver paste, and well affix substrate on substrate holder. The substrate is then mounted in the growth chamber, and air is let pump out of the chamber in order to achieve a base pressure of $<10^{-7}$ mbar, a prerequisite of deposition. The substrate temperature, measured by a thermocouple, is increased slowly (~ 20 °C / min.) to 600–700 °C for growth, and O_2 pressure is also set to 10^{-6} mbar. Now, the growth can start.

Principle of PLD

The PLD process utilizes a high-power-pulsed excimer KrF UV laser [$\lambda = 248$ nm], the rotating target [$PrVO_4$ in our case] facilitated by a motor, and a heated substrate mounted at a distance of $\sim 4 - 5$ cm from the target (Fig. 2.3(b)).

When the laser is focussed on the target, the following process occurs within 30 nanoseconds. The incident laser pulse penetrates into the surface of the target material within penetration depth, which depends on the laser energy/wavelength and the refractive index of the material. The electric field created by the laser pulse is strong enough to knock the electrons out of the

material. These free electrons, rendering in the electromagnetic field of the laser, can collide with the surface atoms of the target and transfer some of their energy to them. This leads to the heating of the surface and eventually the material is vaporized. The interaction of the laser beam with ejected material leads to the formation of high-temperature expanding plasma, called the plume (Fig. 2.3(b)). The adiabatic expansion gives rise to the forward nature of the plume. The dynamic and shape of the plasma depends strongly on the O_2 background pressure. A high background pressure modifies the trajectory and energy of the ejected species (due to collisions between atoms in plasma and O_2). Once the atoms land on the substrate, depending on the substrate temperature, they arrange on the surface, but a too high temperature can also lead to re-evaporation of some species from the substrate. Therefore, the substrate temperature and growth O_2 pressure are the key parameters to the quality and stoichiometry of a thin film. Finally, the nucleation and growth of film takes place on the substrate. To avoid the formation of droplets, the precautions should be taken. These include the distance between the substrate and target material, laser energy which should be optimized before growth of thin film, and a dense target. Other solutions can be to use a beam homogenizer to avoid the laser hot spots [50].

After growth, the sample is cooled down slowly keeping the growth pressure unchanged, in order to avoid the undesired $PrVO_4$ phase. It is also mandatory to remove the silver paste from the sample after the sample has been taken out of the chamber, as the magnetic measurements are quite sensitive to the remanent of any silver paste.

2.1.3 Growth conditions

We used an optimized growth temperature of 650 °C, and pressure of 10^{-6} mbar for all the samples (any different growth condition will be mentioned), a KrF laser with laser energy 200 mJ, pulse repetition rate of 2 Hz, target to substrate distance 5 cm.

2.2 Characterization techniques

After deposition of thin films, we studied their structural and physical properties using various experimental characterization techniques, which are briefly discussed below.

To know the lattice parameters (*in-plane* and *out-of-plane*), growth mode, epitaxial strain, interfacial quality, we have used X-ray diffraction (XRD), Reciprocal Space Mapping (RSM), Transmission Electron Microscopy (TEM), which are described in the following sections.

2.2.1 Structural characterization techniques

The structural properties of PVO films were explored by using the x-ray diffraction and the electron microscopy. These techniques are described in the following sections.

X-Ray Diffraction (XRD)

A crystal is made up of periodic arrangements of atoms or group of atoms, called *basis*, which is attached to the mathematical points in space, called lattice. The structure of a crystal can be identified using any of the neutron, electron or x-ray photon diffraction. The diffraction, by atomic planes in a crystal, depends essentially on the wavelength of the incident beam and the spacing between planes.

The x-ray diffraction was first explained by W. L. Bragg in the early 1900s. He considered a parallel planes of atoms (Fig. 2.4), spaced d apart. When a beam of x-ray photons of wavelength $\lambda \sim d$ is made to incident on the parallel planes, a diffraction is observed when the rays interfere constructively. First, the main condition required to observe the diffraction pattern is that, the beam should be reflected specularly and elastically (meaning that the x-rays are not changed upon reflection). Second, the extra path travelled by the adjacent beam should be an integral multiple of λ , in order to obtain the constructive interference of waves scattered from lattice points. Accordingly, for any plane with Miller indices (h,k,l), it becomes

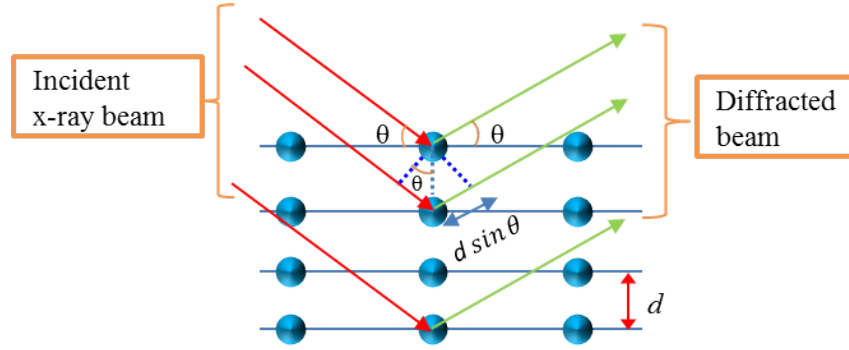


Figure 2.4: Schematic representation of x-ray diffraction, and the derivation of Bragg equation.

$$2d_{hkl} \sin \theta = n\lambda \quad (2.1)$$

Where, d is the interplanar spacing, θ is the angle of incidence (for a specular reflection, angle of incidence is same as the angle of diffraction), and λ is wavelength of incident x-ray beam. Each crystal structure is associated with two kinds of lattices, the crystal lattice and the reciprocal lattice. A typical diffraction of crystal obtained through x-ray diffraction (XRD) technique, is actually a map of reciprocal lattices of crystal. The reciprocal lattice is basically the Fourier Transform (FT) of a crystal lattice in real space. In crystallography, the wave vectors associated with the incident and diffracted beam are generally described in the reciprocal space, because it is more convenient to calculate the solid state properties in the reciprocal space rather than in real space.

The diffracted intensity particularly depends on the atomic arrangement in the crystal, the local electron concentration, phase factor between the incident and diffracted beam, and given by:

$$I = K_0 |F_{hkl}|^2 \quad (2.2)$$

Where, K_0 is a constant, and F_{hkl} is the structure factor, defined by

$$F_{hkl} = \sum_j f_j e^{-i2\pi(x_j v_1 + y_j v_2 + z_j v_3)} \quad (2.3)$$

Where, summation runs over j atoms, f_j is the atomic form factor, or, factor of atomic diffusion, and x_j, y_j, z_j are the coordinates of the j^{th} atom.

For an extensive analysis of the crystal structure, various x-ray scans can be performed, such as

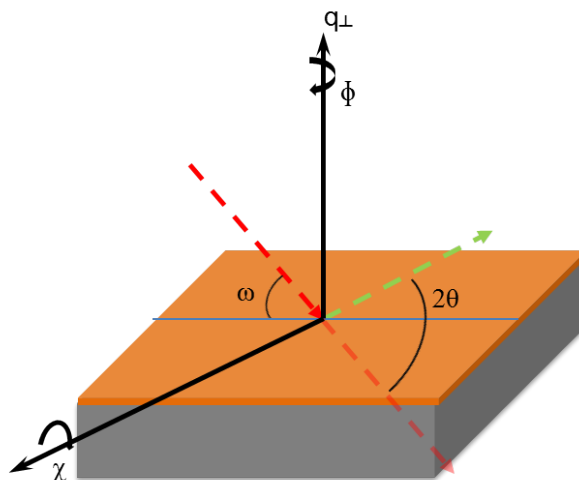


Figure 2.5: Scheme of various x-ray scans.

2θ - ω scan, ω scan, ϕ scan, and χ scan (Fig. 2.5).

2θ - ω scan: The ω and 2θ vectors are varied simultaneously, and the value of $\omega = \theta$ for symmetrical reflections, means that the diffraction wavevector q_{\perp} is perfectly normal to surface plane (Fig. 2.5). This scan provides important informations about the upper layer (in thin films), such as, distance between planes, parallelism of film-substrate interface, and particularly to check whether crystalline phases are incorporated in the crystal.

ω scan / Rocking curve: The 2θ is kept fixed while ω is varied. This scan is mainly used to define the mosaicity of the sample.

ϕ scan: For a fix ω , 2θ , the sample rotates with ϕ , allowing access to symmetry of the crystal and epitaxy of the film compare to the substrate.

χ scan: For a fix ω , 2θ , the angle χ is varied to tilt the sample in order to align it for any asymmetric reflection. This scan is essential for recording Reciprocal Space Maps (RSM), which is discussed in the next section.

Reciprocal Space Mapping

The reciprocal space mapping (RSM) is a mapping of allowed diffraction (by Bragg's equation 2.1) in the Fourier space. This mapping is crucial for determining the in-plane lattice parameters, relaxation state of the film, etc. For a specific reflection, the RSM can be obtained by recording a number of $(2\theta - \omega)$ scans for different $\Delta\omega$ values, and then map / combine all of them in a single file. The reciprocal lattice vectors $\mathbf{b}_1, \mathbf{b}_2, \mathbf{b}_3$ are defined as

$$b_1 = \frac{a_2 \times a_3}{a_1 \cdot (a_2 \times a_3)}$$

$$b_2 = \frac{a_3 \times a_1}{a_1 \cdot (a_2 \times a_3)}$$

$$b_3 = \frac{a_1 \times a_2}{a_1 \cdot (a_2 \times a_3)}$$

Where, a_1, a_2, a_3 are the primitive vectors in crystal lattice, and, b_1, b_2, b_3 are the primitive vectors in the reciprocal lattice. Any vector in the reciprocal space is always orthogonal to the other two vectors in the crystal lattice, this can be described as:

$$b_i \cdot a_j = \delta_{ij}$$

For a symmetric reflection, the diffraction vector q is normal to the crystal surface, and $\omega = \theta$ (Bragg Brentano configuration) (Fig. 2.6(a)). Here, ω is the angle between the crystal surface and the incident X-ray beam, and θ is the angle between scattering planes and the scattered beam. Whereas, for an asymmetric reflection, the diffraction vector is not normal to the crystal surface anymore, but stays normal to the scattering planes (designated as q). In this case, the $\omega \neq \theta$ (Fig. 2.6(b)), and an offset angle between the crystal surface and scattering plane is defined as $\tau = \omega - \theta$. Here, k_i and k_r are the incident and the reflected wave vectors, respectively. The components of the scattering vector parallel (q_x) and perpendicular (q_z) to the crystal surface can be expressed as a function of ω and 2θ as follows:

$$q_x = \frac{2\pi}{\lambda} [\cos(2\theta - \omega) - \cos \omega] \quad (2.4)$$

$$q_z = \frac{2\pi}{\lambda} [\sin(2\theta - \omega) + \sin \omega] \quad (2.5)$$

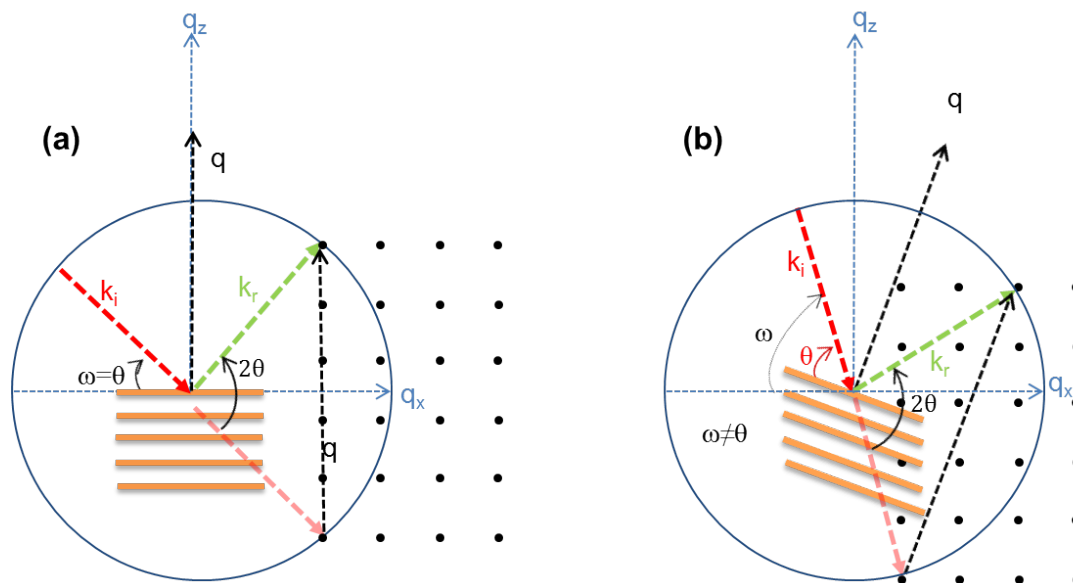


Figure 2.6: Schematic representation of the construction of the Ewald sphere in (a) symmetric and (b) asymmetric configuration.

During my thesis work, I used D8 Discover diffractometer (BRUKER) to map all the required reflections. Nevertheless, the reciprocal space maps provide only a partial information about the crystal structure, for instance, the interplanar spacing, interatomic distance. But, this techniques indeed provides only a global knowledge of the specimen. However, the information at an atomic scale is required. For this reason, we have used Transmission Elctron Microscopy (TEM), which is discussed in the next section.

Transmission Electron Microscopy (TEM)

A Transmission Electron Microscope (TEM) is an analytical tool allowing visualization and analysis of a specimen in the realms of nano-dimensions. TEM is an essential tool for nanoscience, used both in biological and materials fields.

The first electron microscope was made by Max Knoll and Earnst Ruska in 1931, although the magnification was lower than the light microscope. A few years earlier in 1928, De Broglie pub-

lished a paper confirming that, electron has both particle and wave nature [51]. Unfortunately, Knoll and Ruska were unaware of this idea at that time. When they realized that the De Broglie wavelength of electron is much smaller than that of light, they figured TEM can theoretically allow for imaging at the atomic scales. In 1933, they builded another microscope with a higher magnification (Deutsches Museum, Munich, Germany).

An electron microscope typically works on the same basic principle as a light microscope. Except that a beam of electrons is used in TEM, instead of X-ray photons. A beam of electrons, having a smaller De Broglie wavelength than X-ray photons, is emitted from an electron source, usually Tungsten. The beam is then accelerated by the application of a high voltage (50–300 kV) through the so-called electron column, and is focussed using electromagnetic lenses, (because normal glass lenses works only for "light photons" and not for electrons). Then, the beam strikes on the sample, mounted right below the electromagnets, and several phenomena take place due to bombardment of electrons with the sample surface atoms (Fig. 2.7). Namely, the beam can

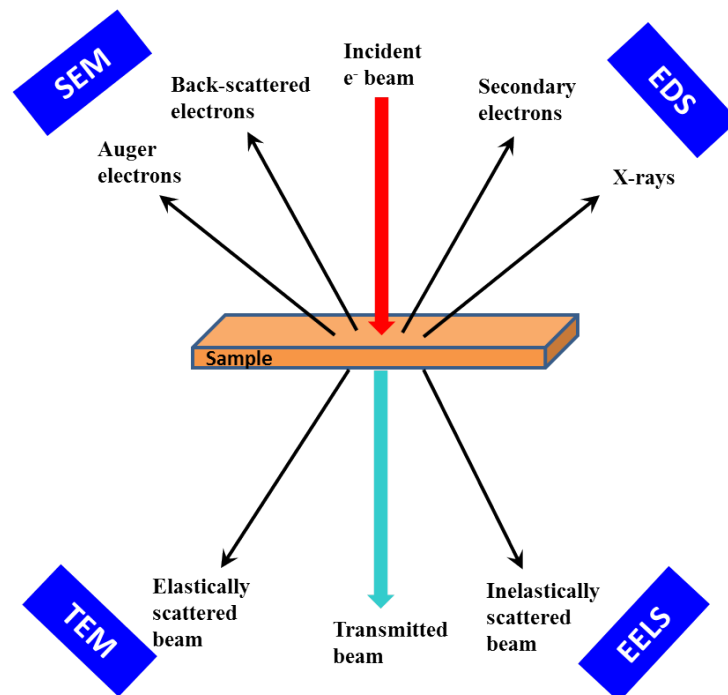


Figure 2.7: Interaction between electron beam and the surface atoms.

be refracted back, diffracted, scattered, transmitted (elastically, inelastically), and so on.

Each of the phenomenon that occurs due to distinct interaction between the electron and sample, provides specific information about the sample. Nevertheless, we will focus here only on the transmitted electrons, which form the transmission electron microscopy (TEM) and is relevant to my thesis. The transmitted beam of electrons form a primary image of the specimen by means of objective lens, due to interaction of electrons with the specimen (stage A, Fig. 2.8). The primary image is then magnified using additional pair of lenses (intermediate lens, and projector lens) to form a final highly magnified image (stage B, Fig. 2.8). The final image is collected at a fluorescent screen, which is situated at the end of the electron column, and light up when electrons hit on it. A digital image can also be captured using a Charge Coupled Device (CCD) camera, mounted right above the phosphor screen. All of these systems are located in a chamber under ultra-high vacuum.

The TEM normally operates in two basic modes, diffraction mode, and imaging mode. In the TEM diffraction mode, a diffraction image is formed at the back focal plane of the objective lens, or at the object plane of the intermediate lens. A diffraction pattern can be viewed on the screen by changing the strength (focal length) of the intermediate lens. This is also referred to as the Selected Area Electron Diffraction (SAED). Whereas in the imaging mode, an image of the specimen is observed at the image plane, using high magnifying lenses. Therefore, to switch the TEM from an imaging mode to diffraction mode, only the voltage feeding the intermediate lens needs to be changed.

Also, to perform the transmission electron microscopy, the sample has to be thinner than 200 nm, in order for electrons to pass through it. To etch a specimen of this dimension requires special techniques, such as, ion milling, Focussed Ion Beam (FIB), etc.

In this study, two electron microscopes were used. The sample preparation, and the imaging were done by Dr. Bernadette Domengès, and Dr. Philippe Boullay.

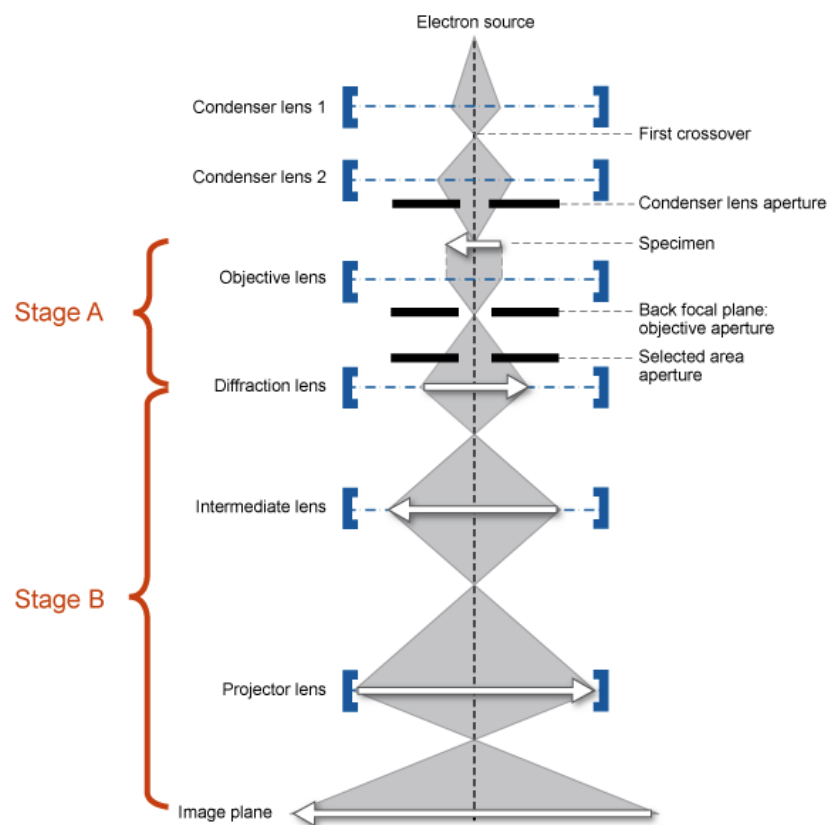


Figure 2.8: Schematic of the optics involved in a typical electron microscope. Taken from *Microscopy Australia*.

2.2.2 Atomic Force Microscopy (AFM)

The Atomic Force Microscopy (AFM) is a scanning microscopy, where the sample surface is probed using a tip attached to a cantilever (Fig. 2.9(a)). A laser is focussed on the cantilever to detect the tip's deflection. In principle, an AFM can be operated in tapping mode, contact mode, and non-contact mode. When the cantilever tip is moved on the sample surface, the tip deflection due to roughness of sample is measured through a sensitive detector, and the sample surface morphology is extracted.

We used a PicoSPM atomic force microscope to perform the AFM scans for our samples. The AFM scans can provide information about the surface roughness of the specimen, by using the formula:

$$R_q = \sqrt{\frac{1}{L_x L_y} \int_0^{L_x} \int_0^{L_y} |Z^2(x, y)| dx dy}$$

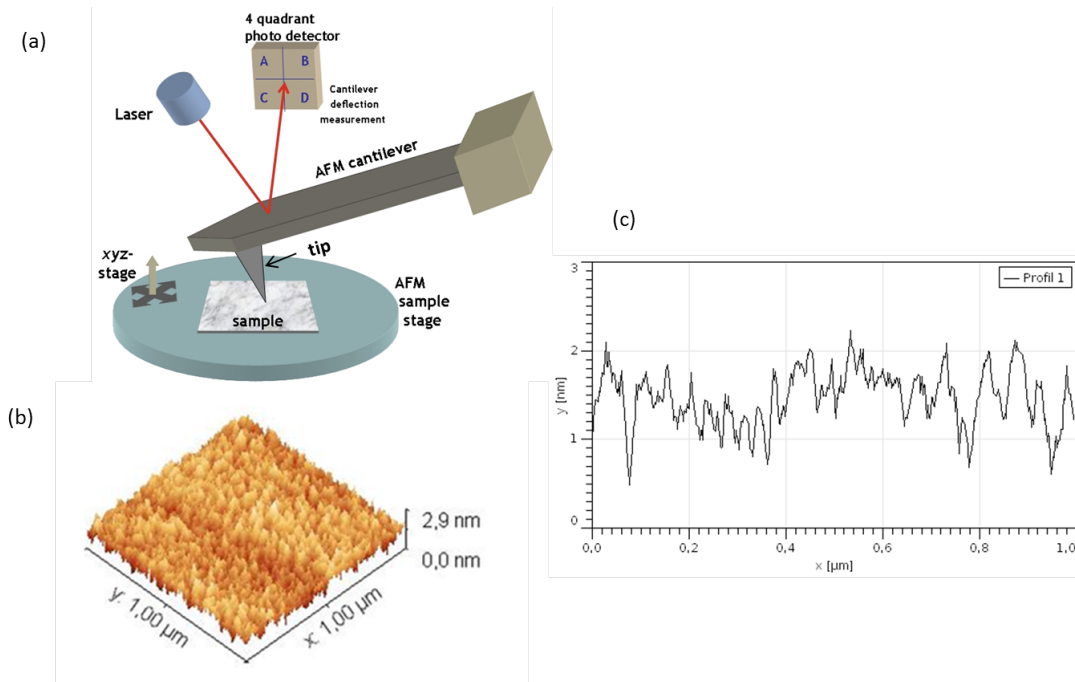


Figure 2.9: (a) Schematic of a typical AFM, (b) a 3D image of a sample surface, and (c) 2D profile of surface roughness, using the formula in text.

Where, L_x , L_y are the length over which the surface roughness is evaluated, and $Z(x,y)$ is the height variation at position (x,y) .

2.2.3 X-ray Photoelectron Spectroscopy (XPS)

The X-ray Photoelectron Spectroscopy (XPS) is a semiquantitative technique for determining composition of a material based on the photoelectric effect. The photoelectric effect is the emission of electrons when light hits a material, and the emitted electrons are called photo-emitted electrons or photoelectrons. The choice of X-ray sources as excitation beams for this technique comes from their ability to probe the core-level electrons. The photoelectric effect for solids can be described as follows:

$$\text{Kinetic energy} = h\nu - \text{Binding energy} - \text{Work function } (\phi)$$

where, $h\nu$ is the incident photon energy. The kinetic energy of the photoelectrons increases as

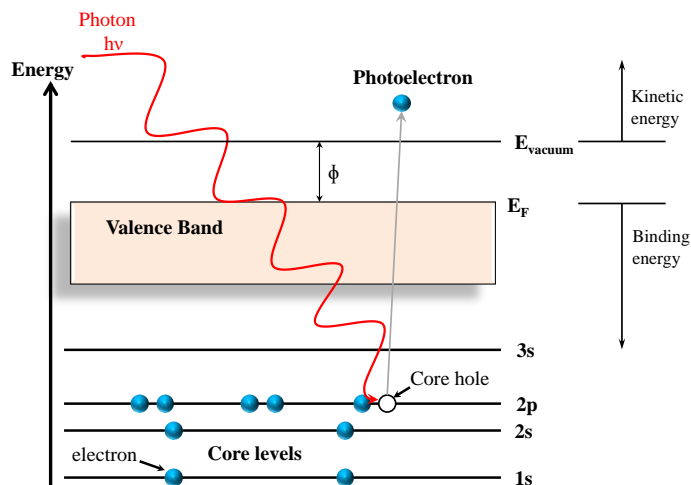


Figure 2.10: The schematic of the photoemission process. Electrons from the sample are extracted by the absorption of high energy photons, and the analysis of these photoelectrons allows to characterize the electronic states of the sample.

the binding energy decreases, and the intensity of photoemission is proportional to the intensity of photons. There is no photoemission, if $h\nu < \phi$. The determination of the kinetic and binding energies of the photoelectrons allows us to characterize the electronic states and chemical environment of the atomic species constituting the sample of interest. Fig. 2.10 shows the schematic of the photoemission process.

The XPS results presented in the manuscript were done in collaboration with Indian Institute of Technology (IIT) Madras by Suraj T S. All spectra were recorded by using Al k_α excitation ($h\nu = 1486.6$ eV) X-ray source, operated at 10 mA and 10 kV. The base pressure of the analyzer chamber was maintained around 5×10^{-7} mbar and operated in a larger area mode by using a hemispherical energy analyzer. The samples were etched by Ar ion sputtering in-situ in the XPS analysis chamber. The binding energies of all compositions were calculated by employing Shirley background type with reference to the C 1s peak at 284.5 eV.

2.2.4 Physical Property Measurement System (PPMS)

After the structure and surface analysis of the samples, we measured their physical properties. In this part, we briefly discuss the Physical Property Measurement System (PPMS), which was used to extract the resistivity of thin films.

The thin films were characterized using a 9T PPMS from Quantum Design, at CRISMAT laboratory (Fig. 2.11). This unique equipment allowed us to perform temperature-field dependent measurements, with temperature range of 1.9 K–400 K.

Electrical resistivity of a thin film

We employed the linear four-point probe technique to measure the electrical resistivity of the samples. The schematic of the experimental configuration is shown in Fig. 2.12. In principle, current is passed through a sample through contacts (between I^+ and I^-), and the potential difference is measured across voltage contacts (V^+ and V^-). Also, the contacts resistance as-

sociated with this method is negligible. Therefore, by using the four-wire method, it is possible to know, both the current and the voltage drop across the sample, and thus the resistance can be calculated. A differential resistance can be expressed as,

$$\Delta R = \rho \left(\frac{dx}{A} \right)$$

However, for an infinitely large slice, where thickness of the slice t is quite smaller than distance between contacts (s), a geometrical factor is multiplied, which depends on the geometry of the sample/slice. Therefore, the above expression, for an infinitely thin slice, becomes,

$$R = \int_s^{2s} \rho \frac{dx}{2\pi xt} = \frac{\rho}{2\pi t} \ln 2$$

Where, s is an average distance between the contacts (Fig. 2.12), this implies,

$$\rho = \frac{\pi t}{\ln 2} R$$

Nevertheless, for a **thin film**, which has a finite, rectangular shape with dimension (a , b), an additional correction factor $R_1 \left(\frac{b}{s}, \frac{a}{b} \right)$ is multiplied to the above expression. Hence, finally, the electrical resistivity of a thin film is given by,

$$\rho = \frac{\pi t}{\ln 2} R_1 \left(\frac{b}{s}, \frac{a}{b} \right) \left(\frac{V}{I} \right) \quad (2.6)$$

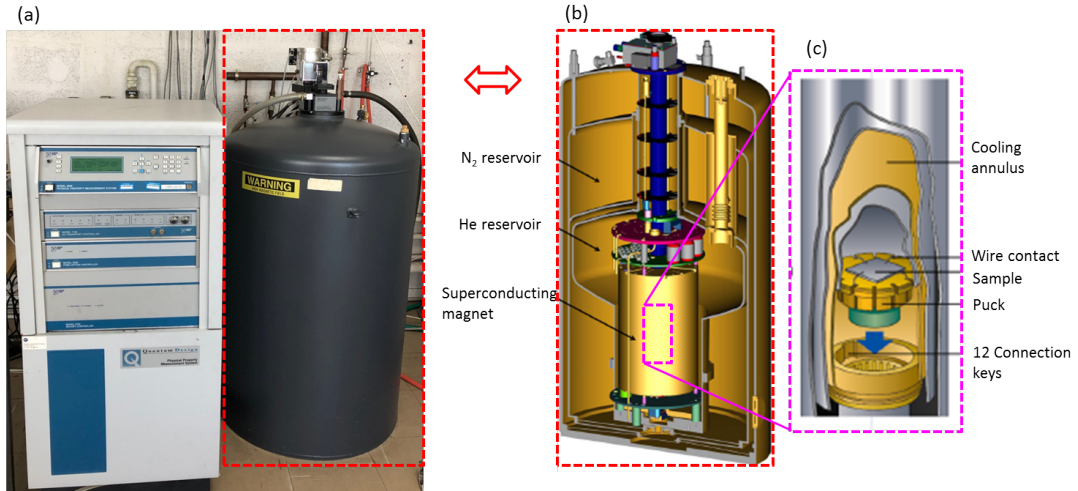


Figure 2.11: (a) Image of our 9T Quantum Design PPMS, at CRISMAT, (b) schematic of inside of a dewar, (c) sample vacuum chamber. Images (b) and (c) were taken from Quantum Design.

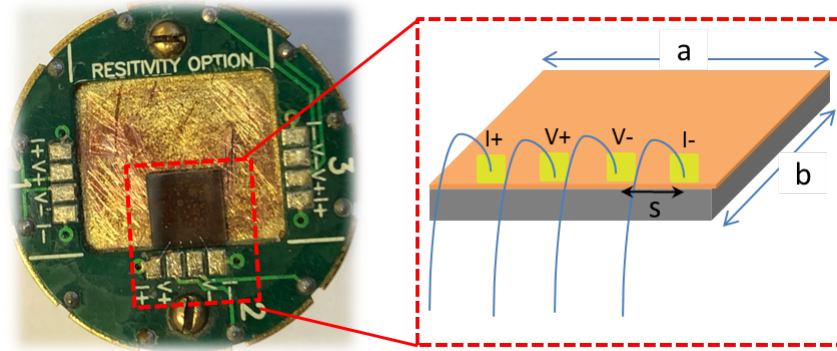


Figure 2.12: The puck used for the resistivity measurements, consisting 3 channels (left), and wire bonding between sample and the support in four-probe configuration (right).

Where, $\frac{\pi t}{\ln 2} R_1 \left(\frac{b}{s}, \frac{a}{b} \right) = G$, is the geometrical correction factor for a thin film of finite dimension (a, b) [52]. The measurement consists of recording the resistance as a function of temperature, and the resistivity is calculated using equation 2.6. If a thin film is deposited on top of an insulating substrate, the resistance of the latter tends to infinity. Therefore, the measured resistance is equal to that of the film.

2.2.5 Superconducting Quantum Interference Device (SQUID) magnetometer

The magnetization measurements in this thesis were carried out by using a Quantum Design DC SQUID based magnetometer.

In general, the SQUID works on two basic quantum phenomena *i.e.* Josephson Tunnelling of electron pairs, and the flux quantization, and is a very sensitive device which can detect a magnetic field as small as 10^{-18} T (and magnetic flux in the range 10^{-7} - 10^{-8}). Our SQUID at the CRISMAT laboratory, which is a DC (direct current) SQUID, is made up of two Josephson Junctions (JJ) in parallel, separating two superconductors. First, the Josephson junction is normally insulating, and the electron pairs (cooper pairs) which makes the superconductor (supercurrent) can tunnel through this junction, depending on the width of junction and applied magnetic flux. The dynamics of the Josephson effect is given by the following equations, where the voltage and current across the Josephson junction is expressed in terms of the wavefunction ψ (probability amplitude) of the electron pair:

$$U(t) = \frac{\hbar}{2e} \frac{\partial \psi}{\partial t}, \quad (2.7)$$

$$I(t) = I_c(t) e^{i\psi(t)} \quad (2.8)$$

Where, in equation (2.7), $\hbar = h/2e$, h is the Plank's constant, e is the electronic charge, and I_c is the critical current in equation (2.8). Second, the magnetic flux inside a superconductor is quantized, that is to say, it changes in the steps of a "quantum flux" (ϕ_0). This is expressed as:

$$\phi_0 = \frac{h}{2e} = 2.07 \times 10^{-15} \text{Wb} \quad (2.9)$$

In principle, when magnetic field is applied to the SQUID, the field tends to change the wave function of electron pairs on either side of the junction, but SQUID resists to this change. Therefore, the SQUID generates a screening current (I_s) and a magnetic field that is equal but opposite to the applied field, thus effectively cancelling the net flux in the superconducting ring (Fig. 2.13(a)). As the applied magnetic flux is increased, the screening current tends to increase. When the applied flux reaches to half the flux quantum ($\phi_0/2$), the junction momentarily becomes resistive, and the current changes the direction. As the applied flux increases further, the

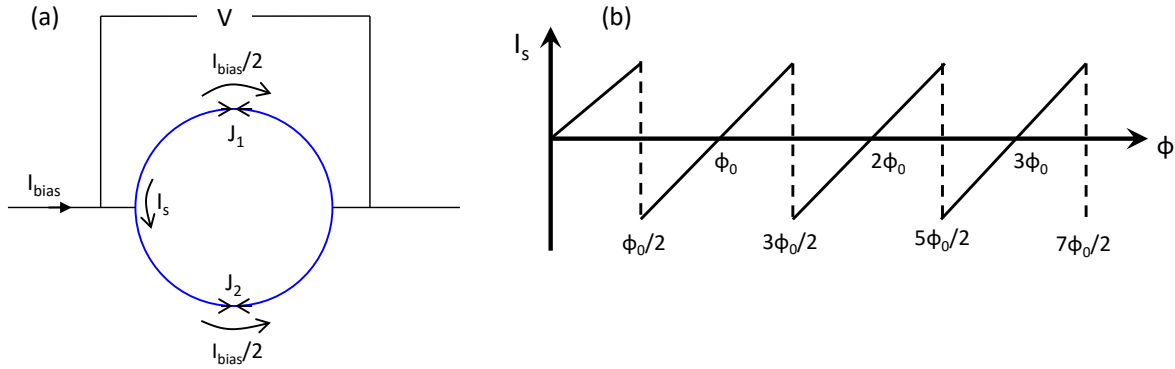


Figure 2.13: (a) A DC SQUID in the presence of applied magnetic field. (b) Variation of the screening current in the SC ring as a function of applied magnetic flux.

screening current decreases, and becomes zero when magnetic flux equals to one flux quantum ϕ_0 (Fig. 2.13(b)). At this point, the magnetic flux inside the loop is equal to the applied flux, thus there is no need for a screening current, and $I_s = 0$. As the applied flux increases further, the screening current starts to flow slowly, and becomes positive, and the cycle begins again. Therefore, the screening current in a superconducting ring is periodic with a period of one flux quantum (also called fluxon) ϕ_0 (Fig. 2.13b).

Fig. 2.14(a) shows our Magnetic Property Measurement System (MPMS), with an electronic cabinet on the left, and the cryostat on the right. The cryostat is liquid helium cooled, equipped with a 5 T superconducting magnet, and is a very sensitive device which is capable of measuring magnetic moment down to 10^{-8} emu. The temperature of the measurement can be controlled between 1.9 K – 400 K, with temperature sweep rate 0.01–10 K/min. The inside of a cryostat is shown in Fig. 2.14b. A sample to be measured, is placed in a drinking straw and well fixed by means of scotch tape, so that it does not move during the measurement. Then, the straw containing sample is attached to the end of sample rod using scotch tape. It is advisory to minimize the use of scotch tape as much as possible, since the measurements can be noisy due to excess use thereof. Before starting the measurements, the sample position has to be optimized with respect to the superconducting magnet. This is done by the sample transport, where the sample is moved across the detection coils (Fig. 2.14c), and SQUID voltage response is measured (Fig.

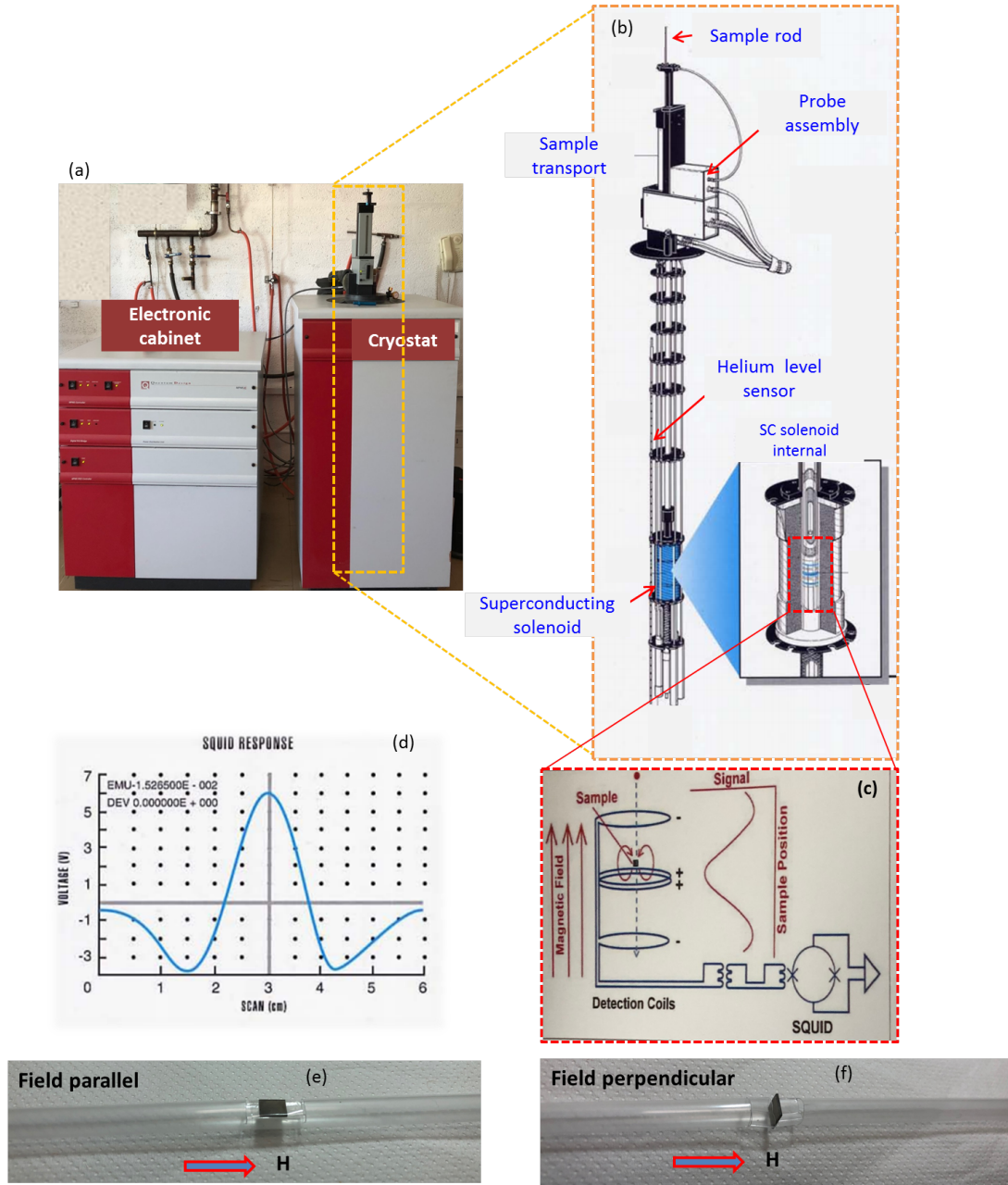


Figure 2.14: (a) Photograph of our SQUID at CRISMAT laboratory. (b) View inside of a cryostat. (c) Schematic representation of a sample moved through the superconducting coils, and (d) a typical SQUID voltage response when sample is moved through coils. Our sample placing geometry inside straw for (e) parallel and (f) perpendicular field. Images (b-d) were taken from CRISMAT laboratory, with permission from Fabien Veillon.

2.14d). The voltage response is then fitted with Multivu software which automatically controls the measurements, and thus the measurements are synchronized. The latter step is repeated by SQUID before beginning of each measurement, and a similar SQUID voltage response curve is produced, which is proportional to the magnetic moment of the sample, and in this way the magnetization of the sample is measured.

We have used $5\text{ mm} \times 5\text{ mm}$ size samples, which can perfectly fit inside the straw/tube in the parallelly applied field configuration (Fig. 2.14e). However, to achieve a perpendicular field geometry, the sample has to be placed differently, as shown in Fig. 2.14f.

Calculation of Magnetization:

To obtain the magnetization of our films in the units of $\mu_B/f.u.$, these steps were followed.

First, conversion of raw data from emu to μ_B by

$$1emu = 1.078 \times 10^{20} \mu_B$$

Second, division of above by the total number of unit cells in the film, which can be calculated as: total no. of unit cells = volume of film/volume of 1 unit cell.

Therefore, finally the magnetization of film can be obtained by multiplying the raw data by a factor of $1.078 \times 10^{20} \mu_B/\text{total no. of unit cells}$.

Estimation of magnetic ordering temperature:

The magnetic ordering(s) in PrVO_3 thin films were realized by plotting derivative of magnetization (dM/dT) versus temperature (T). The minimum in the derivative or a cusp in dM/dT vs T is regarded as the magnetic ordering temperature, similar to work of Copie et. al. [41] (Fig. 1.12).

2.2.6 Magnetism of Reference substrates

The macroscopic magnetization of a sample comprises the magnetization of the film and the substrate upon which film is grown. Thus, in order to obtain the net magnetization of a thin film, the substrate magnetization has to be subtracted. We have used (001)-, (110)- and (111)-oriented SrTiO_3 (STO), $(\text{La,Sr})(\text{Al,Ta})\text{O}_3$ (LSAT), LaAlO_3 (LAO) and YbAlO_3 (YAO) substrates. In practice, these substrates have diamagnetic characteristics, meaning that the magnetic moment is independent of the temperature and opposes the applied magnetic field *i.e.* the magnetization is in opposite direction to that of the applied field. However, there are reports [53, 54], which confirm the presence of small ferromagnetic impurities buried inside the oxide substrates, producing a very small ferromagnetic signal. In addition, the further annealing of the substrates in vacuum at high temperatures during growth could substantially affect the magnetism of the substrates as well.

In our analysis, the true net magnetization of PVO thin films was obtained by subtracting the diamagnetic background of the substrate, simply by subtracting the slope obtained by fitting of raw M vs H data at high magnetic fields. This method is simplistic and widely accepted if the utilized substrate is purely and inherently diamagnetic. But the presence of small ferromagnetic impurities, originating from magnetic tweezers, scotch tape and/or buried Fe-based impurities, also cannot be denied. Thus, in order to check for any paramagnetic or ferromagnetic signals from the impurities in the substrates, the M versus H and M versus T for the as received and the vacuum-annealed substrates were collected using the identical sequence used for the measurements of the samples (substrate + film). The reference substrates were therefore annealed as the growth condition of PVO: at oxygen partial pressure (P_{O_2}) = 10^{-6} mbar, 650 °C for the time duration equivalent to the time of film growth.

From the M versus H plots (at $T = 20$ K) of the annealed and the as received LAO, LSAT and STO substrates (Figs. 2.15, 2.16, 2.17), it is clear that both the as received and the vacuum-annealed substrates are diamagnetic, as the magnetic susceptibility is negative and independent of the temperature. However, the as received LAO substrate shows a small magnetic

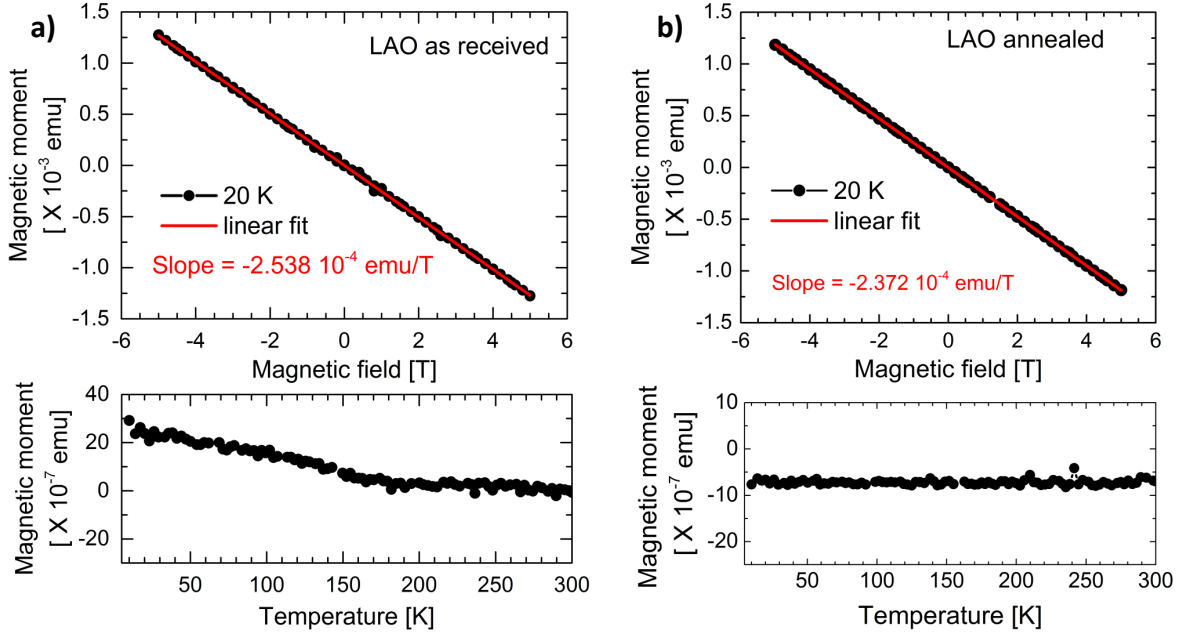


Figure 2.15: M vs H at $T = 20$ K and M vs T at $H = 50$ Oe for (a) the as received and (b) vacuum-annealed LaAlO_3 substrates.

signal dependent of the temperature, which also remains positive over the measured temperature range. But, the annealed LAO substrate is diamagnetic, wherein the magnetic moment remains negative and independent of the temperature. The YAO substrates, both annealed and as received, clearly show the ferromagnetic signals at low magnetic fields, which are shown in the insets of figs. 2.18(a), (b) after the removal of diamagnetic background. Apparently, the ferromagnetic signal for the annealed YAO substrate can be seen up to 300 K (may be even higher), and most probably related to the iron-based impurities in the substrate. Nevertheless, we have subtracted the magnetic contributions of the vacuum-annealed substrates from the sample's magnetization in order to obtain the true magnetization of the films. However, the magnetic moments of the substrates are an order of magnitude smaller than that of the films (for example, at 5T, $\sim 2.0 \times 10^{-4}$ emu for a 50 nm PVO film on YAO substrate, and $\sim 1.5 \times 10^{-5}$ emu for annealed YAO substrate) and therefore no significant changes in the magnetization of film are seen after the subtraction of substrate's magnetic signal. The temperature dependence of magnetic moments of the substrates were also subtracted from that of the sample moments in order

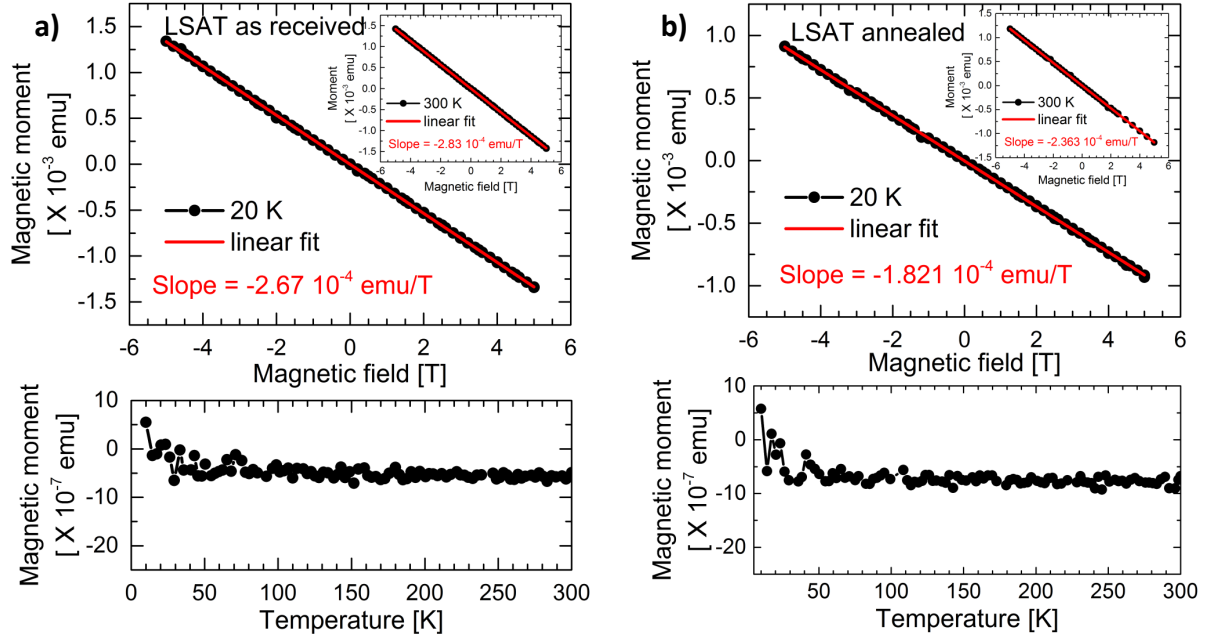


Figure 2.16: M vs H at 20 K and M vs T (H = 50 Oe) for the (a) as received and (b) vacuum-annealed LSAT substrates. The insets show M vs H at 300 K.

to obtain the true temperature dependent magnetization of the film.

In the last chapter of the thesis, we also discuss the magnetic anisotropy in PVO thin films grown on the (001)- (110)- and (111)-oriented STO substrates, by applying magnetic field along the sample plane, and perpendicular to the sample plane. Therefore, in order to avoid any anisotropy contribution from the substrates and to verify if the magnetic susceptibilities of the substrates are similar for the field direction along in-plane and out-of-plane of the substrate, the raw M versus H loops of the annealed STO(110) and STO(111) substrates are shown in Fig. 2.19 and Fig. 2.20, respectively. First, it is evident that, neither of the substrates have any ferromagnetic impurities for field applied along in-plane and out-of-plane of the substrates. Second, the magnetic susceptibilities (dM/dH , or slope of M vs H) are also very similar for both the directions of the applied magnetic field.

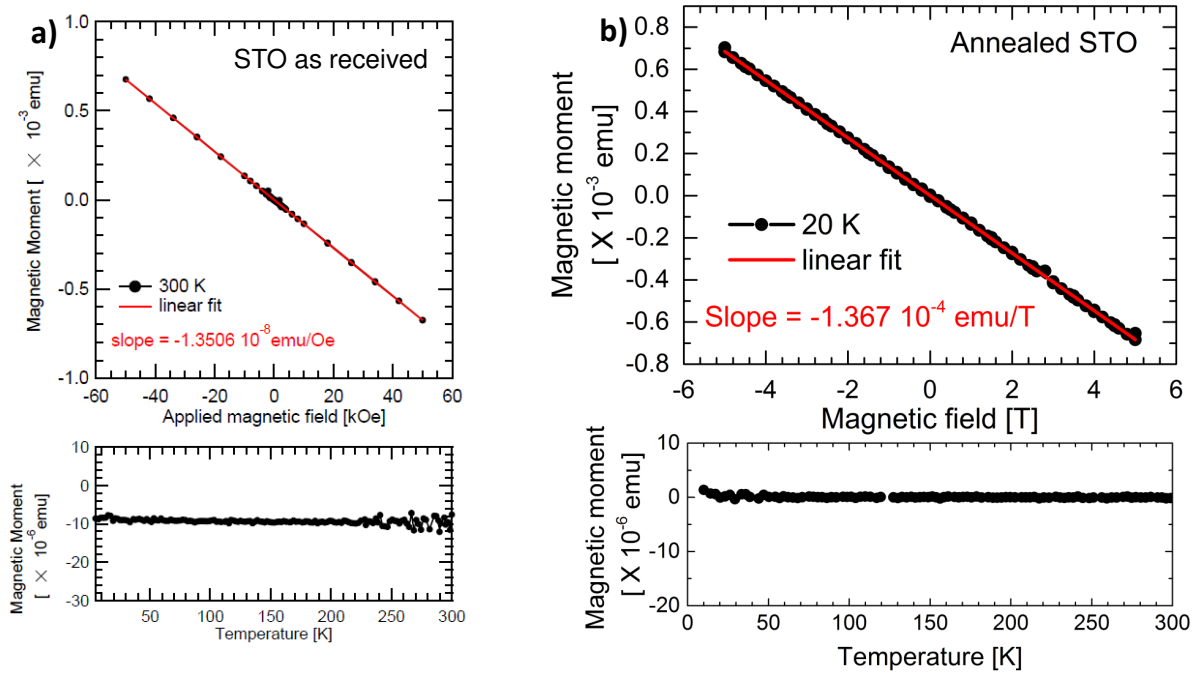


Figure 2.17: M vs H and M vs T for the (a) as received and (b) vacuum-annealed SrTiO₃ substrates.

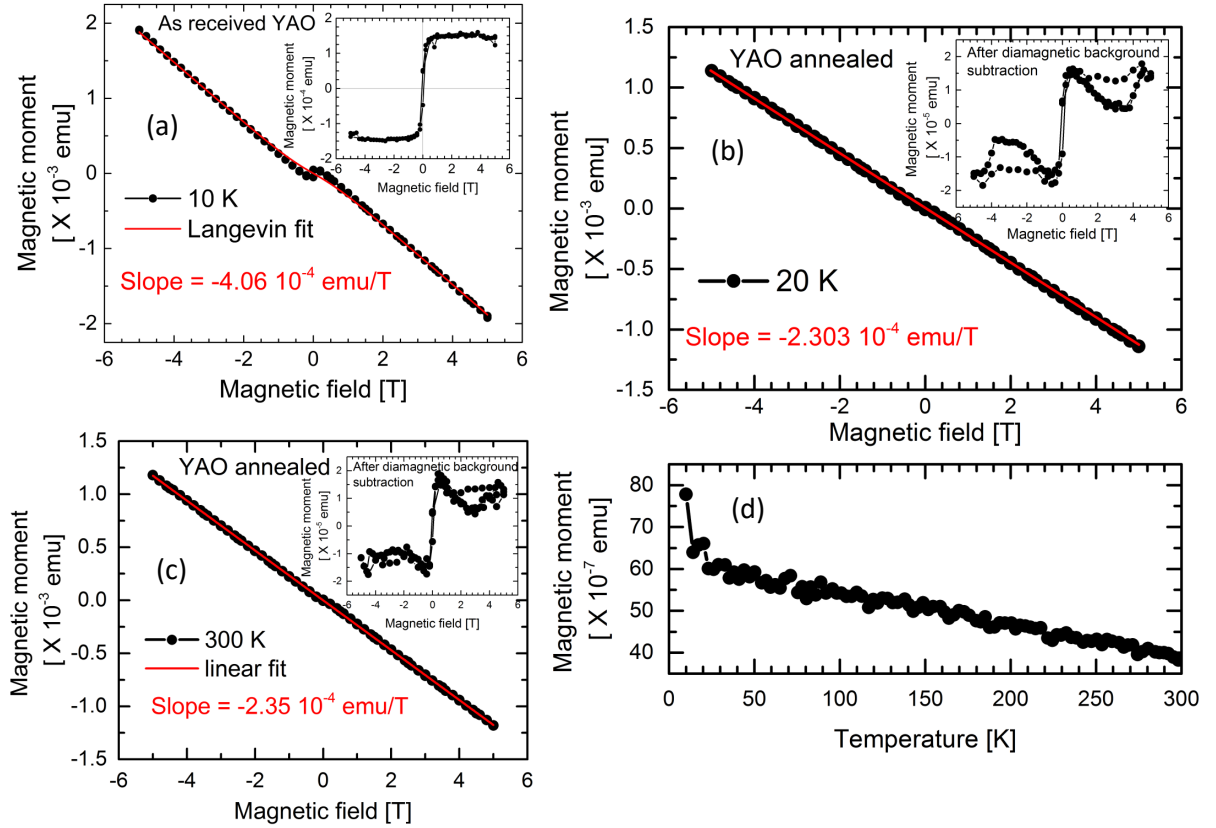


Figure 2.18: (a) M vs H of an as received YAO substrate. Inset shows the magnetic signal after the subtraction of diamagnetic background. (b) M vs H for an annealed substrate at 20 K, and the inset shows the magnetic signal of the substrate after the subtraction of diamagnetic background. (c) The M vs H loop at 300 K, where the ferromagnetic signal can still be seen in the inset. (d) The M vs T (at $H = 50$ Oe) for the vacuum-annealed YAlO_3 substrates.

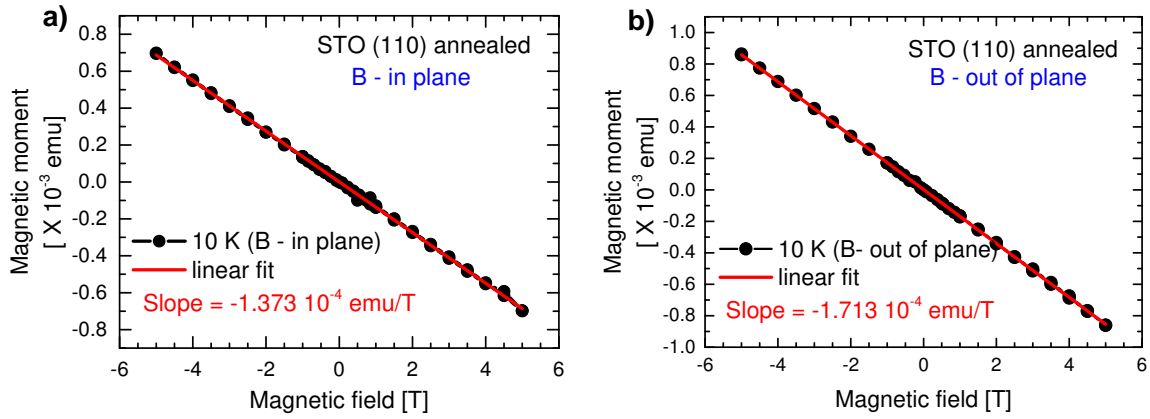


Figure 2.19: Raw M versus H data of the (110)-oriented STO substrate after dummy growth process for magnetic field applied along in-plane and out-of-plane directions of the substrate.

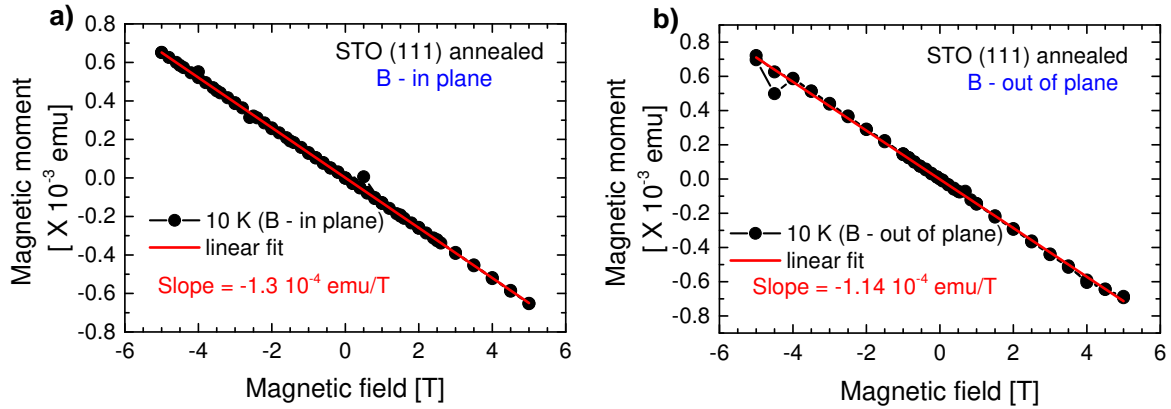


Figure 2.20: Raw M versus H data of the (111)-oriented STO substrate after dummy growth process for magnetic field applied along in-plane and out-of-plane directions of the substrate.

In conclusion, we have seen that STO, LAO and LSAT substrates are diamagnetic, but, the YAO substrates (as received and annealed) have small ferromagnetic signal which lasts up to 300 K and should be related to Fe-based impurities buried in the substrates. The (110)- and (111)-oriented STO substrates are also diamagnetic, with almost equal magnetic susceptibilities for field out-of-plane and in-plane of the substrates.

In this chapter, I have presented the experimental techniques utilized in the thesis. In the forthcoming ones, I will discuss the main characteristics of PVO thin films, and how these properties can be altered or tuned by the induced epitaxial strain via different means, such as by using different substrates, varying film thickness and finally by using different oriented STO substrates. In the next chapter, we will discuss the effect of epitaxial strain produced by various single crystal substrates on the physical properties of PrVO_3 thin films.

Chapter 3

STRAIN ENGINEERING IN PrVO_3 THIN FILMS: USING STO, LSAT, LAO, YAO SUBSTRATES

In this chapter, we present the main characteristics of PVO thin films grown under different strains. We will start with the structure determination by XRD and TEM, and then discuss their detailed magnetic properties. Finally, we conclude the chapter by correlating structural and magnetic properties thereof.

3.1 Prerequisite

Altering of strain in thin films is always interesting as it can promote hidden phases that are absent from the bulk compounds. This can be achieved by growing films of certain thickness using commonly utilized deposition techniques, for instance PLD. The strain in turn is accommodated via different means, such as through rotation of octahedra, changes in the bond lengths, and

sometimes through creating defects [55]. The investigation of each of these modifications indeed requires a great deal of effort. Moreover, the nature, and/or sign of strain is also another key to control the properties of a thin film. In this chapter, we present the physical properties of PrVO_3 thin films as a function of strain.

3.1.1 Preliminary growth conditions

The synthesis of PrVO_3 thin films was carried out using the Pulsed Laser Deposition (PLD) technique, at CRISMAT laboratory, Caen. A variety of single crystal substrates were utilized for the study, for example SrTiO_3 (STO) (100), $(\text{La,Sr})(\text{Al,Ta})\text{O}_3$ (LSAT) (100), LaAlO_3 (LAO) (100) and YAlO_3 (YAO) (110). The details of the lattice parameters, lattice mismatches etc. associated with the substrates are discussed in the next section. The polycrystalline PrVO_4 target was synthesized from stoichiometric mixture of Pr_6O_{11} and V_2O_5 powders by standard solid state reaction, pressed into pellets and prepared in air at 1100°C during 48 hours. The synthesis of PrVO_3 thin films was repeated a number of times before beginning of the series, to optimize the growth conditions. The utilized growth conditions are below:

- substrate: SrTiO_3 (001), LSAT (001), LaAlO_3 (100), YAlO_3 (110);
- target: PrVO_4 ;
- film thickness: ~ 50 nm;
- substrate temperature: 650°C ;
- atmosphere: under vacuum (10^{-6} mbar);
- substrate to target distance: 5 cm;
- laser KrF ($\lambda = 248$ nm) Excimer: 2 Hz, 200 mJ ($\sim 1\text{ J/cm}^2$).

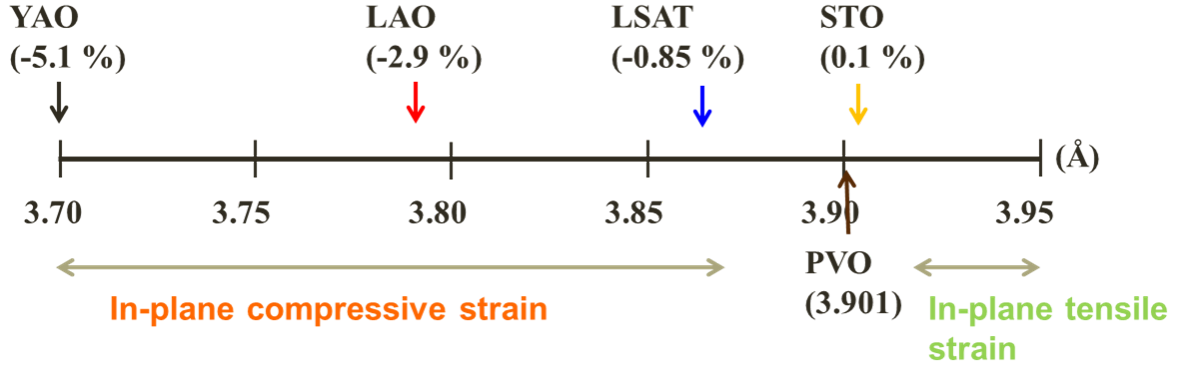


Figure 3.1: Scheme representation of lattice mismatch between PVO and all substrates.

3.1.2 Derivation of lattice misfit

The calculations of lattice misfit or lattice mismatch (σ) between the lattice of bulk PrVO_3 and the substrates in study were performed by using the following formula:

$$\sigma(\%) = \frac{a_{sub.} - a_{layer}}{a_{sub.}} \times 100 \quad (3.1)$$

where, $a_{sub.}$ and a_{layer} are the pseudocubic (pc) lattice parameters of the substrate and layer (PVO), and the lattice mismatch is expressed in percentage (%).

The as-received single crystal perovskite substrates from *CrysTec* were employed. At room temperature, the SrTiO_3 is cubic with lattice parameter $a_c = 3.905 \text{ \AA}$, LSAT has a pseudocubic structure with $a_{pc} = 3.868 \text{ \AA}$, LaAlO_3 has a rhombohedral crystal lattice with $a_{pc} = 3.791 \text{ \AA}$, and YAlO_3 is orthorhombic with pseudocubic lattice parameter 3.710 \AA . For simplicity, we have used the pseudocubic lattice parameters throughout this thesis to calculate the mismatch or strain. The bulk PrVO_3 , at room temperature, adopts an orthorhombic $Pbnm$ structure, with $a = 5.487 \text{ \AA}$, $b = 5.564 \text{ \AA}$, and $c = 7.778 \text{ \AA}$ [61]. In here, we consider a pseudocubic unit cell of PVO that yields $a_{pc} \approx a_o/\sqrt{2} \approx b_o/\sqrt{2} \approx c_o/2 \approx 3.901 \text{ \AA}$.

Following equation (3.1), the theoretical lattice mismatches between PVO and the substrates are: +0.1 % (STO), -0.85 % (LSAT), -2.9 % (LAO), and -5.1 % (YAO). Here, a positive and negative sign refer to tensile and compressive mismatch, respectively (Fig. 3.1). In the next section, we will describe the structural analysis performed using x-ray diffraction technique.

3.2 Preliminary structural analysis by XRD

The analysis of the PVO thin films starts with x-ray diffraction (XRD) in the θ - 2θ Bragg-Brentano configuration. This scan allows us to confirm the desired phases, and also the crystallinity of PVO thin films. Fig. 3.2 shows the representative θ - 2θ XRD scans of the PVO thin films grown on various substrates. We observe that the PVO thin films are single phase, and present film thickness fringes (commonly known as *Laue fringes*). This attests a high quality, well defined and atomically smooth film-substrate interface. These fringes are however suppressed in the case of PVO film grown on the LAO substrate (PVO/LAO), presumably due to presence of the

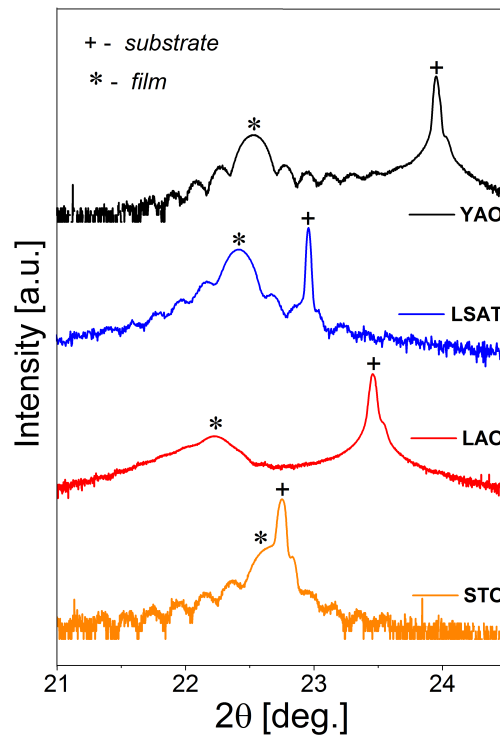


Figure 3.2: θ - 2θ HRXRD scan for a series of 50 nm thick PVO films on different substrates. The $(001)_{pc}$ Bragg peak of the film and substrate (STO, LAO, LSAT), and $(110)_{pc}$ of YAO substrate are indicated by the * and +, respectively.

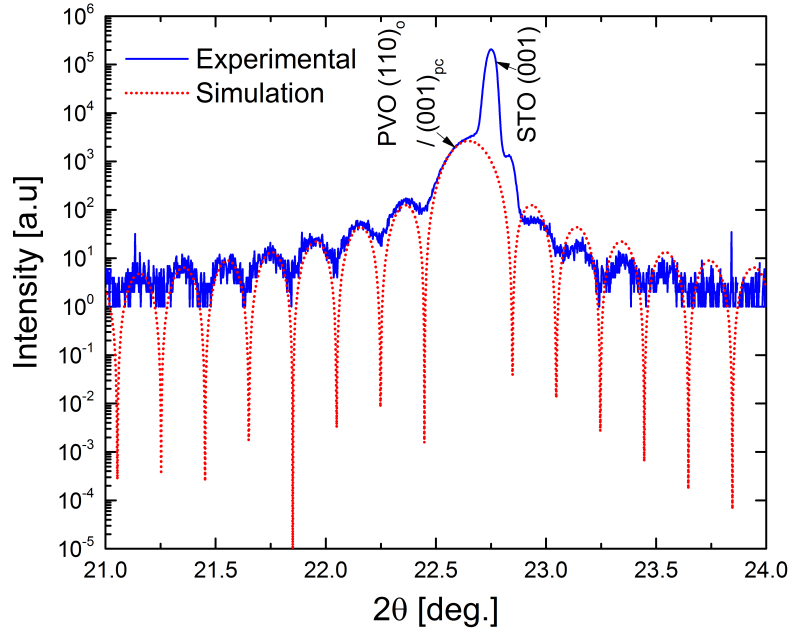


Figure 3.3: A representative XRD scan of a PVO film grown on the STO (001) substrate (in blue). The oscillations in red are the fit to the observed thickness fringes, achieved using a simulation, which incorporates and dependent of the *out-of-plane* lattice parameter and total number of unit cells in the film. A change in the *out-of-plane* lattice parameter shifts the fitted curve to left or right, and number of unit cells define the periodicity of oscillations, thus providing an estimate of film thickness.

twin domains in the LAO substrate. An approximate estimate of film thickness was made by fitting these fringes using a simulation (details given in Fig. 3.3 for PVO/STO for example).

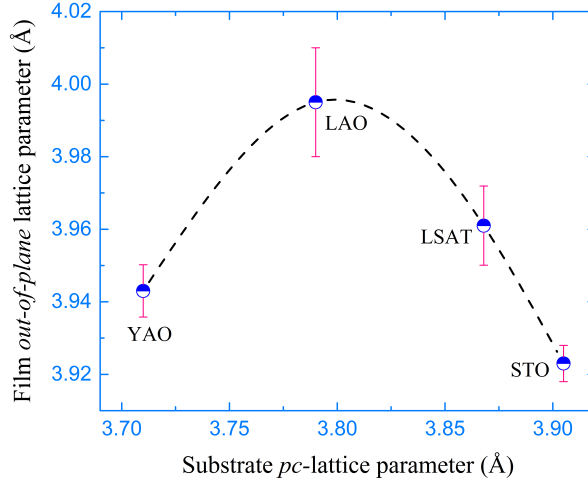


Figure 3.4: PVO film *out-of-plane* lattice parameter as a function of substrate lattice parameter. The *out-of-plane* lattice parameters are extracted from θ - 2θ scan, and are plotted here with error bars. The calculation for error bars is given in the *Annex section*.

3.2.1 *Out-of-plane* structure

The PVO films are grown under compressive strain on the LSAT, LAO, and YAO substrates, as the *in-plane* unit cell parameter of these substrates is smaller than the pseudocubic cell parameter of bulk PVO. Thus, the *out-of-plane* of PVO is expected to enhance compared to the bulk lattice parameter. On the other hand, the STO has a slightly bigger cell than the bulk PVO, leading to an *in-plane* tensile strain in PVO film, and therefore the *out-of-plane* is anticipated to be smaller than its bulk counterpart *i.e* 3.901 Å.

In this work, the *out-of-plane* lattice parameters of the PVO films are extracted from the θ - 2θ XRD scans (Fig. 3.2), and plotted in Fig. 3.4. The extracted *out-of-plane* lattice parameters of the films are 3.995 Å, 3.961 Å, 3.943 Å and 3.923 Å for LAO, LSAT, YAO and STO, respectively (Table 3.1). We observe that while the *out-of-plane* lattice parameter of PVO/LAO is enhanced significantly and is evidently highest in the series. On the contrary, it is decreased for PVO/STO and is minimum in the series. This indicates that the PVO film undergoes a maximum

compression (reduction of *in-plane* of PVO) in the film plane when grown on the LAO substrate, so as to give the largest *out-of-plane*. On the other hand, an *in-plane* tensile strain in PVO/STO film reduces the *out-of-plane* lattice parameter, as foreseen. Interestingly, the *out-of-plane* of PVO/YAO film is less than PVO/LAO. For the PVO film grown on a large lattice-mismatched YAO substrate, this seems plausible that the film is not able to adopt the strain associated with the YAO substrate. Nevertheless, to fully understand the *in-plane* strain structure of PVO films, we detail the reciprocal space maps in the next section.

3.2.2 *In-plane* structure

The reciprocal space maps (RSM) provided us information about the *in-plane* lattice parameters of PVO films. For this, we recorded the RSM maps around $(103)_{pc}$ (*pc* refers to the pseudocubic notation) reflection of STO, LSAT and LAO, and around (212) of the YAO substrate (Fig. 3.5).

Reciprocal Space Mappings

Fig. 3.5 shows well developed PVO film peaks in the lower region, and strong substrate peaks in the upper region of the maps. Since the horizontal peak positions of the PVO film coincide with those of the substrate for both LSAT and STO substrate, we deduce that the film is fully strained with the substrate, and has the same *in-plane* lattice constant. In the case of LAO, the small shift of the film peak to lower Q_{in} value suggests an increase of the *in-plane* lattice parameter, and a partially relaxed film, which confirms a flexibility of the PVO lattice for a large strain associated with large lattice mismatch of -2.9 %. Finally, we see that the PVO film is fully relaxed on YAO, indicating that the growth is not coherent for this substrate, which can be explained by large compressive lattice mismatch (-5.1%). The extracted *out-of-plane* and *in-plane* lattice parameters are summarized in the Table 3.1.

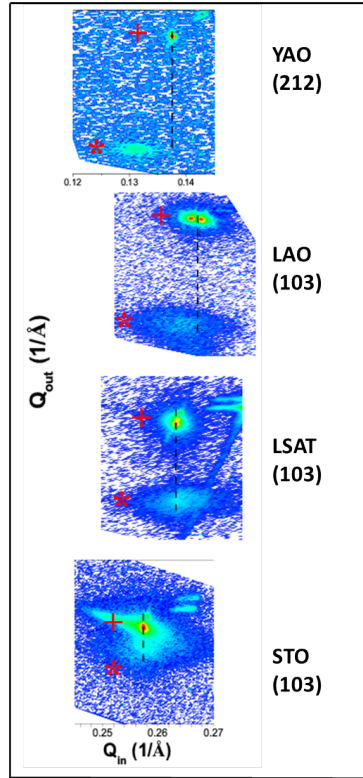


Figure 3.5: Asymmetrical RSM scans of PVO films grown on different substrates, around (103) of STO, LAO, LSAT substrates, and (212) of the YAO substrate. The measured reflections are in the pseudocubic description.

Table 3.1: Summary of observed lattice parameters, experimental lattice mismatch, pseudocubic cell volumes, distortion (ratio of the *out-of-plane* to *in-plane* PVO lattice parameter), residual strain calculated *out-of-plane* i.e ϵ_{110} .

Substrate	<i>In-plane</i> lattice parameter of substrate [Å]	Lattice mismatch (%)	<i>In-plane</i> lattice parameter of film [Å]	<i>Out-of-plane</i> lattice parameter of film [Å]	Pseudo-cubic unit cell volume [Å ³]	Distortion	Residual strain (<i>out-of-plane</i>)(%)
YAO	3.710	-5.15	3.860	3.943	58.75	1.022	1.077
LAO	3.790	-2.93	3.830	3.995	58.60	1.043	2.412
LSAT	3.868	-0.85	3.868	3.961	59.26	1.024	1.540
STO	3.905	0.10	3.905	3.923	59.82	1.005	0.566

Remarkably, the *out-of-plane* lattice parameter of all PVO films has increased compare to the bulk one. This is logical for the LSAT, LAO and YAO substrates, which induces *in-plane* compressive strain, and thus the *out-of-plane* is expected to increase. However, we observe an enhanced *out-of-plane* of PVO/STO film as well compare to bulk PVO, despite an *in-plane* tensile strain. This seems to suggest a possible presence of oxygen vacancies in PVO/STO film, which results in an expansion of PVO cell due to the Colombic repulsion.

To certify this, we estimated the *out-of-plane* lattice parameters (a_{\perp}) of all PVO films based on the lattice mismatches and the Poisson's ratio of PVO, and then compared it with the actual observed *out-of-plane* lattice parameters. Table 4.2 details the possible expansion of unit cell. As the film *out-of-plane* lattice parameter (a_{\perp} (expected)), and epitaxial lattice mismatch (ϵ_{\parallel}) are linked by the Poisson's ratio (ν) as follows [57]:

$$a_{\perp} = \left[1 - \frac{2\nu}{1 - \nu} \cdot \epsilon_{\parallel} \right] a_0$$

where a_0 is the film unstrained lattice parameter. From Table 4.2, we observe that for tensile strain (STO substrate), volume of the pseudo-cubic unit cell has increased as compare to the bulk compound, and the *out-of-plane* lattice parameter is increased by 0.7% compare to the expected one, which can be explained by the presence of oxygen vacancies. On the contrary, for compressive strain, the cell volume is nearly equal to the bulk one ($V_{pc} \sim 59.36 \text{ \AA}^3$), suggesting the absence of oxygen vacancies as reported in CaMnO_3 and SrMnO_3 films [58, 59], and confirming that the observed effect results mainly from epitaxial strain. Finally, for the LSAT substrate, the cell volume is close to the bulk one and the *out-of-plane* lattice parameter is slightly higher than the expected one. This establishes LSAT substrate in an intermediate regime, where the strain is mainly dominated by the epitaxial one with a small amount of oxygen vacancies. After realizing the *out-of-plane* and *in-plane* lattice strain in PVO thin films, we present in the next section the discussion concerning the texture of films.

Table 3.2: Quantification of possible oxygen vacancies in tensile, and compressive strain. The estimation of a_{\perp} (expected) is established based on the lattice mismatch and Poisson ratio of PVO, $\nu \sim 0.39$.

Substrate	Lattice mismatch (%)	a_{\perp} (expected) [Å]	a_{\perp} (actual) [Å]	Expansion (%)	V_{uc} (present Exp. work) (Å ³)
STO	0.10	3.896	3.923	0.70	59.82
LSAT	-0.85	3.950	3.961	0.27	59.26
LAO	-2.93	4.047	3.995	-1.28	58.60
YAO	-5.15	4.157	3.943	-5.14	58.75

3.3 Study of microstructure by TEM: Determination of the epitaxial relationship

To characterize the microstructure of PVO films, the transmission electron microscopy (TEM) analysis was performed for each sample (only PVO/LAO will be shown here). The cross-sectional thin lamellae were prepared, and oriented in order to observe both the *out-of-plane* and *in-plane* of the PVO. Fig. 3.6(a) is an illustrative Selected Area Electron Diffraction (SAED) pattern of a PVO/LAO film, where the enlargement in Fig. 3.6(b) shows a complex splitting of the PVO reflections, marked by green arrows, and could represent the deformation of PVO framework from one domain to the other. Fig. 3.6(c) shows an HRTEM image of a PVO film grown on the LAO substrate, where the interface between LAO and PVO is indicated by yellow arrows, and exhibits contrast perturbation due to strain. The cyan arrows and dotted circles in Fig. 3.6(c) demonstrate the orientation of C_{PVO} *in* and *out-of-plane* of the lamellae plane, respectively. Nevertheless, in most of the observations, we observe C_{PVO} lying *in-plane* of the film, and the diffraction spots related to $2 \times a_c$ along the growth direction are either weak (STO, YAO, LSAT), or non-existent (LAO). This allows, for example for PVO/STO, $\text{PVO}[110]_o \parallel \text{STO}[001]_c$ and $\text{PVO}[001]_o \parallel \text{STO}[100]_c$ or $\text{PVO}[001]_o \parallel \text{STO}[010]_c$ (o and c stands for orthorhombic and cu-

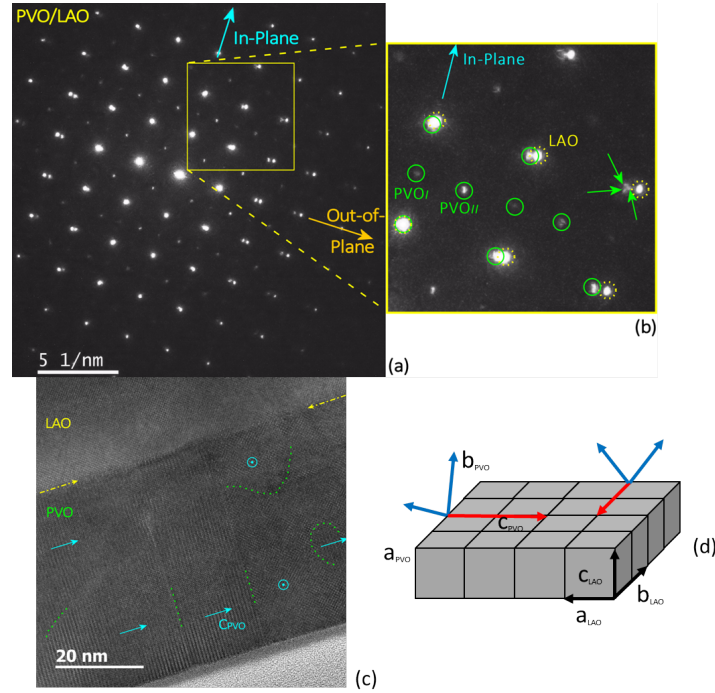


Figure 3.6: (a) Typical SAED pattern of PVO/LAO sample; several patterns can be distinguished, especially along *out-of-plane* direction. (b) Enlargement showing the complex splitting of PVO reflections (green arrows). (c) HRTEM image of PVO film on LAO substrate. The orientation of C_{PVO} is given on several domains. It always lies *in-plane*, either parallelly (cyan solid arrows) or perpendicularly (dotted circle) to the lamella plane. Domains are outlined with dotted lines. The interface between LAO substrate and PVO film exhibits contrast perturbation indicative of strains, depicted by dashed arrows.

bic, respectively). A schematic representation of these two domains, oriented at 90° to each other is shown in Fig. 3.6(d).

3.4 Resistivity measurements

One of the main objective of my thesis is to study the physical properties of PVO films, and to investigate how the strain imposed by different substrates tunes them. In this part, we will explore the electrical properties of PVO thin films, which are collected using four-point probe method.

Fig. 3.7 displays the temperature dependent resistivity $\rho(T)$ measurements of PrVO_3 thin films grown on different substrates. An insulator-like behavior for PVO films grown on LAO, LSAT and YAO substrates is observed. On the contrary, the PVO/STO film displayed a conducting-like behavior (inset of Fig. 3.7). This is likely due to the presence of the oxygen vacancies in

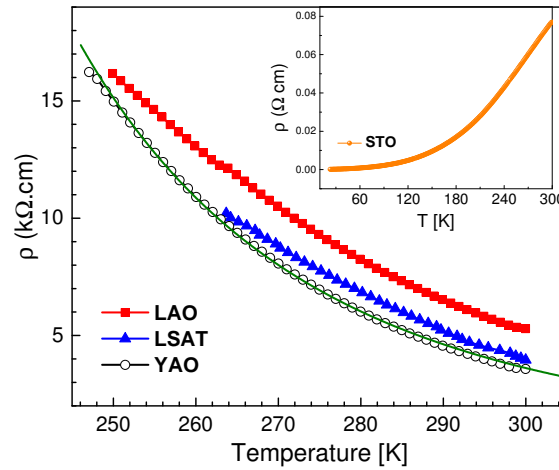


Figure 3.7: Resistivity (ρ) of a series of PVO thin films as a function of temperature (T). The green line is a fit to the Arrhenius equation (see below paragraph). The inset shows plot for PVO/STO.

the STO substrate [60]. At low temperatures, the resistance of films (on YAO, LAO and LSAT) exceeds the limiting value of the experimental setup, and therefore the data are presented only above 250 K. Assuming a thermally activated behavior, expressed by the Arrhenius equation: $\rho = \rho_0 e^{E_A/K_B T}$, we fit the data for PVO/YAO (in green), and the extracted parameters are: residual resistivity $\rho_0 = 0.014 \, \Omega \cdot \text{cm}$ and the activation energy $E_A = 183 \, \text{meV}$. As compare to the bulk PVO parameters [61], $E_A = 179 \, \text{meV}$ and $\rho_0 = 0.36 \, \Omega \cdot \text{cm}$, the value of ρ_0 for PVO film has considerably decreased by an order of magnitude, whereas the activation energy agrees well with that of the bulk value. This difference might arise due to several factors, such as oxygen vacancies, strain induced by substrate and so on.

3.5 Magnetic properties

In this part of the chapter, the magnetic properties of PVO thin films are presented, and their dependence upon the strain applied by various substrates is also discussed.

3.5.1 Hysteresis cycles

In this section, we will explore the magnetic properties of PVO films as a function of magnetic fields H . However, first, it is important to discuss the magnetism of the substrates used in the study. A detailed description on the substrates magnetism is already presented in the chapter 2 (section 2.2.6). While LAO, LSAT and STO substrates are purely diamagnetic, a weak ferromagnetic-like behavior is seen for the annealed YAO substrate (Fig. 3.9(b)). Thus, in order to obtain the true magnetization of the film (Fig. 3.9(c)), the substrate magnetic signal is subtracted from the whole sample signal (Fig. 3.9(a)). But, since the magnetic signal of the substrate is an order of magnitude smaller than the magnetic signal of the whole sample, no significant difference between magnetization of the sample and film is observed. Similarly, the subtraction was performed for other substrates as well, and the magnetization loops at $T = 20 \, \text{K}$

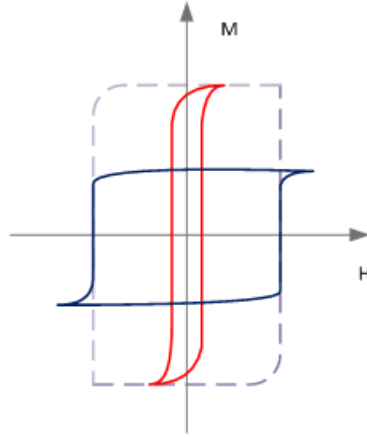


Figure 3.8: A schematic representation of soft and hard magnetic loops, which will combine to give a hysteresis loop shown in Fig. 3.10.

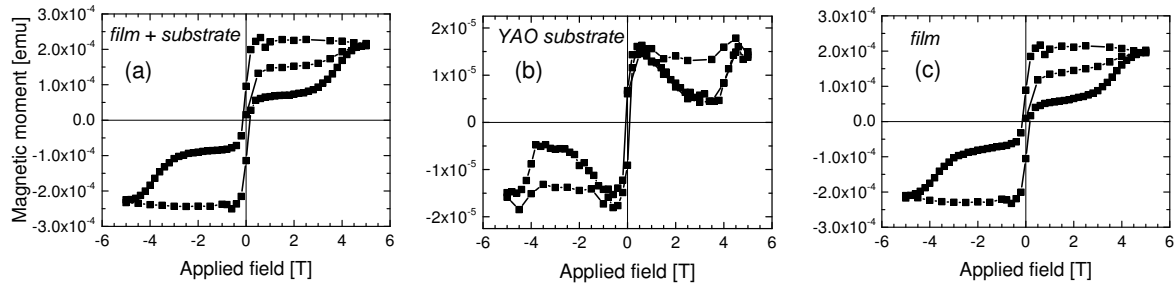


Figure 3.9: Field dependent magnetic moment at $T = 20$ K for (a) PVO film grown on the YAO substrate, as a whole, after diamagnetic background (b) annealed YAO substrate, and (c) the PVO film, which was obtained by subtracting substrate magnetic signal (shown in b) from the whole sample signal (shown in a). The diamagnetic background was removed from each plot.

were obtained for PVO films on different substrates (Fig. 3.10). (The cycles at $T = 10$ K are not completely saturated at 5 T, especially for the LAO substrate, thus the parameters such as coercive field H_c and saturation magnetization M_s cannot be rightfully defined). From the magnetic loops (Fig. 3.10), the following points about PVO films can be drawn:

- A ferromagnet-like behavior;
- Magnetization can be described as an addition of a soft and a hard magnetic contributions, as shown by the schematic in Fig. 3.8;
- Soft magnetic phase is nearly fixed at $H \sim 0.2$ T, while hard one changes with the strain. The extracted coercivity (H_c) from the latter phase is plotted in Fig. 3.10(e) as a function of strain.

Following this, we computed an approximate contribution of each magnetic phase using a method [62]. For instance, $\Delta M_{hard} = 85$ % and $\Delta M_{soft} = 15$ % for PVO/STO, $\Delta M_{hard} = 70$ % and $\Delta M_{soft} = 30$ % for PVO/LAO, $\Delta M_{hard} = 60$ % and $\Delta M_{soft} = 40$ % for PVO/LSAT, $\Delta M_{hard} = 45$ % and $\Delta M_{soft} = 55$ % for PVO/YAO. These observations indicate the sensitivity of each of the magnetic phases to epitaxial strain. Moreover, a large soft component in PVO/YAO film is observed. This behavior will be clarified in the next chapter. The coercive field (H_c), extracted from the hard magnetic phase (specified by arrows), is plotted in Fig. 3.10(e), and detailed in Table 3.3. This shows that the H_c associated with PVO films increases with increase in the compressive residual strain, due to increase in domain wall clamping by the substrate with increase of strain. In similar system, a large strain leads to decrease in the mobility of domain walls and thus large magnetic field is required for the magnetization switching. [63]

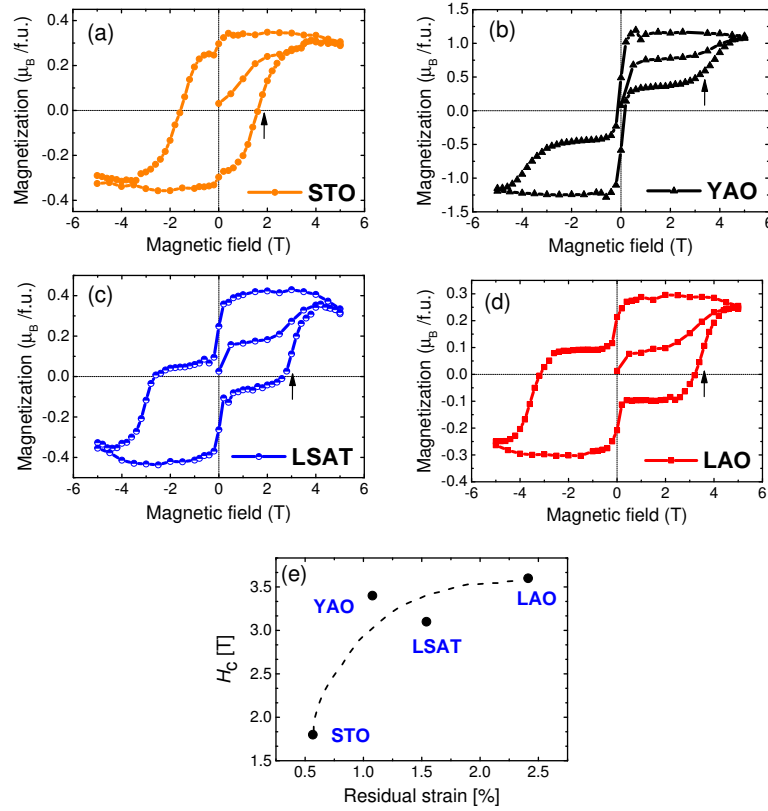


Figure 3.10: (a) - (d) Magnetic hysteresis cycles taken at $T = 20$ K. (e) Plot of the coercive field (H_c) in PrVO_3 films as a function of residual strain. The arrows indicate the hard magnetic phase, using which the H_c is extracted. This typical double hysteresis loop/behavior of PrVO_3 films can be perceived as an addition of soft and hard magnetic phase (see fig. 3.8). The dashed lines are only guide to the eyes.

Table 3.3: Summary of the pseudo-cubic unit cell volume (V_{pc}), coercive field (H_c), Néel temperature (T_N) of PVO films on different substrates.

Substrate	Lattice mismatch (%)	V_{pc} (\AA^3)	H_c (T)	T_N (K)
STO	0.10	59.82	1.8	30
LSAT	-0.85	59.26	3.1	90
LAO	-2.93	58.60	3.6	100
YAO	-5.15	58.75	3.4	85

3.5.2 Magnetic orderings in PrVO_3 films: MT measurements

In order to further investigate the strain effect on the magnetic properties of PrVO_3 thin films, we performed the Field Cooled (FC) and Zero Field Cooled (ZFC) measurements at an *in-plane* applied magnetic field of $H = 50$ Oe. However, for the sake of clarification, only representative FC plots are displayed in Fig. 3.11(a). From these plots, the substrates magnetic contributions have been removed in order to observe the net magnetizations of the films. Fig. 3.11(a) shows the temperature dependence of the normalized magnetization, and the magnetic orderings in PVO thin films are revealed by the derivative of the magnetization (Figs. 3.11(b-e)). We can see the magnetic signal rising at around 100 K for PVO/LAO and ~ 30 K for PVO/STO, which is ascribed to the magnetic ordering of the vanadium sublattices, and referred henceforth as the Néel temperature (T_N). Notably, the T_N of PVO/STO has decreased (from 80 K to 30 K) compare to the work of Copie et. al. [41]. This discrepancy can be understood from the difference of growth conditions: in cited reference [41], $P_{O_2} = 10^{-5}$ mbar and $T = 600$ °C were used for the growth of film, which are different from our growth conditions (see section 3.1.1).

The estimation of T_N is realized by plotting the derivative of magnetization as a function of temperature, where the transition from paramagnetic to antiferromagnetic (AFM) state is represented by the minimum of the derivative, also marked by arrows. Below the marked transitions, the vanadium spins align in an AFM manner, and thus regarded as the Néel temperature. While for bulk PrVO_3 compound, this transition is assigned to the onset of a C-type Spin Ordering (C-

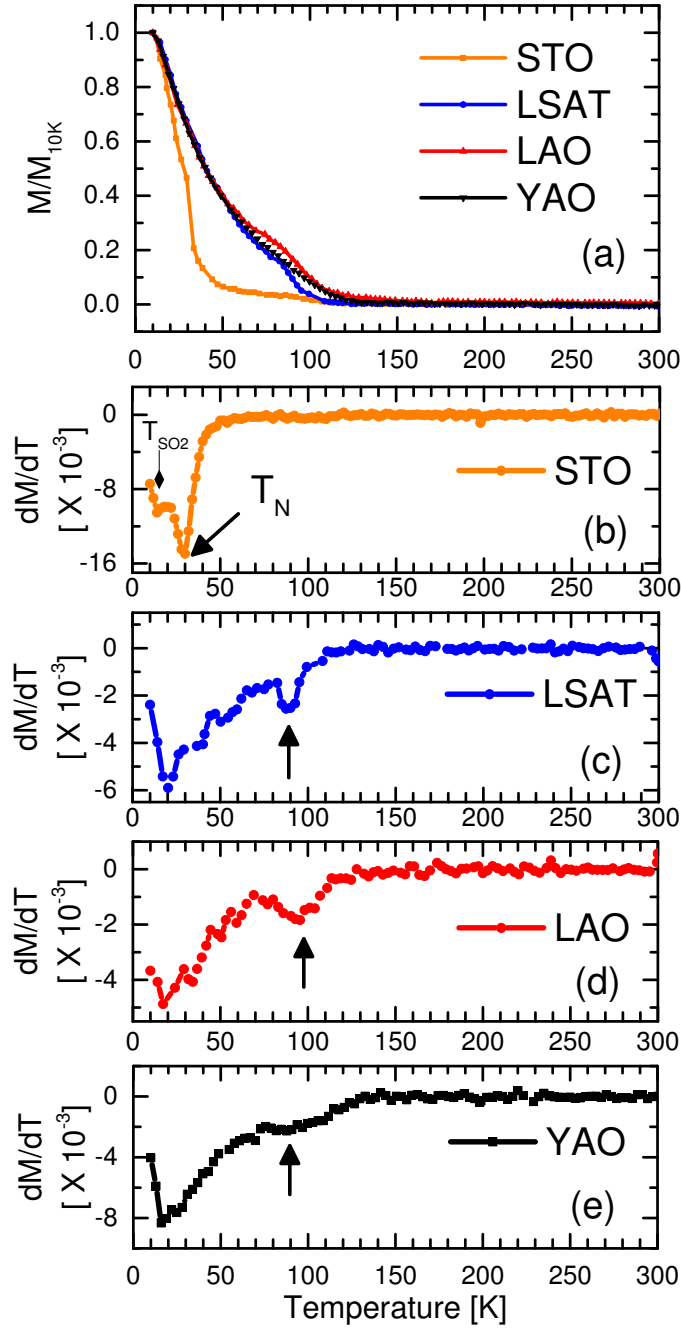


Figure 3.11: The temperature dependent Normalized magnetization (ratio of magnetization to the magnetization recorded at 10 K), along with the derivative of magnetization for PVO films grown on various substrates. The arrow in the derivative curves shows the onset of Néel temperature (T_N). The substrates magnetization were subtracted in order to obtain true magnetization of the films.

SO) of the vanadium moments, for epitaxial PrVO_3 thin films grown on the STO substrate, the DFT calculations predict that substrate-induced strain leads to the G-type Spin Ordering (G-SO) [42]. The PVO films are grown under tensile strain on the STO substrate, and under nominal compressive strain on the LSAT, LAO and YAO substrates. The tensile (compressive) strain in PVO films would essentially increase (decrease) the V-V nearest neighbour distance, and thus reduces (enhances) exchange integral leading to a decrease (increase) in the value of T_N .

Notably, the MT plots also exhibit an extra magnetic feature at low temperature, denoted by T_{SO2} (see Fig. 3.11), where the slope of the magnetization is also minimal. This magnetic feature is surprisingly absent in the bulk PrVO_3 [67] compound, but has been reported for other ortho-vanadates with smaller R size (R : rare earth element) [68, 69, 70]. In addition, Reehuis *et. al.* clearly distinguished this transition for a doped $\text{Pr}_{1-x}\text{Ca}_x\text{VO}_3$ compound [71]. Upon decreasing the temperature to T_{SO2} , a small hump at $T \sim 20$ K can be seen, which could represent the emergence of another type of spin configuration and/or a phase coexistence between C-SO and G-SO. Indeed, as it has been shown earlier, the praseodymium sublattice begins to get polarized due to the presence of exchange field produced by the vanadium sublattice, resulting in a ferromagnetic structure [71]. In order to investigate this phenomenon, the M versus H at different temperatures have been recorded (Fig. 3.12). Below T_N , the change in the shape of hysteresis loops clearly indicates the emergence of the magnetic ordering in PVO films. Above T_N , the hard cycle in the hysteresis loop is still open at 5T, and could possibly represent the presence of a short range magnetic ordering or an intermediate magnetic ordering region where moments are neither completely paramagnetic nor antiferromagnetic. This is partly shown in the inset of Fig. 3.12(b), where above $T \sim 170$ K (for LAO), the inverse susceptibility can be well fitted in the paramagnetic region using the Curie-Weiss law, and region between the dashed lines could represent an intermediate ordered phase. However, a complete magnetic ordering of the vanadium sublattices takes place at a lower temperature at $T_N = 100$ K.

To further understand the relationship between the magnetic properties and strain or distortion (ratio of *out-of-plane* to *in-plane* lattice parameters), the T_N versus lattice strain is shown in Fig. 3.13. We observe that the T_N of the PVO films increases monotonically with the strain, and is highest for LAO ($T_N \sim 100$ K) and lowest for STO substrate ($T_N \sim 30$ K). Moreover, due to

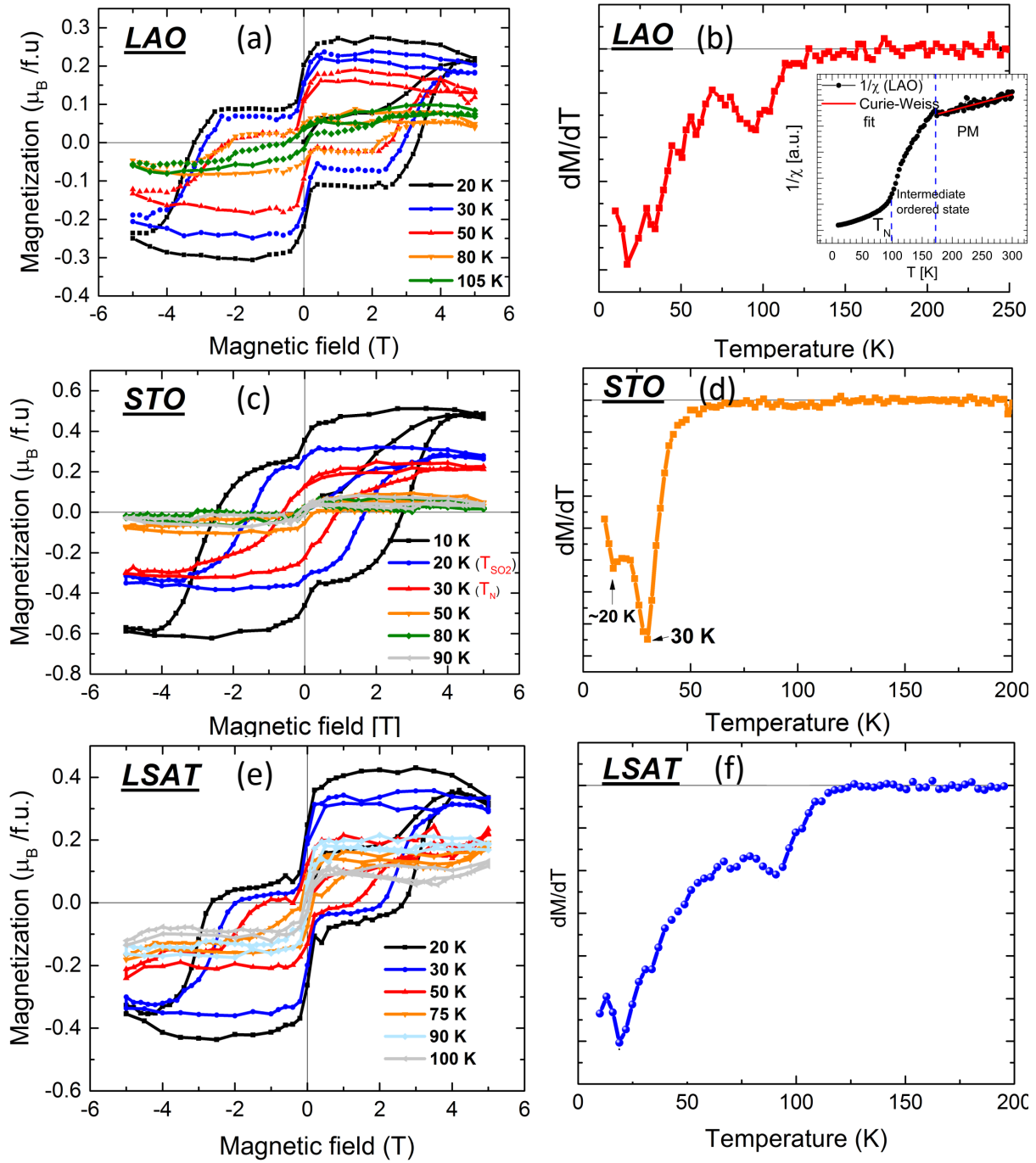


Figure 3.12: MH hysteresis loops of PVO films obtained at different temperatures, for LAO (a), STO (c) and LSAT (e) substrates, and their respective dM/dT versus temperature are shown in (b), (d) and (f). Inset of Fig. (b) shows temperature dependence of the inverse susceptibility of PVO film on LAO substrate, where red line is the Curie-Weiss fit in the paramagnetic region, and the region between two dashed lines represents an intermediate ordered phase.

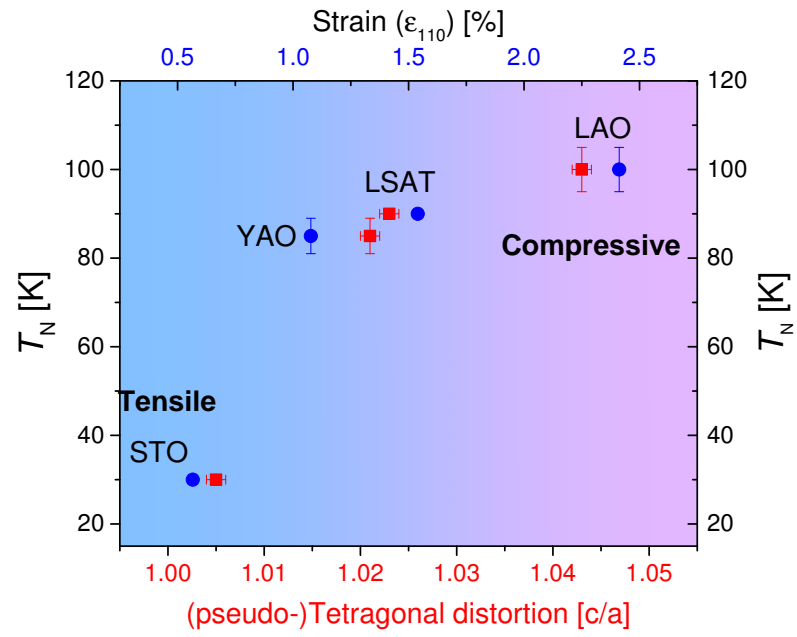


Figure 3.13: The Néel temperature T_N of PVO films as a function of the tetragonal distortion (ratio of *out-of-plane* to *in-plane*) (bottom scale), and strain (top scale).

relaxed behavior of the PVO film on YAO substrate, one expects a T_N close to the bulk one (~ 130 K), but the out-of-plane lattice parameter is larger than the bulk lattice parameter, may be due to oxygen vacancies, which produces a distorted structure with c/a ratio ~ 1.02 , and thus could favor lower T_N . It is interesting to note that the tensile strain (STO substrates) in PVO films reduces the T_N extensively, while the compressive strain (LSAT, LAO, YAO substrates) leads to an increase of T_N .

To further explore the magnetic properties of PVO films and their dependence on the strain, which leads to a tilting of BO_6 octahedra or change in the B-O-B bond angle [72, 73, 74, 75, 76], it is necessary to have a complete knowledge of distortion of the structure and the VO_6 -octahedral rotation. The degree of rotation of VO_6 octahedra depends strongly on the sign and magnitude of the strain [75, 76]. Under *in-plane* tensile strain ($c/a < 1.01$), the VO_6 octahedron comprises of an enhanced *in-plane* V-O bond length and the V-O-V bond angle close to 180° . This decreases the *in-plane* AFM superexchange interaction between the adjacent V sites, and hence the reduced T_N . On the other hand, under *in-plane* compressive strain ($c/a > 1.01$), it is the other way round *i.e.* a reduced *in-plane* V-O bond length and V-O-V bond angle $< 180^\circ$. This, as a result, enhances the *in-plane* AFM interaction and therefore an enhanced T_N .

3.6 DFT calculations

These calculations were performed by Julien Varignon (CNRS, Thales).

To get further insights on the role of the epitaxial strain on the magnetic properties of PrVO_3 films, we have performed *first-principles* simulations using Density Functional Theory (DFT). Consistently with previous studies [65], DFT correctly predicts that bulk PrVO_3 is a C-SO insulator in the ground state. Regarding the thin films, we find that the perovskite grows with the (001) and (1-10) $Pbnm$ axes aligned along the substrate for all the tested films (*e.g.* PrVO_3 grown on STO, LSAT, LAO and YAO substrates, see insets of fig. 3.14(b) for sketches of local axes and

growth orientation). This yields films grown along the orthorhombic (110) direction, in sharp agreement with experiments. We emphasize here that due to the presence of small domains in the films (inducing a mechanical constraint [65]), we have considered growth conditions with the $(110)_o$ direction forced to be orthogonal to the substrate (*i.e.* the film is not allowed to tilt). With that additional constraint, the ground state is associated with a $P2_1/m$ symmetry with nearest neighbor V^{3+} spins antiferromagnetically coupled in all crystallographic directions. It yields a G-type spin ordering compatible with experiments. Finally, all films are insulating with band gaps ranging from 1.50 eV (YAO) to 1.78 eV (STO).

Although mean-field methods such as DFT can not provide accurate values of the Néel temperature, they nevertheless remain valuable technics for capturing trends as a function of external stimuli [80]. We report on Fig. 3.14(a) the ratio of the Néel temperature with respect to that of PrVO_3 grown on a STO substrate as a function of the pseudo tetragonality c/a of the films extracted from our simulations. As one can see, DFT captures the trend observed experimentally with an enhancement of the Néel temperature going from STO to YAO substrates, although our computed $T_N/T_{N-\text{STO}}$ ratio is smaller than the experimental one for the LAO substrate. Amazingly, if the material could be stabilized on YAO without relaxation of the film, the Néel temperature is expected to be approximately multiplied by two with respect to that of PrVO_3 films deposited on STO.

Along with validating the experimentally measured trend for T_N as a function of the applied epitaxial strain, our *first-principles* simulations also provide microscopic insights on the origin of this physical behavior. We observe that both magnetic constants J_1 and J_2 between nearest V^{3+} neighbors along the (1-10) (or (110)) and (001) directions, respectively, increase with enlarging the compressive epitaxial strain. Firstly, this is ascribed to shorter V-O bond lengths along the (1-10) and (001) directions induced by strain. Secondly, we do not observe any significant modifications of oxygen cage rotations amplitude in the different films – the $a^-a^-c^0$ rotation amplitude is even slightly increasing with decreasing the substrate lattice parameter – and thus the classical “ $\widehat{V-O-V}$ angles going to 180° ” argument cannot explain the strengthening of J s. Nevertheless, we find a crossover between two lattice distortions as a function of the epitaxial strain (see fig. 3.14(b)): (i) for a moderate lattice mismatch (*e.g.* STO and LSAT), we extract a

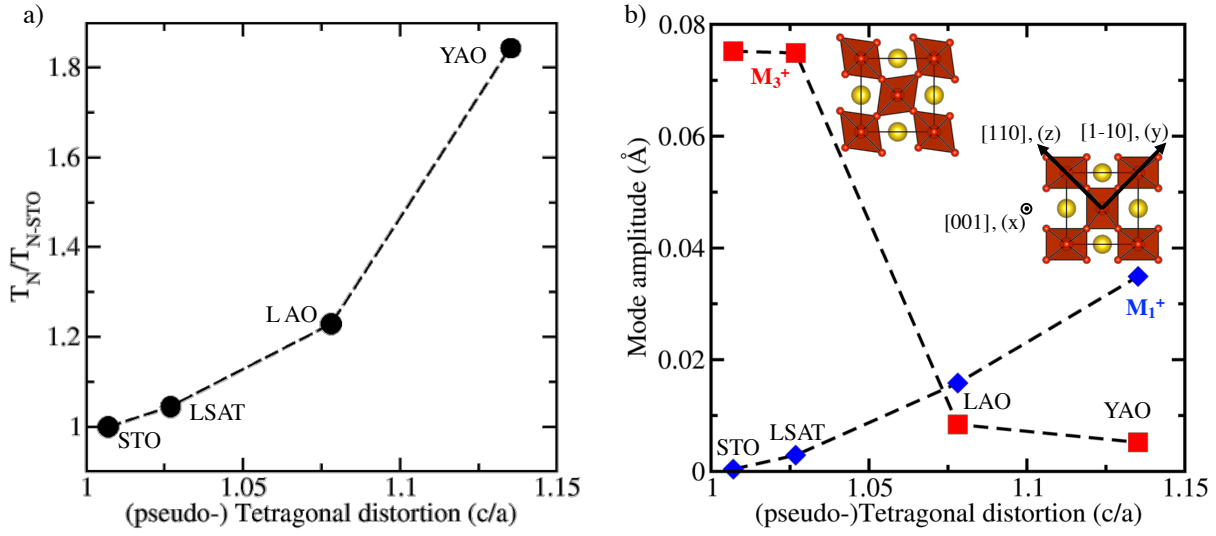


Figure 3.14: Relative evolution of the Néel temperature (a) and of the amplitude of the M_3^+ and M_1^+ distortions as a function of the pseudo-tetragonality of the PrVO_3 films. Sketches of the structural distortions and local axes are presented as insets.

large Jahn-Teller distortion, labelled M_3^+ , producing an asymmetry of V-O bonds on nearest V sites that is reminiscent of bulk RVO_3 physics and (ii) for a large lattice mismatch (*e.g.* LAO and YAO), the JT motion vanishes and is replaced by a M_1^+ distortion unaffected V-O bond lengths but distorting O-V-O angles in VO_2 planes orthogonal to the (001) direction (see insets of fig. 3.14(b) for sketches of the distortions). The amplitude of the latter distortion, absent in the bulk and roughly zero for films grown on STO and LSAT substrates, closely behaves like T_N as a function of the tetragonality of the material. In fact, the crossover between the amplitude associated with the M_1^+ and M_3^+ distortions highlights a clear modification of the electronic structure: the two V^{3+} d electrons are located in the d_{yz} orbital plus an alternating combination of the $d_{xz} \pm d_{xy}$ orbitals on neighboring sites for moderate strains while they lie in the d_{xz} and d_{yz} orbitals on all neighboring sites for large compressive epitaxial strain (see insets of Fig. 3.14(b) for the definition of local axes). It follows that V-O bond length contractions combined with the modifications of V^{3+} d orbital occupancies for LAO and YAO substrates favor superexchange in the three crystallographic directions and thus strongly promotes the enhancement of the Néel

temperature.

3.7 Conclusions and perspectives

It is important to highlight that, to study the structure of a thin film, defining the texture, and establishing a correlation between structure and magnetism, always remain a complicated job due to presence of substrate and the particular geometry of the sample. The present study however demonstrates a spin-orbit-lattice coupling in PrVO_3 thin films. For instance, the most distorted film on the LAO substrate with $c/a \sim 1.04$ associated with compressive mismatch of $\sim -2.9\%$ have the highest Néel temperature around 100 K. Whereas the film grown on the STO substrate is the least distorted one with $c/a \sim 1$, and a lower Néel temperature ~ 30 K. Therefore, the compressive strain in PrVO_3 films clearly favors the superexchange interaction. The DFT calculations not only validate the experimentally observed trend of T_N vs. strain, but also predicts a change in the electronic structure of PrVO_3 thin films with increase of strain. The presence of two magnetic phases in the hysteresis cycles remains unclear at the moment. Different hypothesis can nevertheless be brought forward:

1. Some double hysteresis loops have also been observed on other systems, such as orthoferrites RFeO_3 , where R is Rare-earth element. In these weak ferromagnet materials, due to canted antiferromagnetic alignment of the Fe^{3+} magnetic moments, thin films of SmFeO_3 present the soft magnetic phase in polycrystalline form. Nevertheless this soft component was attributed to garnet or magnetite impurity phase. [62, 77]

In the case of epitaxial orthoferrite films, such as YFeO_3 , the hysteresis loops are also composed of two magnetic components; a soft component below 0.1 T and an S shaped at higher field. These two components result from different variants in the film. For a magnetic field applied along the direction of the canting, the net moment reverse with a coercive field of 0.1 T. At the contrary, for other variant, when the magnetic field is applied along the antiferromagnetic axis, a spin reorientation occurs with a high coercivity. [78, 79]

However, in our films, only the variant with the long axis in-plane is present (See Fig. 3.6). Therefore, it is difficult to explain the soft component in our films based on this hypothesis.

2. Another possibility is the presence of dead layer on the surface of the film. As the vanadate films have tendency to get oxidized on the surface [38, 86], a dead layer can be formed and bring some magnetic component [85].

This second hypothesis will be investigated in the next chapter with the use of capping layer and surface measurements such X-ray photoelectron spectroscopy (XPS).

Chapter 4

STRAIN ENGINEERING IN PrVO_3 THIN FILMS: FILM THICKNESS AND CRYSTAL ORIENTATION DEPENDENCE

In the previous chapter, we described the strain engineering of PrVO_3 thin films by employing several single crystal substrates, and presented the strain-dependent magnetic properties. Other well established methods to achieve a range of strain states in thin films are discussed in the present chapter. The first part of the chapter deals with the film-thickness-dependent physical properties of PrVO_3 thin films, where film thickness is varied on the LAO and LSAT substrates. The second part of the chapter aims to discuss the structural and magnetic properties of the PrVO_3 films grown on SrTiO_3 substrates with different orientations.

4.1 Strain engineering via changing PrVO_3 film thickness

Controlling the layer-by-layer film thickness through minute deposition undoubtedly offers fascinating properties, namely, spin-glass behaviour in compressively strained BiFeO_3 thin films [81], thickness dependent magnetic anisotropy in $\text{La}_{2/3}\text{Ca}_{1/3}\text{MnO}_3$ films [82] or the dimensional crossover of magnetization from 3D to 2D in SrRuO_3 thin films [83]. Nevertheless, it certainly remains a less investigated topic in vanadates thin films so far, particularly for PrVO_3 thin films. In this chapter, we therefore present the film thickness-dependent structural and magnetic properties of PrVO_3 thin films.

4.1.1 Growth conditions

The growth of PrVO_3 thin films was carried out by using the PLD chamber installed at the CRISMAT laboratory, Caen. The utilized substrates were LaAlO_3 (100), and $(\text{La,Sr})(\text{Al,Ta})\text{O}_3$ (LSAT) (100), as-received from *CrysTec*. We have seen in the previous chapter that, a 50 nm PVO film is epitaxially strained on the LSAT substrate, whereas, it is partially relaxed on the LAO substrate. Therefore, we have chosen these two aforementioned substrates in order to study the thickness dependence on the strain. The film thickness was varied between $\sim 10 - 100$ nm. The utilized growth conditions were:

- substrates: LaAlO_3 (001), LSAT (001);
- target: polycrystalline PrVO_4 ;
- film thickness (t): $\sim 10-100$ nm;
- substrate temperature: 650°C ;
- atmosphere: under vacuum (10^{-6} mbar);
- substrate to target distance: 5 cm;

- laser KrF ($\lambda = 248$ nm) Excimer: 2 Hz, 200 mJ.

4.1.2 Preliminary structural observations by XRD

The first concern after synthesis of films was to ensure the right phases, smooth interface between film and substrate, which was acquired by performing a wide range $\theta - 2\theta$ scan and rocking curves using conventional XRD technique. This also allowed us to determine the *out-of-plane* and *in-plane* lattice parameters of PVO films grown on LAO and LSAT substrates as detailed below.

Out-of-plane structure

Fig. 4.1 displays the $\theta - 2\theta$ x-ray diffraction measurements of PVO films on LAO and LSAT substrates in the vicinity of pseudocubic (001) reflection. At first glance, we observe that PVO/LSAT films present clear thickness fringes, indicative of well defined interface between film and the LSAT substrate. Whereas these representative fringes are quite small, and suppressed for PVO/LAO films, presumably due to presence of inherent twin domains in the LAO substrate. The film thickness was actually estimated by fitting these fringes with a simulation, as explained earlier in section 3.2 (Fig. 3.3).

The *out-of-plane* lattice parameters of PVO films, extracted from the $\theta - 2\theta$ scans, are plotted in Fig. 4.2 (upper panel, represented by \perp). Firstly, we observe that the *out-of-plane* lattice parameters of PVO films has increased as compare to the bulk pseudocubic $a_{pc} = 3.901$ Å, in agreement with the *in-plane* compressive strain imposed by both the substrates. Secondly, it remains nearly constant for PVO/LSAT films, and reside within the error bars (calculations of which are given in *Annex section*). For PVO/LAO films, the *out-of-plane* tends to decrease with increase of film thickness, a characteristic of relaxing behavior of the film under compressive strain. This typical behavior for PVO/LAO films can be rather expected due to a large mismatch between bulk PVO and the LAO substrate (~ -2.9 %).

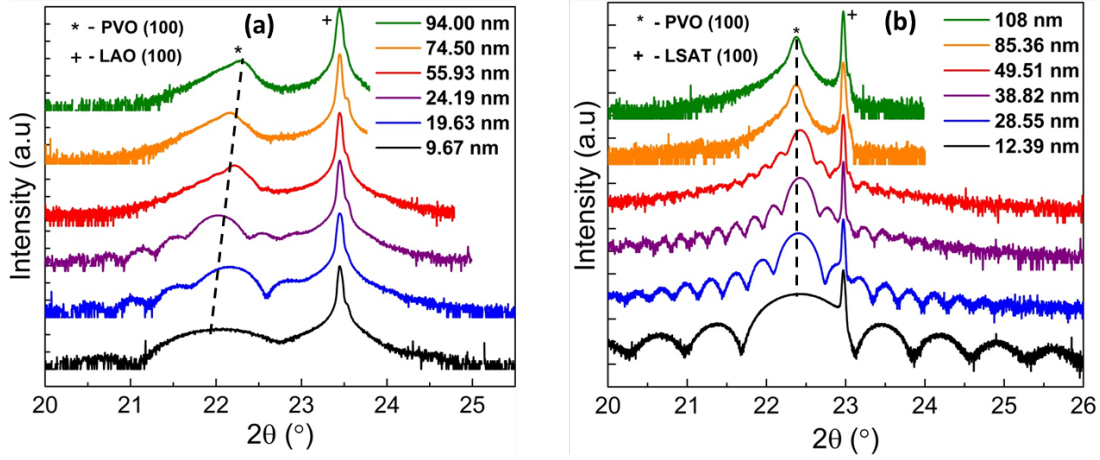


Figure 4.1: $\theta - 2\theta$ x-ray diffraction measurements of a series of PVO films on (100)-oriented LAO (a) and LSAT substrates (b) around pseudocubic (100) of the substrates. The asterisk (*) and plus (+) symbols represent the PVO film and substrate, respectively. The dashed lines are only guide to the eyes.

In-plane structure

To quantify the *in-plane* lattice parameters of PVO films, asymmetrical reciprocal space maps were recorded around $(103)_{pc}$ reflection of both the substrates (Fig. 4.3). We note that the thinner PVO film ($t \leq 24$ nm) is *in-plane* strained with the LAO substrate but thicker films are partially relaxed, as the position of films peak along the horizontal Q_{in} axis shifts toward lower value. This is in perfect agreement with the highly mismatched PVO film grown on the LAO substrate, which tends to relax easily over small thickness, due to a decrease in the strain states as the thickness increases. The extracted *in-plane* lattice parameters from these maps are plotted (within the instrumental error) in Fig. 4.2 (lower panel, represented by ||) as a function of film thickness. On the LAO substrate, the *in-plane* lattice parameter of film increases linearly with the film thickness. This behavior is typical of a partially relaxed film, and is in accordance with a decrease of *out-of-plane* lattice parameter with increase of t , for a film with an ideal Poisson's

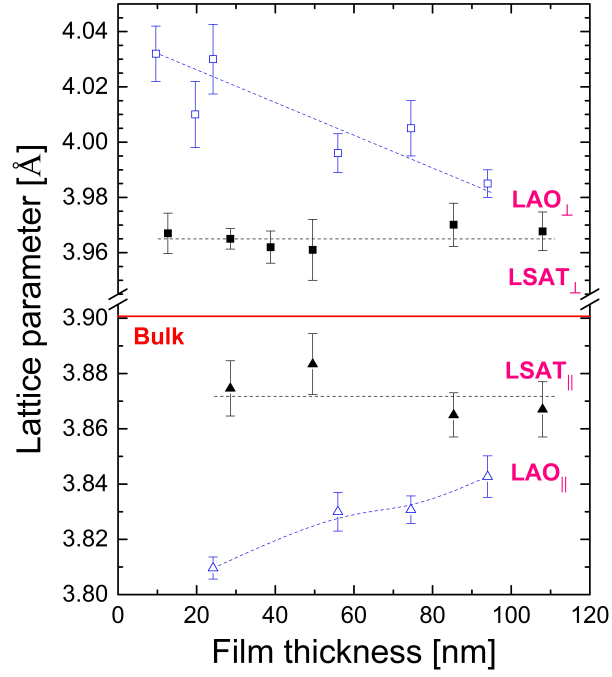


Figure 4.2: The *out-of-plane* (square symbols in top panel) and *in-plane* (triangle symbols in bottom panel) lattice parameters of PVO films on LAO (blue open symbols) and LSAT (black close symbols) substrates, as a function of the film thickness, plotted along with the error bars. \perp and \parallel symbols represent the *out-of-plane* and *in-plane* lattice parameters of PVO, respectively. The dashed lines serve as guide to the eyes. Red line indicates PVO bulk *pseudo-cubic* lattice parameter.

ratio. On the LSAT substrates, the situation is different as the PVO films are strained with the substrate. This is clearly seen in Fig. 4.3(b), where the horizontal position of film peak coincides with the one of LSAT substrate. Following this, we extract that the film and substrate have the same *in-plane* pseudocubic lattice parameters.

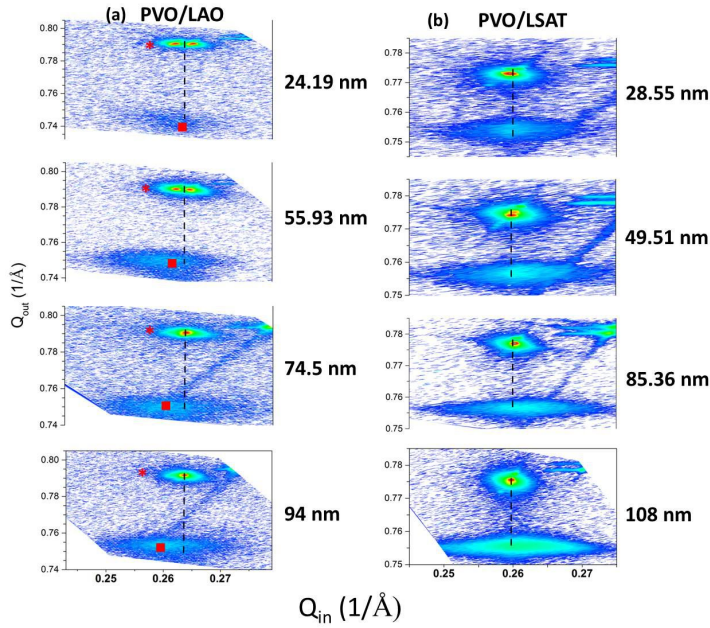


Figure 4.3: Asymmetrical Reciprocal Space Maps (RSMs) performed for a series of PVO thin films grown on (a) LAO and (b) LSAT substrate, around *pseudo-cubic* (103) of the substrate. The horizontal axis is Q_{in} and vertical axis is Q_{out} for all RSMs. The substrate and film peaks are located in the upper and lower region of RSMs, and marked by the asterisks and solid square symbols respectively, for both substrates. The double peaks for the LAO substrate are due to twin domains in the substrate. The vertical dashed lines are only guide to the eyes.

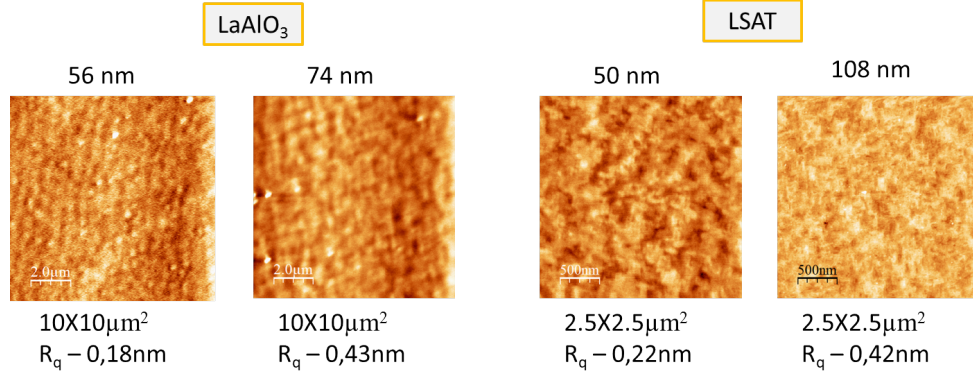


Figure 4.4: AFM images of PVO films grown on the LAO and LSAT substrates, where the surface roughness R_q is also given.

Discussion

Given a large lattice mismatch between PVO and the LAO substrate, it is rather unambiguous to foresee this relaxing behavior of PVO/LAO films. For PVO films on LSAT substrates, a small mismatch between PVO and the LSAT substrate keeps films strained with the substrates, even for thicker films. In addition, our surface microscopy results confirm a smooth surface of all the samples, with a surface roughness R_q slightly increases with increase in film thickness, but remains less than 0.5 nm even for thicker films. To clarify, few AFM images have been depicted in Fig. 4.4. Apart from this, the pole figures for all thicknesses were performed in order to globally realize the epitaxy of PVO films. For an orthorhombic cell, it is possible to discriminate between different variants of PVO with (111) plane. Indeed, in the configuration “ $[110]$ -axis lying in-plane”, (111) plane should be diffracted at $\psi = 63.3^\circ$, whereas in configuration for “ $[110]$ -axis lying out-of-plane”, the (111) plane should be diffracted at $\psi = 26.6^\circ$. Based on our preliminary results, we observed the intensity peak only for $[110]_o$ *out-of-plane* ($[001]_o$ *in-plane*) case (at $\psi \sim 26.51^\circ$), and no signal was seen for the scenario when $[110]_o$ *in-plane*. Thus, all the films appear to have a single $[110]_o$ growth orientation.

4.1.3 Magnetic properties

After having some understanding about the structure of PVO films *i.e.* *in-plane* and *out-of-plane* lattice parameters, epitaxy etc, we will now discuss the effect of layer thickness on the magnetic properties of PVO thin films. We will start with the magnetization measurements as a function of magnetic field, which were carried out using the SQUID magnetometer equipped with a 5T solenoid coil.

Hysteresis cycles: Dead layer at the surface of PVO films

Fig. 4.5 displays the magnetization-magnetic field (M - H) measurements performed at $T = 30$ K for PVO films on the LAO and LSAT substrates with various film thicknesses. In order to clearly observe the PVO magnetic contribution, the substrates magnetic signals (section 2.2.6, page 65) were subtracted from the whole measured signal. First, we observe an opening of the MH loop with the increase of film thickness, evidencing a ferromagnetic-like behavior of the PVO films. Second, the magnetization of films could be described as a combination of a soft and a hard magnetic phase, as explained in the previous chapter.

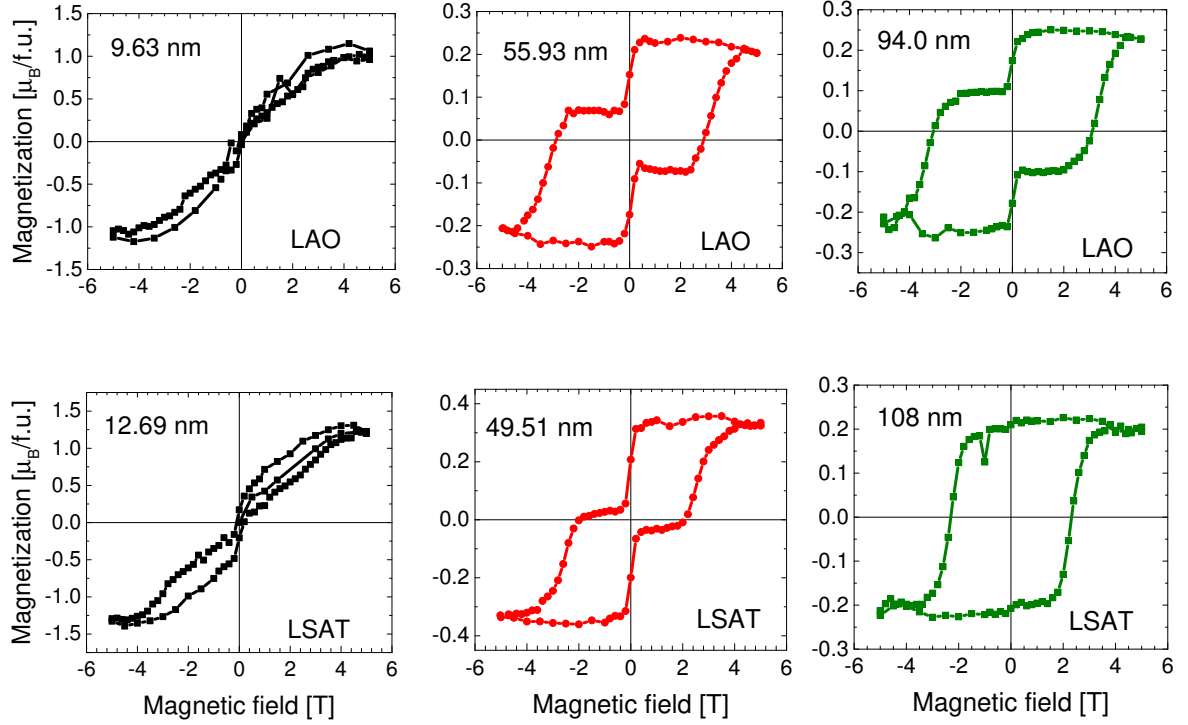


Figure 4.5: The magnetic hysteresis cycles of PVO films grown on LAO and LSAT substrates, taken at $T = 30$ K, for different thicknesses.

The coercive field (H_c) extracted from the hard magnetic phase, saturation magnetization (M_s) and the remanent magnetization (M_R) are plotted as a function of film thickness in Fig. 4.6. A continuous decrease in M_s and increase in H_c are observed for both the substrates with increase in the film's thickness, until a nominal value is reached, which remain nearly constant for the thick films. (This typical trend of M_s and H_c with increase of film thickness remains true for any measured temperature (20 – 50 K)) Additionally, the shape of hysteresis loop changes from a square like MH to a paramagnetic like S-shaped as thickness is reduced (Fig. 4.5). We suggest here that a large value of M_s for thinner films is reminiscent of the presence of a non-magnetic/paramagnetic layer at the surface of film, namely a “dead layer”, similar to the previous

observations in DyTiO_3 thin films [85]. Actually, when film surface is exposed to air, the surface of film can get over-oxidized, and the magnetic V^{3+} ions can indeed be replaced by V^{4+} or non-magnetic V^{5+} ions, decoupling Pr^{3+} ions. This over-oxidized phase is commonly observed on vanadate films surface such as LaVO_3 or SrVO_3 . The surface of the films are not stable and tend to over-oxidize [38, 86]. Our high resolution TEM image of a PVO film on the LAO substrate (Fig. 3.6(c)) shows such amorphous PVO on the surface of film of a few nanometers. This amorphous phase could lead to isolated Pr atoms, which release their strong paramagnetic response. In order to estimate the thickness of the dead layer, we will use a classical model that incorporates two magnetic layers [85]. Finally, the oxidation of the surface will also be investigated with the XPS measurements on the surface of the films in the next section.

Quantification of dead-layer thickness

To estimate the thickness of this layer, we used a classical model described by equation 4.1, which assumes that this layer is paramagnetic, has null magnetization at remanence, and has a huge magnetization at high fields. The thickness-dependence of remanent magnetization (M_R) and saturation magnetization (M_s) are fitted with the proposed dead layer model, using the following equation:

$$M_{tot.} = m_{tot.}t = m_P t_P + m_{AF} t_{AF} \quad (4.1)$$

$$m_{tot.} = (m_P - m_{AF})t_P/t + m_{AF} \quad (4.2)$$

where, $t = t_P + t_{AF}$ is the total thickness of film, t_P is the thickness of paramagnetic layer, t_{AF} is the thickness of antiferromagnetic layer, m_P is the moment per unit volume of the paramagnetic layer, m_{AF} is the moment per unit volume of the antiferromagnetic layer. With $m_{AF} \sim 0.7 \mu_B/\text{f.u.}$ (f.u.: formula unit) [88] (for bulk PVO) and $m_P = 0$ (for M_R), a dead layer thickness t_P of ~ 6 nm for LAO (Figure 4.6(c)) and ~ 4 nm for LSAT (Figure 4.6(d)) was obtained by fitting the remanent magnetization. Furthermore, setting m_P to the maximum magnetization of the thinnest sample and using t_P as fitting parameter, we evaluated $t_P \sim 6 - 7$ nm from fitting of

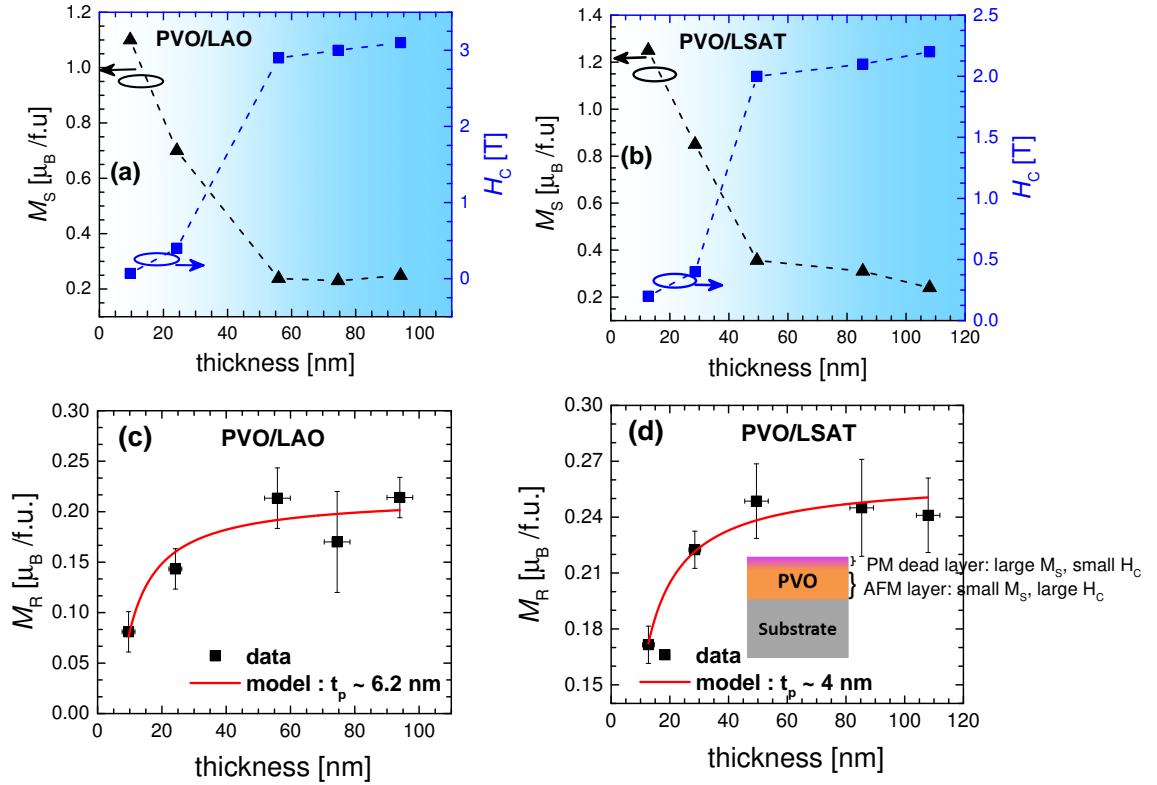


Figure 4.6: A plot of saturation magnetization (M_s), remanent magnetization (M_R) and coercive field (H_c) as a function of PVO film thickness. The red curve in (c) and (d) is a fit for equation 4.1 using a classical dead layer model. The inset of (d) is a scheme of our PVO thin film, with a paramagnetic dead layer on the top.

M_s vs t .

Remarkably, a similar trend in H_c and M_s was also observed for ferrite thin films, which likely indicated a change in the magnetization spin axis, in addition to a reorientation of the domains above critical thickness [95, 96]. In PVO thin films, however, a strong paramagnetic response of thinner films is indicative of dead layer at the film's surface, which consists isolated Pr^{3+} atoms. In addition, a decrease of M_s with increase in film thickness is also evidenced by a decrease in the fraction of film that is made up of the paramagnetic phase. Likewise, the increase of H_c with increase of film thickness could be related to the increase in the density of pinning sites due to increase in the number of domains, and/or domain boundaries. Indeed, due to a partial strain-relaxation, the film could energetically favor multiple domains, as shown earlier [97]. For thick PVO films, the magnetization and coercive field approach a nominal value, meaning that the magnetic contribution from each layer is static, and independent of film thickness.

Reviving PrVO_3 thin films magnetic properties: Capping of PVO surface

So far we have discussed the presence of two magnetic phases in PrVO_3 thin films, and their dependence upon film thickness. We speculated that a dead layer at the surface of film, containing isolated Pr atoms, is responsible for the soft magnetic phase in the hysteresis cycles. To confirm our hypothesis, and to extract the magnetic properties of PrVO_3 thin films (excluding the contribution from dead layer), we have explored the possibility to reduce the film surface by capping it with few layers of LAO. The capping of PVO film surface with the reducing material LAO essentially diminishes the formation of $\text{V}^{4+} / \text{V}^{5+}$ at surface, and thus minimizes the contribution of dead-layer. Following this, we capped PVO film with ~ 8 nm of LAO grown in the same deposition conditions. Fig. 4.7 illustrates magnetic hysteresis loops, recorded at $T = 20$ K, of an approximately 50 nm PVO thin film, with and without capping layer. Fig. 4.7(b) shows a clear decrease of the soft magnetic component for the capped film, concomitant with the hypothesis of dead layer. For the hard magnetic phase, the remanent magnetization, saturation magnetization and the coercive field are almost the same. This leads to an important conclusion of the chapter; the soft magnetic component in M versus H is certainly a film-surface-related phenomenon. A

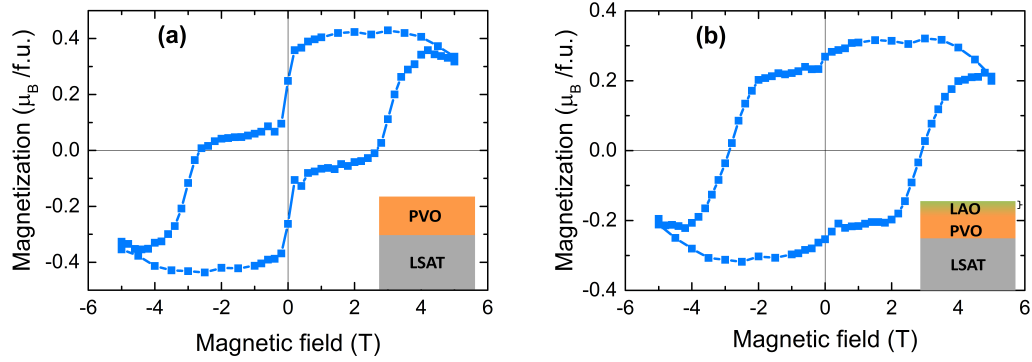


Figure 4.7: Magnetic hysteresis cycles at 20 K of a ~ 50 nm PVO/LSAT film uncapped (a), and capped with ~ 8 nm thick LAO (b).

residue of soft phase even after the capping of film could suggest a minor contribution from the interface. It could be argued that, the reduction of the soft magnetic phase is associated with the strain applied by the top LAO layers on few layers of PVO film, or vice versa. In this regard, we have investigated the x-ray photoelectron spectroscopy of both (bare and capped) films in the next section.

X-ray Photoelectron Spectroscopy (XPS)

In order to confirm the origin of the dead layer on a PVO film on the LSAT substrate, we have investigated the valence states of the vanadium atomic species at different probing depths, by using X-ray Photoelectron Spectroscopy (XPS) (specs GmbH, Germany) (for more details, see section 2.2.3). In Figs. 4.8(a) and 4.8(b), we show the XPS spectra of a PVO film on the LSAT substrate at different sputtering times, allowing to vary the probing depths of the film. Focussing on the V^{3+} (shaded in blue) and V^{4+} (shaded in red) peaks in the spectra, we clearly observe a gradient of the V valence over the film depth, with a higher concentration of V^{4+} near the film surface. With increase in the probing depth, for example, around 10 nm from film surface, the

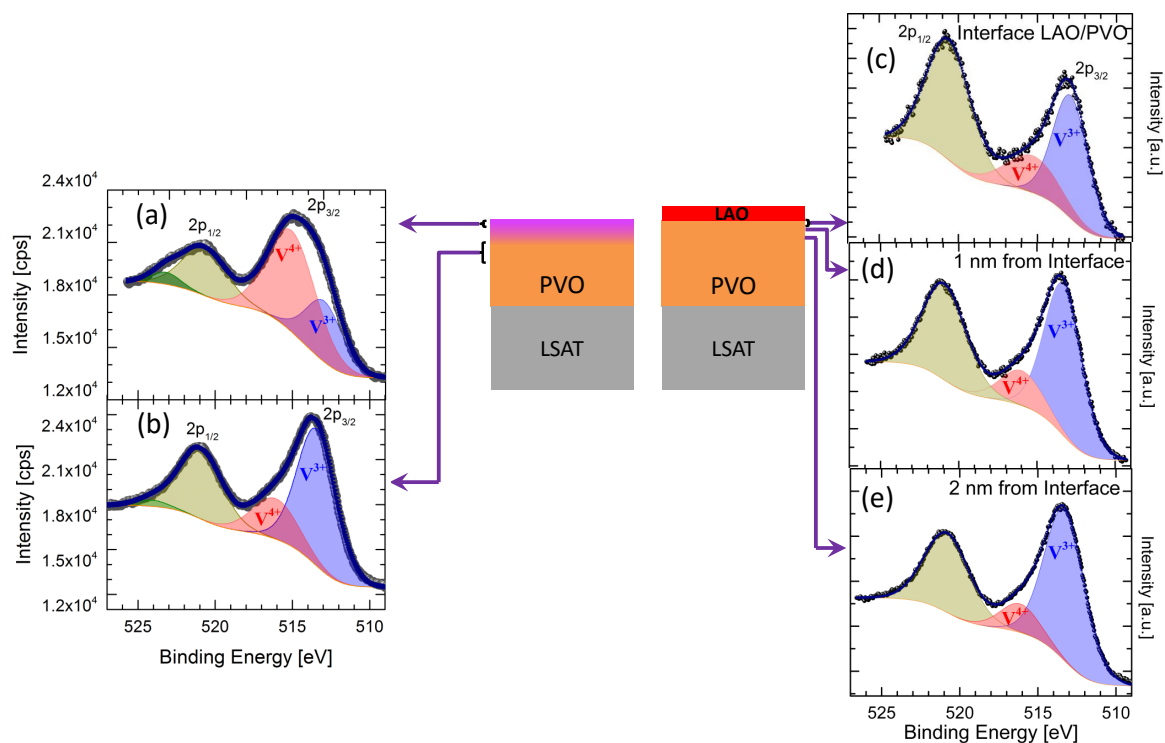


Figure 4.8: XPS spectra of V 2p core levels on a 50 nm thick PVO film on the LSAT substrate, (a) near the film surface and (b) at nearly 12 nm probing depth. The black spheres represent the original data, whereas color lines and shaded area are the fitted curves. (c-e) XPS spectra of a LAO capped PVO film. The capping layer thickness is nearly 8 nm, and PVO film thickness is kept same as before in order to compare. XPS spectra at different probing depths, (c) near LAO/PVO interface, (d) 1 nm from the interface and (e) 2 nm from the interface.

V^{3+} concentration evidently increases (see Fig. 4.8(b)).

We have then investigated the V valence states on a capped PVO film with nearly 8 nm of LAO (Figs. 4.8(c), 4.8(d), 4.8(e)). The LAO layers were in situ deposited at the same deposition conditions as that of PVO film on the substrate. One can see that capping undoubtedly increases the V^{3+} concentration at the surface of PVO film as compare to that of the uncapped / bare PVO film (Fig. 4.8(a)). Moreover, with further increase in the probing depth (from LAO/PVO interface) the V^{3+} concentration monotonically increases, and V^{4+} concentration decreases. Hence, the over-oxidized dead layer with a higher concentration of V^{4+} in a bare PVO film is certainly at the origin of the soft magnetic phase, which can be efficiently suppressed by the formation of more V^{3+} in a capped film.

Magnetization-Temperature measurements

The next step is to investigate the effect of film thickness on the magnetic transition temperature of PrVO_3 films. For this, the magnetization-temperature (*MT*) measurements were performed at $H = 50$ Oe after field cooled (Figs. 4.9 and 4.10). In order to obtain the true magnetization of the films, the substrates magnetic signals were subtracted from the whole measured sample signal (see section 2.2.6 for substrates magnetism). The magnetic phase transitions temperature of PVO thin films are obtained by plotting the derivative of the magnetization. Here, we consider the cusp in the derivative as the T_N of the films, which is clearly indicated by the dashed lines in Fig. 4.9 and Fig. 4.10. For PVO films on LAO substrates, the thick films ($t > 50$ nm) have T_N close to 100 K. While, for thinner films, the T_N has decreased to ~ 30 K ($t = 19.63$ nm), and no clear transition is observed for $t = 9.63$ nm film. For PVO films grown on LSAT substrates, the T_N is close to 90 K for all measured samples. This is probably because all PVO films (even thick film of thickness 108 nm) are epitaxially strained on LSAT substrates due to smaller mismatch, whereas, thick PVO films on LAO substrates are partially relaxed. For bulk PrVO_3 , the transition at T_N was previously ascribed to the onset of a C-type spin ordering of the vanadium moments [88, 89], for epitaxial PrVO_3 thin films, the substrate-induced strain results in a G-type spin ordered states of the vanadium moments, as evidenced by the DFT calculations (explained on

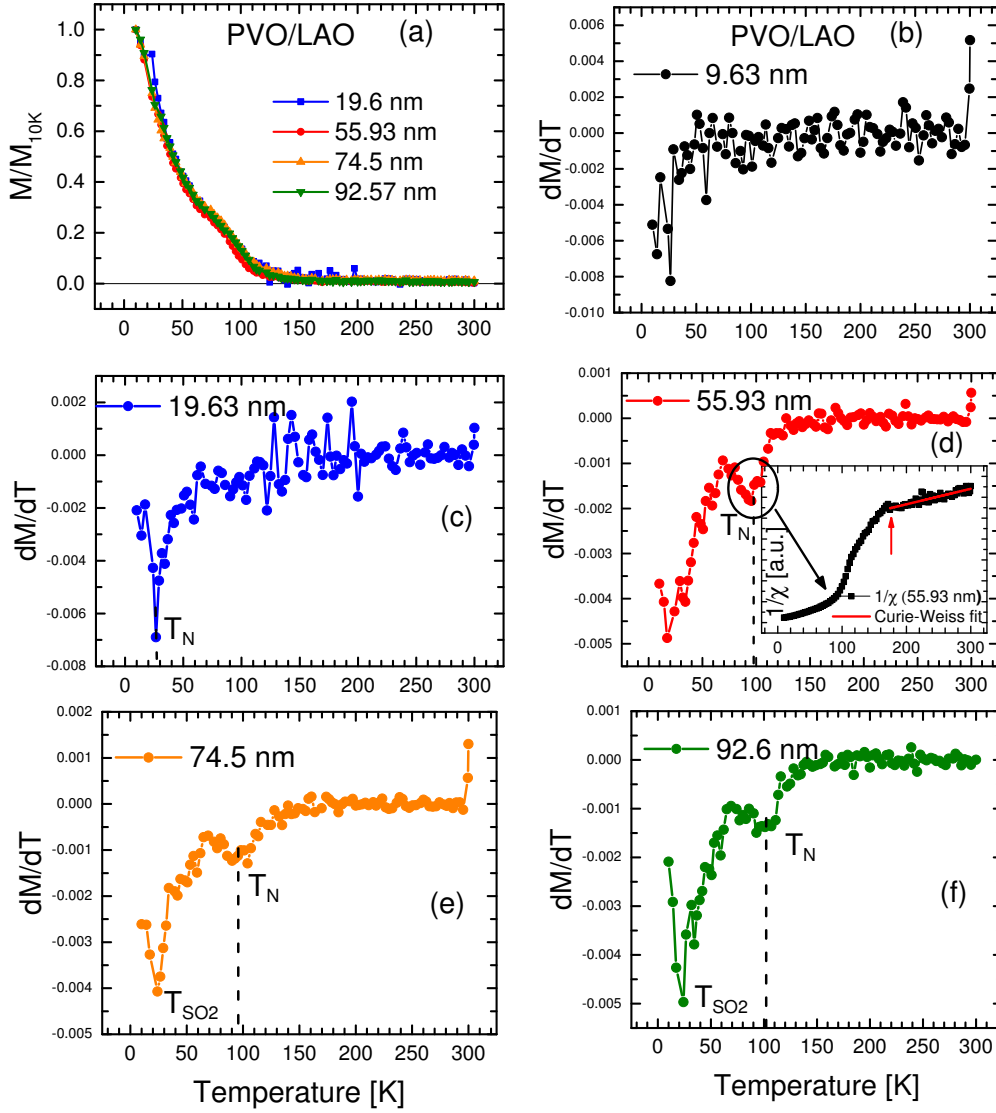


Figure 4.9: (a) Temperature dependence of the Normalized magnetization for a series of PrVO_3 films grown on LAO substrates obtained by applying in-plane magnetic field of 50 Oe. (b-f) the representative derivative of the magnetization for different film thicknesses. The T_N was estimated from the cusp, marked by the dashed lines.

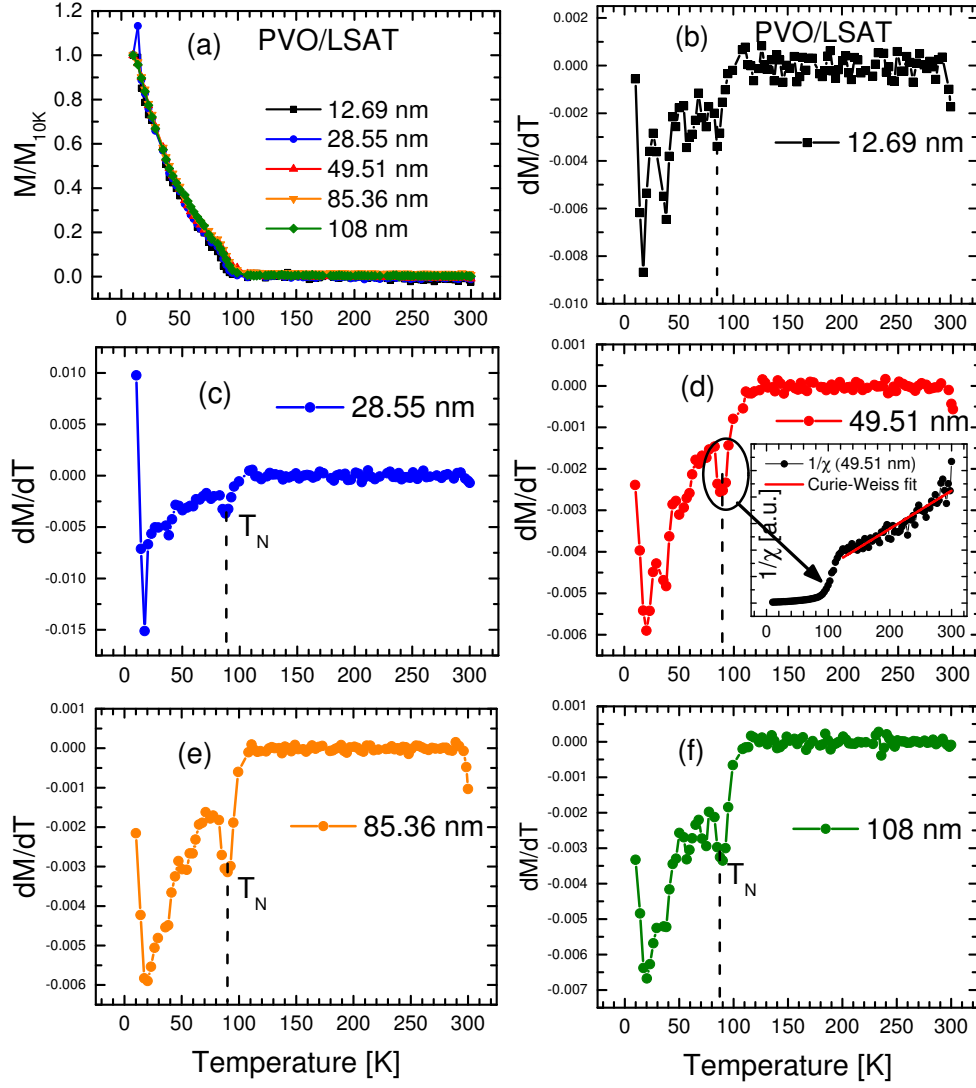


Figure 4.10: (a) Temperature dependence of the Normalized magnetization for a series of PrVO_3 films grown on LSAT substrates obtained by applying in-plane magnetic field of 50 Oe. (b-f) the representative derivative of the magnetization for different film thicknesses. The T_N was estimated from the cusp, marked by the dashed lines.

page 90, and page 36) [90]. Here, it is important to discuss the temperature dependent inverse susceptibility plot (shown in the insets of Fig. 4.9(d) and Fig. 4.10(d)), where a clear transition from the paramagnetic state is observed around 170 K for the LAO substrate (125 K for LSAT substrate). Above this temperature, the inverse susceptibility can be well fitted using the Curie-Weiss law in the paramagnetic regime (see red line), which show a typical linear dependence on temperature. However, this transition is 70 K higher than the previously assigned T_N . A possible explanation could be that, at 170 K (for LAO), there is a transition from the paramagnetic phase to an intermediate phase where spins have a combined AFM and paramagnetic order, and at 100 K (T_N) a complete AFM order of vanadium sublattices takes place. However, we have considered the cusps in the derivative curves to mark the transition temperatures in PVO thin films. In this regard, the T_N of PVO films on LAO substrates is changed by almost 70 K with the increase of film thickness. Whereas, it is nearly constant for the PVO films on the LSAT substrates. Notably, PVO films show an additional magnetic feature at T_{SO2} , established by kink in the dM/dT . This transition is surprisingly constant at ~ 20 K for both the substrates. The origins of this anomaly have also been discussed in the previous chapter. First, it might be due to the magnetic polarization of the praseodymium sublattice in the presence of exchange field produced by the vanadium moments, via Pr-V exchange, resulting in a ferrimagnetic structure [93]. Second, it could also represent a reorientation of the vanadium spin configuration from G-type to C-type, where V^{3+} spins are staggered in the *ab-plane* and aligned ferromagnetically along *c* axis.

Discussion

The influence of film thickness on the structural and magnetic properties of PrVO_3 thin films has been investigated. While, a small lattice mismatch between bulk PVO and LSAT substrate keeps PVO thin films epitaxially strained to the substrate, a partially relaxed behavior is seen for the thick films on the LAO substrates. The field dependent magnetic properties are quite interesting. Thin PVO films show a paramagnetic-like behavior with a large M_s and small H_c , whereas with increase of film thickness, the M_s decreases and H_c increases. This typical behavior has been explained by the presence of a speculated dead layer at the surface of film, which is also responsible for soft magnetic phase in M vs H. Indeed, the XPS results confirm a higher concentration of V^{4+} at the film surface, and with increase of probing depth, V^{4+} sharply decreases and concentration of V^{3+} increases. Furthermore, in order to verify that the soft component is related to the film surface, and also to revive the dead layer, the PVO film has been capped, which robustly reduces the soft component in M vs H, and the XPS results clearly show an enhancement in the concentration of V^{3+} . These results clearly demonstrate that, the dead layer at the film surface should be the origin the soft magnetic component in the M vs H.

4.2 Crystal surface orientation dependent properties of PrVO_3 films

Having explored the strain effect produced by means of utilizing various commercially available substrates and by varying film thickness in PrVO_3 thin films, we now describe the properties manifested by PrVO_3 films grown on SrTiO_3 substrates with different crystal orientations, *i.e.* STO (001), STO (110) and STO (111). Using the STO (110) and STO (111) substrates over STO (001) can have favourably significant effect on the properties of thin films. For example, cubic STO (110) substrate provide lower lattice mismatch for growing orthorhombic crystals and a chance for anisotropic strain control. Also, because of the polar nature of (110) and (111)-oriented substrates / surfaces, they are more susceptible to the reconstruction and the strain relaxation. Therefore, in this part, we present the detailed study on the crystal surface orientation dependent structural and magnetic properties of PrVO_3 films. We fabricated two series of samples on different oriented STO substrates of 35 nm and 75 nm in order to investigate the additional thickness effect on the magnetization and magnetic anisotropy. In the next sections, we discuss the results associated with $t = 35$ nm films.

4.2.1 Growth conditions

PrVO_3 thin films on STO (001), STO (110) and STO (111) were grown using pulsed laser deposition with a KrF excimer laser and a stoichiometric target. The growth temperature (T_G) and growth pressure (P_{O_2}) were kept at 650 °C and 10^{-6} mbar. The substrates were pre-treated and cleaned using ethanol and acetone only, and no further etching/heat treatment was performed. The film thickness was estimated around 35 nm and 75 nm for two series.

4.2.2 Structure

The crystal structure of the grown films is identified using a high resolution x-ray diffractometer combined with the transmission electron microscope. In the forthcoming sections, we present the HRXRD θ - 2θ scans, reciprocal space maps, phi scans to define the epitaxy of films, and the transmission electron microscopy results.

θ - 2θ and RSM scans

The *out-of-plane* lattice parameters of PVO films were extracted from XRD θ - 2θ patterns (Fig. 4.11). There is a strong film peak on the left side of the STO substrate peak near $2\theta = 22.7^\circ$ (STO (001)), 32.4° (STO (110)) and 40° (STO (111)). Two well-separated substrate peaks correspond to Cu $K\alpha_1$ and $K\alpha_2$ due to source in the X-ray tube. The oscillations can also be observed in the XRD pattern due to uniform film thickness, except for (111)-oriented STO substrate, where only one small oscillation is seen, probably due to presence of extra charges at the interface on account of the polar discontinuity and/or an intermix termination. In addition, (110)-oriented STO substrate presents these oscillations more strongly as compared to other oriented substrates, and the effect is more evident for the thicker films (Fig. 4.18). From previous studies it has been clear that the perovskite substrate surface fulfills the important criteria such as: (1) single termination; (2) no major reconstruction; (3) stable interfaces [84, 90, 97, 98]. For the classical (001)-oriented STO surface, single termination can easily be achieved by the chemical etching, and no major reconstruction is needed thanks to the chargeless layers $[(\text{SrO})^0, (\text{TiO}_2)^0]$, leading to a coherent growth of the film. For a system with (110)-orientation, criteria (3) is always met from the nominal charge point of view. Nevertheless, since the substrate is polar $[(\text{SrTiO})^{4+}, (\text{O}_2)^{4-}]$ [99], condition (1) and (2) are less straightforward. For a (111)-oriented surface, none of the criteria are trivial. First, the process of achieving single terminated STO (111) substrate is rather difficult [100, 101]. Second, even if we obtain single termination, they are always polar in nature $[(\text{SrO}_3)^{4-}, (\text{Ti})^{4+}]$, and an inadvertent surface reconstruction can prevent coherent growth of first few monolayers of the film [102].

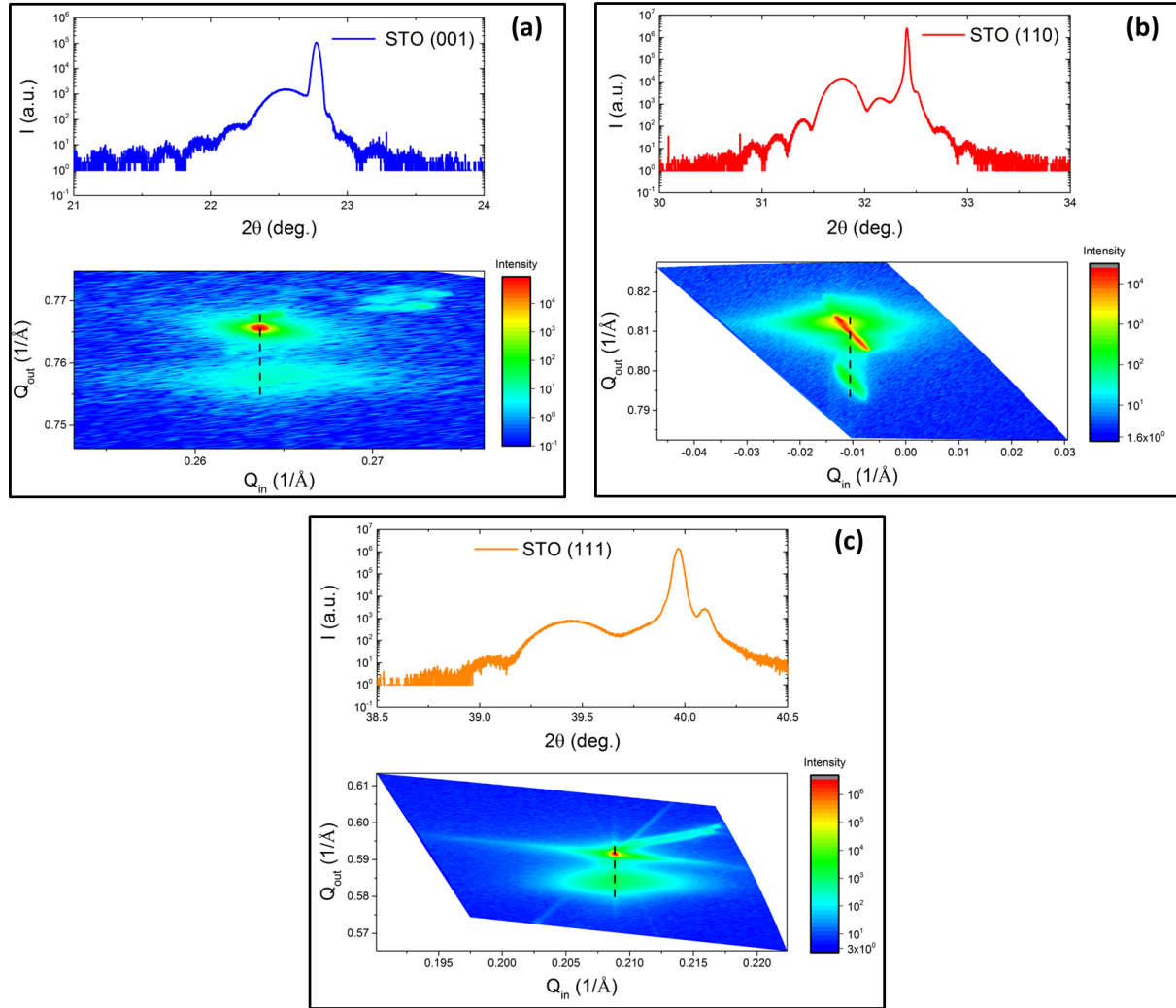


Figure 4.11: (a) HRXRD θ - 2θ scan patterns of $\text{PrVO}_3/\text{SrTiO}_3$ (001) and x-ray reciprocal space mapping around (103) plane. (b) HRXRD θ - 2θ scan patterns of $\text{PrVO}_3/\text{SrTiO}_3$ (110) and x-ray reciprocal space mapping around (130) plane. (c) HRXRD θ - 2θ scan patterns of $\text{PrVO}_3/\text{SrTiO}_3$ (111) and x-ray reciprocal space mapping around (123) plane. The reciprocal space maps show well developed PrVO_3 film peak in the lower region, and a strong substrate peak in the upper region. The lines are only guide to the eyes and indicate the strained behavior of all films.

The extracted *out-of-plane* lattice parameters for PVO/STO (001), PVO/STO (110), PVO/STO (111) are: $d_{001} = 3.940$, $d_{110} = 3.98/\sqrt{2} = 2.814$, $d_{111} = 3.954/\sqrt{3} = 2.283$, respectively. Notably, the *out-of-plane* lattice parameter of PVO/STO (110) has enhanced comparatively to other substrates, even though the change between STO (001) and STO (110) is only $\sim 1\%$. Moreover, the enhancement of *out-of-plane* lattice parameters of PrVO₃ films indicates that (1) the films have undergone an *in-plane* compressive strain, and/or (2) involve contribution of oxygen vacancies.

To explore the *in-plane* strain states and a coherent growth behavior of PrVO₃ films, reciprocal space maps in skew symmetry were collected around (103) plane for STO (001), around (130) plane for STO (110) and around (123) plane for the STO (111) substrate (lower panels in Fig. 4.11(a-c)). As the position of the film peak along the horizontal Q_{in} axis is same as that of the substrate peak for all three orientations of the substrate, we deduce that the films are grown coherently on the STO substrates, with the same *in-plane* lattice constants. By combining the HRXRD θ - 2θ and RSM data, we can therefore calculate the unit cell volume of the PrVO₃ films; $V_{pseudocubic} = 3.905^2 \times 3.940 \text{ \AA}^3 = 60.08 \text{ \AA}^3$ for PVO/STO (001), $V_{pseudocubic} = 3.905^2 \times 3.98 \text{ \AA}^3 = 60.66 \text{ \AA}^3$ for PVO/STO (110) and $V_{pseudocubic} = 3.905^2 \times 3.954 \text{ \AA}^3 = 60.29 \text{ \AA}^3$ for PVO/STO (111).

Transmission Electron Microscopy: The microstructure of PrVO_3 films grown on (001)-, (110)- and (111)-oriented STO substrates

In order to get further insights into the local microstructure of the films, the transmission electron microscopy was performed. For this, the cross-section was prepared by Maxime Hallot at université de Lille, and the microscopy study was performed at CRISMAT laboratory by Dr. Philippe Boullay. Fig. 4.12 shows the images of the observed film ((a) and (d)), the associated diffraction pattern (encircled in red and green), and the representative schematic of the crystallographic growth orientation ((b), (c) for STO (111), and (e) for STO (110)). Two kinds of PVO domains are observed for the films grown on (111) STO, oriented 60° to each other. This is consistent with the six fold symmetry presented by the (111)-oriented STO. From the associated diffraction pattern in Fig. 4.12, the following epitaxial relationships between the film (F) and the substrate (S) are established: (1) $F[011]_o // S[111]_c$ and $F[100]_o // S[110]_c$, or $F[101]_o // S[111]_c$ and $F[010]_o // S[110]_c$, (2) $F[311]_o // S[111]_c$ and $F[\bar{1}\bar{1}2]_o // S[110]_c$.

The PVO film grown on top of a (110)-oriented STO presents a smooth and parallel interface as compared to the interface between the film and (111) STO, in agreement with the previous observation through x-ray diffraction. This is most probably because of the absence of the polar discontinuity in case of (110)-oriented STO substrate. Furthermore, the TEM results confirm the thickness of the film, around 35 nm. The simulation of the diffraction pattern extracted from several local regions indicates two kinds of domains, oriented 180° with each other (Fig. 4.12(e)). Another domain can be conceived simply by rotating the orthorhombic lattice by 180° . Thus, the film grows with $[100]_o$ (or $[010]_o$) as out-of-plane while clamping $[001]_o$ and $[010]_o$ (or $[100]_o$) to the substrate, with the following epitaxial relationships: $F[100]_o$ (or $F[010]_o$) $// S[110]_c$ and $F[001]_o // S[001]_c$. Even if no quantitative information is really accessible because of the local nature of the transmission electron microscopy, an average structural analysis can be obtained using the complementary XRD, such as phi scan described in the next section.

For PVO film grown on (001) STO, O. Copie et. al. already observed two PVO domains oriented 90° to each other [84], with the epitaxial relations: $F[110]_o // S[001]_c$ and $F[001]_o // S[100]_c$, or, $F[110]_o // S[001]_c$ and $F[001]_o // S[010]_c$. The schematic representation of the oriented do-

main is show in Table 4.1 (also in Fig. 1.11). The calculated in-plane lattice mismatch and the observed growth of film for different orientation of STO substrate is given in Table 4.1.

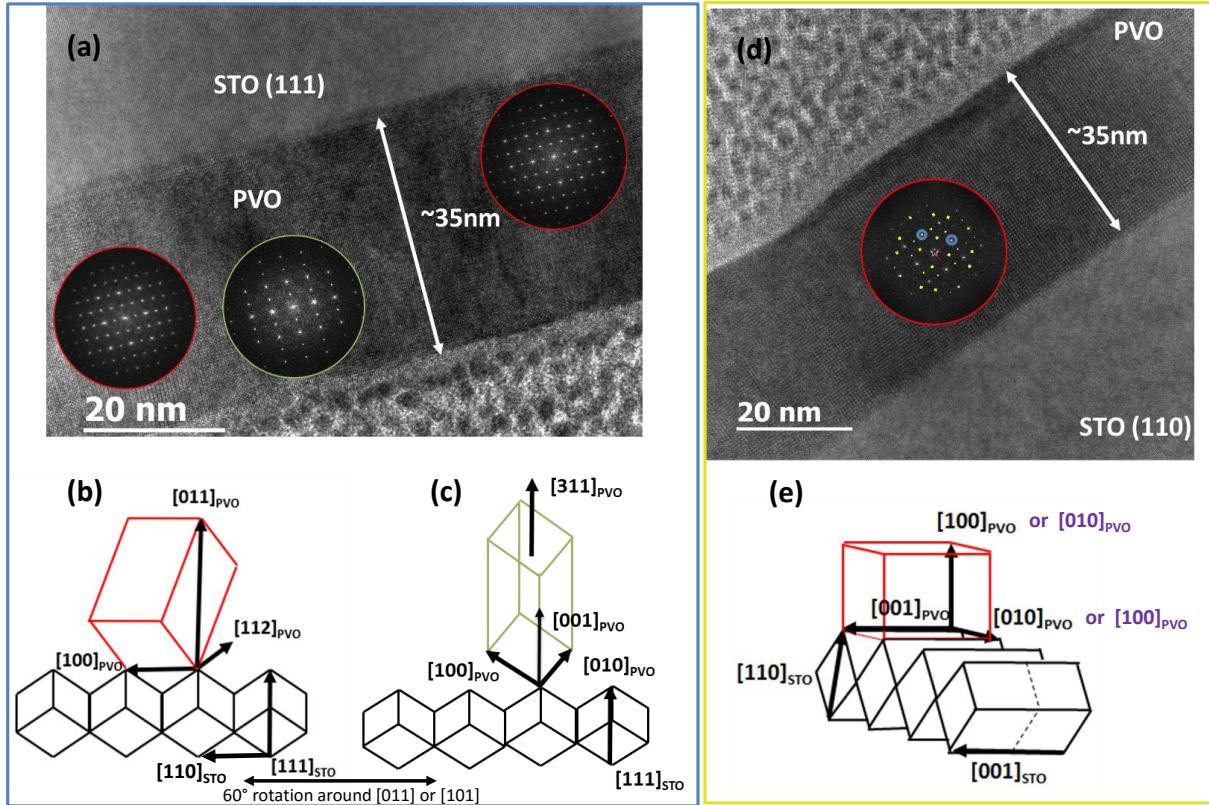


Figure 4.12: TEM image of PVO film on STO (111) (a) and STO (110) (d) and associated diffraction pattern. Schematic representation of PVO domains observed for various substrates (b, c, e).

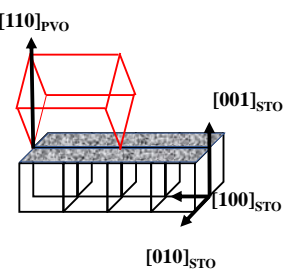
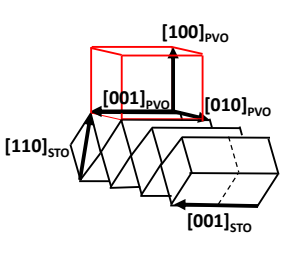
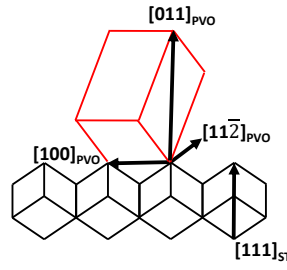
	STO[001]			STO [110]			STO [111]		
	In-plane		Out-of-plane	In-plane		Out-of-plane	In-plane		Out-of-plane
Directions	$[001]_o = [100]_{pc}$	$[\bar{1}\bar{1}0]_o = [010]_{pc}$	$[110]_o = [001]_{pc}$	$[001]_o = [001]_{pc}$	$[010]_o/[100]_o = [110]_{pc}$	$[100]_o/[010]_o = [110]_{pc}$	$[11\bar{2}]_o = [110]_{pc}$	$[100]_o/[010]_o = [110]_{pc}$	$[\bar{1}01]_o/[\bar{0}1\bar{1}]_o = [111]_{pc}$
Lattice mismatch	0.41 %	-0.05 %		0.41 %	-0.74 % / 0.65 %		0.18 %	0.65 % / -0.74 %	
Growth									

Table 4.1: A detailed summary of the *in-plane* and *out-of-plane* lattice directions of PVO on STO with different crystal surface orientation. The lattice misfit are calculated for *in-plane* directions. The experimentally observed growth orientations of the PVO lattice on different oriented STO are also shown. The in-plane lattice mismatch between PVO and STO is defined as: $\sigma_{[hkl]} = (a_{STO} - a_{PVO})/a_{PVO}$, where a_{STO} and a_{PVO} are the lattice parameters of cubic STO substrate and PVO respectively, in the direction $[hkl]_o$ of orthorhombic PVO.

Phi-scans

To determine the metric of the PrVO_3 film with respect to the substrate, the phi scans of a skew symmetric plane were collected. Fig. 4.13 shows the ϕ scans for (101), (200) and (200) asymmetric crystal planes of (001) (110) and (111) oriented STO respectively. The observation of four reflections apart 90° in the phi scan for (101) reflection of (001) oriented STO indicate the four fold symmetry of the substrate. In addition, the occurrence of film peaks at the same phi angle (as that of substrate) further reflects that the film is grown epitaxially on the substrate with the so called *cube-on-cube* epitaxy. (Here, the pseudocubic description of film has been used).

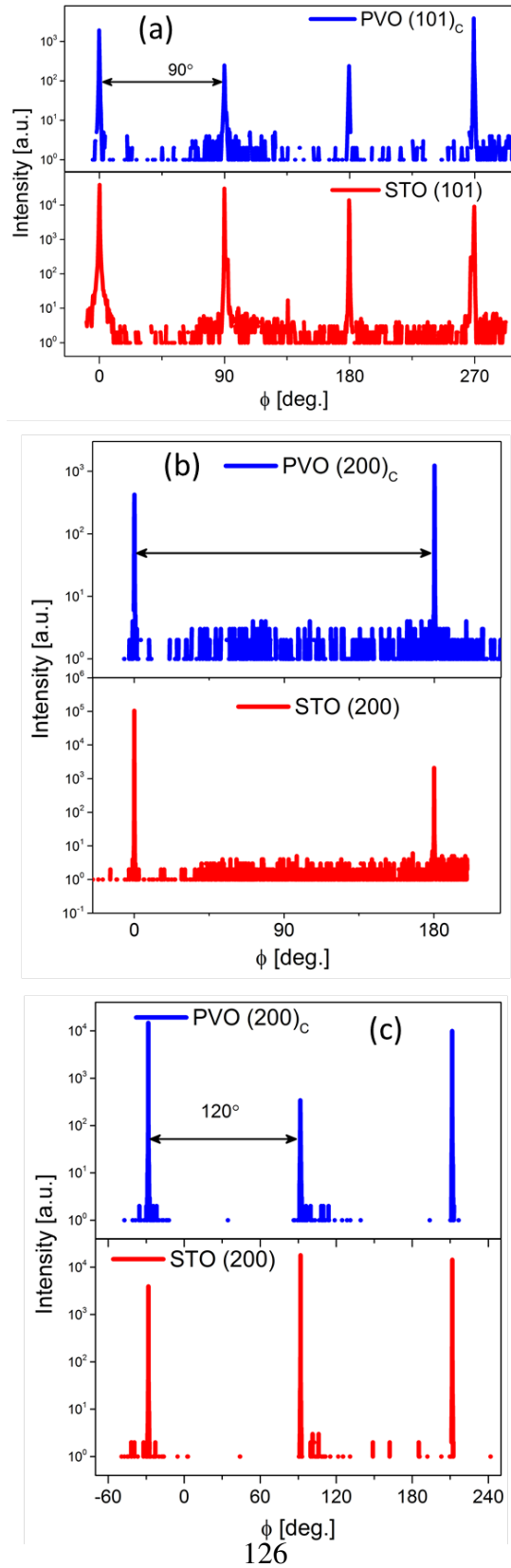


Figure 4.13: Phi scans measured along (101) reflection of STO (001) (a), (200) reflection of STO (110) (b), and also along (200) reflection of STO (111) (c). Here the pseudocubic description is used for film.

Similarly, for (110) and (111) STO, the two fold and three fold symmetry of the substrates are observed respectively, and the films exhibit a cube-on-cube epitaxy in that the ϕ angle is same for film and the substrate.

4.2.3 Strain controlled epitaxial stabilization

The stabilization of the epitaxial phases in thin films is an important issue for building advanced material devices. The phase stability in thin films is established by the kinetic processes and the thermodynamical stability of the adsorbed atoms [103]. In this section, we examine the effect of the lattice misfit induced strain in PVO thin films on the surface diffusion of the adsorbed atoms. Several groups have studied the epitaxial stabilization phenomenon on the oxides, and concluded a quadratic relationship between the activation energy and the strain [104, 105, 106]. A linear dependence of the activation energy versus strain has also been observed for semiconductors

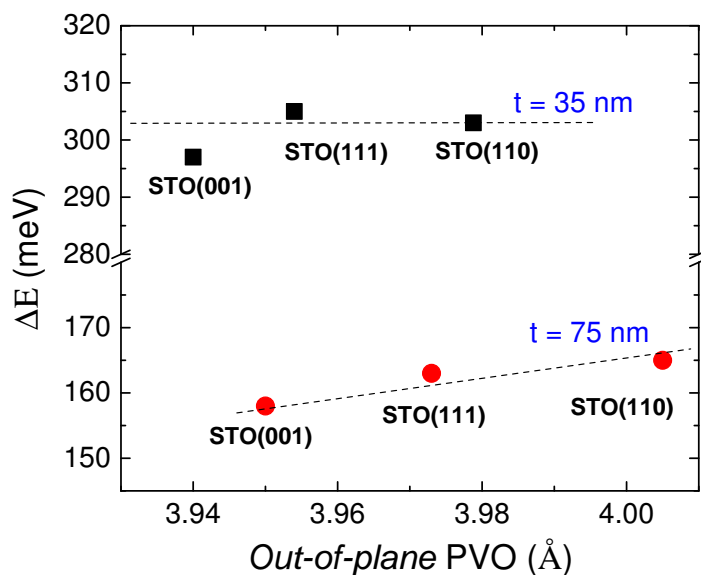


Figure 4.14: Strain dependence of the activation energy of the surface atoms, presented for films grown on STO of different crystal surface orientation and for two film thicknesses.

[107, 108]. For PVO films grown on the STO substrates of different crystal surface orientations, the extracted strains along *out-of-plane* are: $\sim 1.0\%$ [STO(001)], $\sim 1.36\%$ [STO(111)] and $\sim 2.02\%$ [STO(110)]. Using the Arrhenius equation, $\tau = \tau_0 \exp(\Delta E / K_B T)$ where τ is the relaxation time, we can calculate the activation energy ΔE . The relaxation time (τ) is defined as $1/e$ times the time taken to complete half unit cell of PVO. As the *out-of-plane* lattice parameters of PVO films on different oriented substrates are different, thus the time required to make one unit cell would also be different. Accordingly, we calculated the activation energy for PVO films under different strain levels induced by the oriented substrates. The activation energy associated with the thicker films ($t \sim 75$ nm) is also presented for comparison. From Fig. 4.14, two conclusions can be drawn: First, it costs larger activation energy to stabilize the surface atoms in thinner films as compared to the thick films. This is presumably because of different strain states between thick and thin films, and indeed it is conceivable that for the thick films which are partially relaxed (discussed in the next section) the energy barrier for the surface atoms is lower than those for the strained thin films. Furthermore, the activation energy for thicker films is nearly same as that of the bulk PVO (~ 180 meV, see section 3.4). Second, for any film thickness-series, the film with the highest *out-of-plane* / strain possesses the highest activation energy, although the change is very subtle.

4.2.4 Magnetic properties

In this section, we will discuss the magnetic properties of the different oriented PrVO_3 films and demonstrate that these aforementioned properties strongly depend on the orientations of lattice distortion imposed by (001)-, (110)-, and (111)-oriented SrTiO_3 substrates. The magnetic properties of PVO thin films were investigated using commercial SQUID (5T), combined with VSM-SQUID (7T). The substrates magnetic signals were subtracted from the samples raw magnetic signals in order to obtain the net magnetization of the PVO films (see section 2.2.6 for substrates magnetism). From the raw magnetic signals of the substrates, it was seen that the STO substrates with three different orientations of out-of-plane are diamagnetic, and have nearly

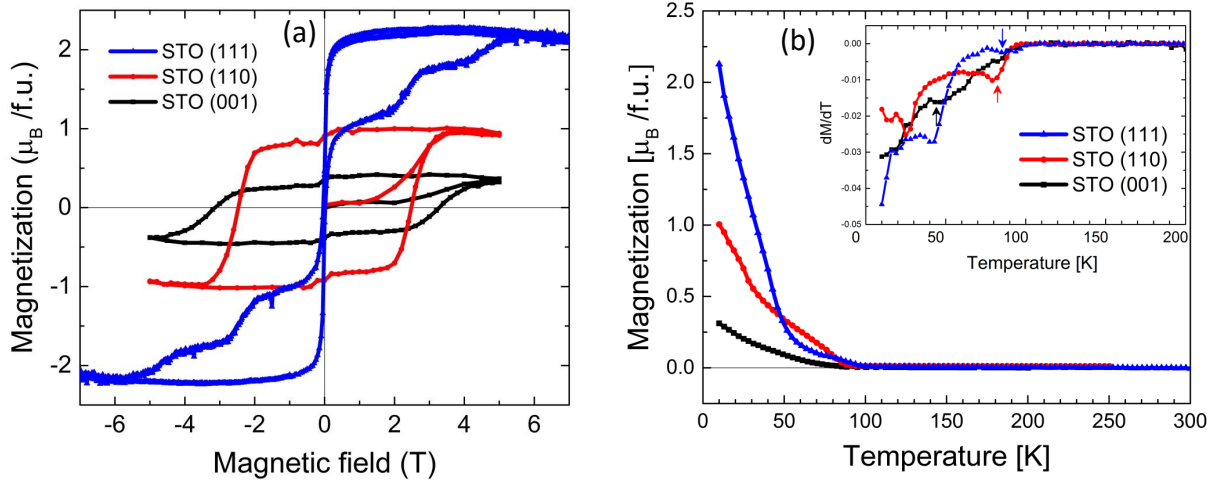


Figure 4.15: (a) Hysteresis cycles obtained at 10 K for PVO films on different oriented STO substrates. (b) Field-cooled scans as a function of temperature, performed by applying 50 Oe field in the plane of the sample, and the inset shows the derivatives of magnetization as a function of temperature, and the arrows depict the transition temperature.

equal magnetic susceptibilities. Fig. 4.15 shows the main magnetic results of PVO films grown on different oriented STO substrates. For PVO film on the (001)-oriented STO, the saturation magnetization is $\sim 0.3 \mu_B / \text{f.u.}$, and the coercive field $\sim 3\text{T}$, which are close to what was previously observed in chapter 3 for a 50 nm PVO/STO film. Remarkably, the magnetic behavior of PVO films on (110)- and (111)-oriented STO substrates are different from the film on (001)-oriented STO. By considering the hard components, the saturated magnetization of PVO films on (110)- and (111)-oriented STO has increased and is close to $0.8 \mu_B / \text{f.u.}$, and $1.2 \mu_B / \text{f.u.}$, respectively. To the best of our knowledge this phenomenon where the saturation magnetization is enhanced by approximately 4 times merely by changing the crystal surface orientation of the substrate, is observed first time in thin films. A similar study focussed on SrRuO_3 thin films on different oriented STO substrates reported nearly 2 times enhancement of saturation magnetization (between (001) and (111)), and the authors explained this peculiar behavior using a high spin state of Ru^{4+} ions [109].

Interestingly, small jumps in the hysteresis loops (Fig. 4.15(a)) can also be observed, and probably associated with the presence of magnetic domains. We showed earlier (section 4.1.3) that the appearance of soft magnetic component in the hysteresis loop is a result of the presence of dead-layer at the film surface. Following this, we speculate the existence of two magnetic domains in PVO film on (111)-oriented STO, with different coercive fields. The two jumps correspond to the two crystallographic domains observed through TEM (see Fig. 4.12). Similarly for the (001)- and (110)-oriented STO, the soft component is attributed to the dead layer, whereas the hard component corresponds to the crystal domain. Another important point is the intensity of the soft component of the PVO film grown on STO (111) which is higher than measured before for all the other films. One hypothesis is the polar nature of the substrate-film for this orientation [102]. This can arise from the polar surface of the sample, which is not stable and has tendency to oxidize.

Remarkably, a staircaselike behavior in hysteresis loop (below 3 K) was also reported by Tung et. al. [110] for PrVO_3 single crystals, and found to depend on the magnetic field sweep rate, in that the steps in MH loop shifts to higher magnetic field as the field sweep rate is reduced. This unusual behavior was then proposed to be arisen on account of two phases in PrVO_3 single crystals, one with fraction of spins responsible for the glassylike behavior, and other spins ordered in the antiferromagnetic fashion. Nevertheless, this proposed behavior of PrVO_3 : *a disordered antiferromagnet with Random Fields*, still remains unconvinced due to lack of solid proofs such as neutron scattering experiments or theoretical calculations. Besides, our observations of PVO thin films are in contrast with the results of counterpart single crystal. From Fig. 4.16(b), it is evident that the steps in $M-H$ loops do not essentially depend upon the field sweep rate, meaning that the steps are not associated with the random fields or spin-glass mechanism. Moreover, the AC magnetization measurements at different frequencies were also performed to further verify the possibility of spin glass behavior of the PVO films (Fig. 4.16(a)). In the Fig. 4.16(a), the temperature dependent magnetic moment of PVO film on (111)-oriented STO substrate is shown at different frequencies, which clearly display the magnetic ordering / transition temperature around 83 K. However, the results do not reveal any change in the transition temperature with increase of frequency, ruling out the spin-glass mechanism in PVO films.

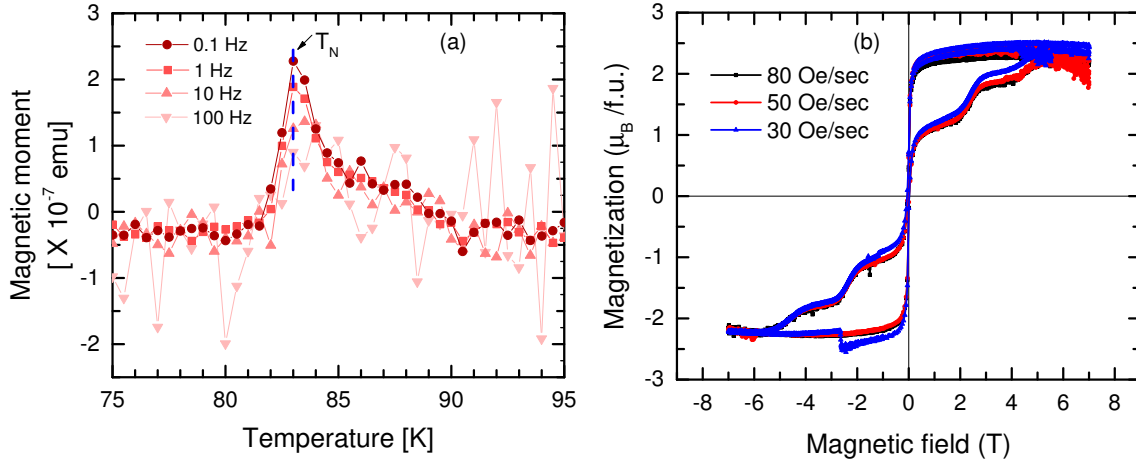


Figure 4.16: (a) AC moment as a function of temperature (in the vicinity of magnetic ordering temperature T_N) at different frequencies. The blue dashed line shows a constant behavior of T_N for all frequencies. (b) Hysteresis loops of PVO film on (111)-oriented STO substrate collected at different field sweep rates.

Fig. 4.15(b) shows the temperature dependence of field cooled magnetization at in-plane applied field of 50 Oe. The transition from a paramagnetic state to an ordered antiferromagnetic state of the vanadium sublattices is realized through the minimum in the slope of magnetization, marked by the arrows in the inset of Fig. 4.15(b), and referred to as the Néel temperature (T_N). For PVO film on the (001)-oriented STO substrate, the T_N is close to 40 K, whereas, it has increased to ~ 80 K for the film on the (110)- and (111)-oriented STO substrates, in sharp agreement with the AC susceptibility measurements (Fig. 4.16(a)). The strain along out-of-plane of film on (001)-, (110)- and (111)-oriented STO substrates are $\sim 1.0\%$, $\sim 2.0\%$ and $\sim 1.4\%$, respectively. For the (110)- and (111)-oriented STO, a large tensile strain along out-of-plane direction reduces the in-plane V-V nearest neighbour distance, and thus increase the exchange interactions, and hence enhanced T_N .

We have further investigated the magnetic anisotropy of epitaxial PVO thin films grown on STO substrates with different orientations. The magnetic anisotropy of the oriented PVO films is characterized by $M - H$ after subtraction of the diamagnetic contribution from the STO sub-

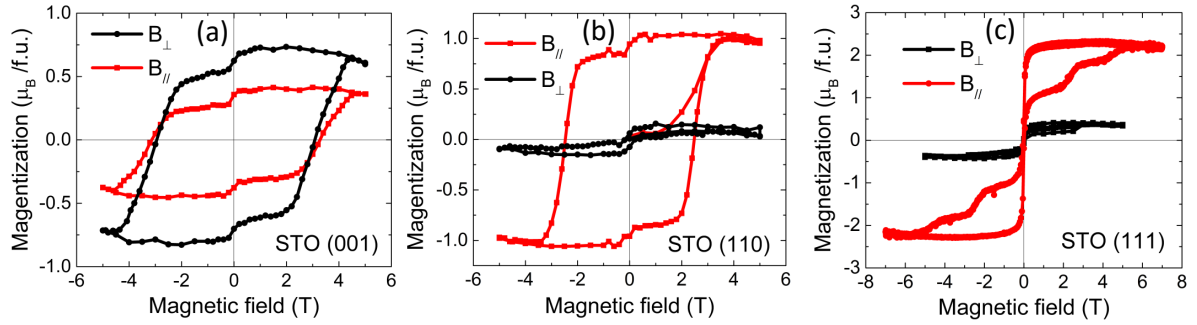


Figure 4.17: Hysteresis loops at $T = 10$ K of PVO films on STO (001) (a), STO (110) (b) and STO (111) (c) substrates for field applied along in-plane and out-of-plane directions of the substrates.

strate. In order to ensure the identical magnetic susceptibility for (110)- and (111)-oriented STO substrates for both field directions, we have collected the $M - H$ cycles for magnetic field applied along in-plane and out-of-plane of the substrates (see Figs. 2.19 and 2.20, page 70). Figs. 4.17(a-c) show the $M - H$ for PVO films on the oriented substrates, for magnetic field applied along parallel and perpendicular to the sample plane. For the PVO films on (110)- and (111)-oriented STO substrates, a strong anisotropy is observed, where, the largest saturated magnetization is achieved when field is applied along in-plane of the sample. Whereas, for the PVO film on (001)-oriented STO substrate, the largest saturated magnetization is achieved probably when magnetic field is applied along out-of-plane direction, with almost similar coercivity for the two directions. This is in contrast to our previously observed M versus H loops for the PVO film on (001)-oriented STO (see Fig. 1.12, chapter 1). However, the film shown in Fig. 1.12 was grown at a different deposition conditions, *i.e.* at 10^{-5} mbar and 600°C . In this sense, an anisotropy with higher saturated magnetization appears for the (001)-oriented STO compare to magnetic field direction parallel to the substrate plane, while, very high anisotropy is observed for PVO films grown on (110)- and (111)-oriented STO substrates. To summarize, the values of the coercive field, remanent magnetization, and saturation magnetization for field parallel and perpendicular are listed in Table 4.2.

Table 4.2: Crystallographic orientation and angular dependence of coercive field H_c , remanent magnetization M_r , and the saturation magnetization M_s for 35 nm PVO films. Here, θ (angle between direction of magnetic field and sample surface) = 0° means field is applied *in-plane*, and $\theta = 90^\circ$ means field is orthogonal to sample surface.

Orientation		0° / <i>in-plane</i>	90° / <i>out-of-plane</i>
001	H_c (T)	3.1	3.0
	M_r (μ_B / f.u.)	0.35	0.66
	M_s (μ_B / f.u.)	0.42	0.75
	axis		
110	H_c (T)	2.4	0.2
	M_r (μ_B / f.u.)	0.9	0.06
	M_s (μ_B / f.u.)	1.0	0.15
	axis	Easy	Hard
111	H_c (T)	0.03	0.03
	M_r (μ_B / f.u.)	0.47	0.03
	M_s (μ_B / f.u.)	2.3	0.4
	axis	Easy	Hard

As we have seen previously that the film thickness can be used to observe the strain relaxation effects, thus influencing their magnetic properties. Therefore, in order to investigate the relaxation effect on the uniaxial/biaxial magnetic anisotropy in PVO films, we fabricated thicker films of $t \sim 75$ nm, and characterized them using XRD and SQUID magnetometry.

The representative HRXRD $2\theta - \omega$ scans of 75 nm PVO films grown on differently oriented STO substrates are shown in Fig. 4.18. The films are grown single-phased, evidenced via wide range $2\theta - \omega$ scan (not shown), and present thickness fringes on (001)- and (110)-oriented sub-

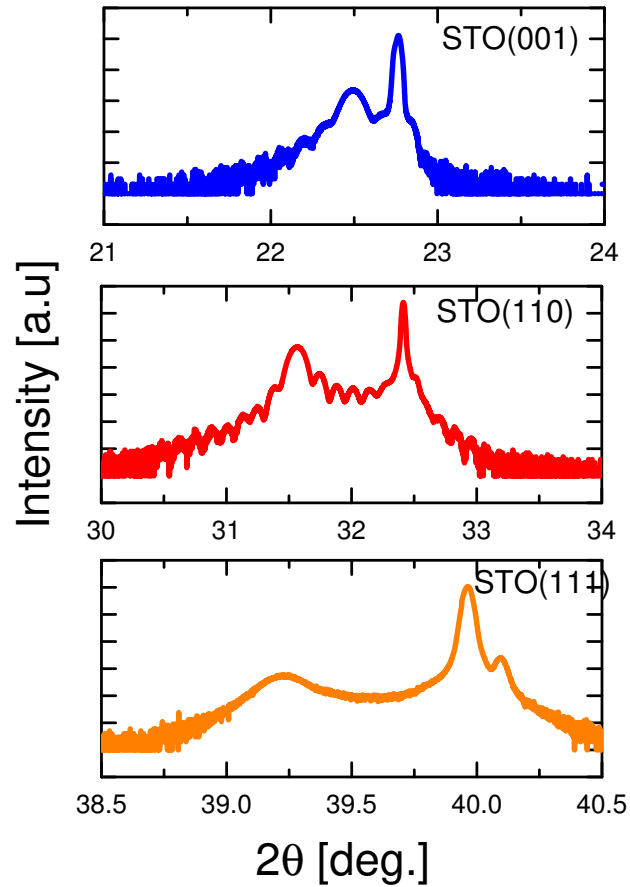


Figure 4.18: HRXRD $2\theta - \omega$ scans of 75 nm PVO films grown on (001)-, (110)- and (111)-oriented STO substrates, in the vicinity of cubic (001), (110) and (111) reflections, respectively.

strates, while these are absent for the (111)-oriented substrate, possibly due to mix termination, and/or presence of extra interfacial charges. Figs. 4.19(a-c) show the collected reciprocal space maps of 75 nm PVO films on (a) (001)-, (b) (110)-, and (c) (111)-oriented STO substrates, around skew-symmetrical planes of the substrates. The inspection of these plots reveals that all the oriented PVO films are partially relaxed, as evidenced by the deviated Q_{in} value of film from that of the substrate. Interestingly, the shift of film reflection to the higher values of Q_{in} indicates a lowering of in-plane lattice constant of film to the bulk value *i.e* 3.901 Å. Albeit a small lattice misfit between PVO and STO substrate the film appears to be partially relaxed, and might be account for the increased number of defects with time (laser shot), giving rise to enhanced out-of-plane lattice constants of PVO: 3.95 Å(STO (001)), 4.00 Å(STO (110)), and 3.97 Å(STO (111)).

Figs. 4.19(d-f) show the hysteresis loops along two in-plane and out-of-plane directions of (001)-, (110)-, and (111)-oriented STO substrates. For (001)-oriented STO, the easy axis most probably lies along [001] of STO substrate, while the hysteresis loops corresponding to the two in-plane direction *i.e* [100] and [010], exhibits a square-like loop with nearly half saturation magnetization as compared to magnetization along the easy axis, and can be defined as a hard or an intermediate axis. To obtain a conclusive information on the anisotropy, the angle dependence of magnetization would be required. Remarkably, the saturation magnetization, remanence and the shape of hysteresis loops along both in-plane directions of STO(001) are similar, indicating isotropic magnetism probably due to dominance of four fold crystalline anisotropy in the PVO film on (001)-oriented STO substrate. For (110)-oriented STO substrate, we observe an evident easy axis along [001] of STO, while the hard axis lies out-of-plane along [110], evidenced by a linear $M - H$ loop (inset of Fig. 4.19(e)). Therefore, there is a clear perpendicular anisotropy for PVO film on (110)-oriented STO. More interestingly, the hysteresis loops corresponding to two in-plane directions of film separated by 90° differ extensively. This clearly shows a presence of uniaxial anisotropy for PVO film on (110)-oriented STO, and can be account for the magnetoelastic anisotropy present in the film due to different strain along two in-plane directions. In this sense, two significant observations can be drawn for PVO film on STO (110): (1) Single domain film, or, two domains but oriented 180° to each other. This is because it is practically

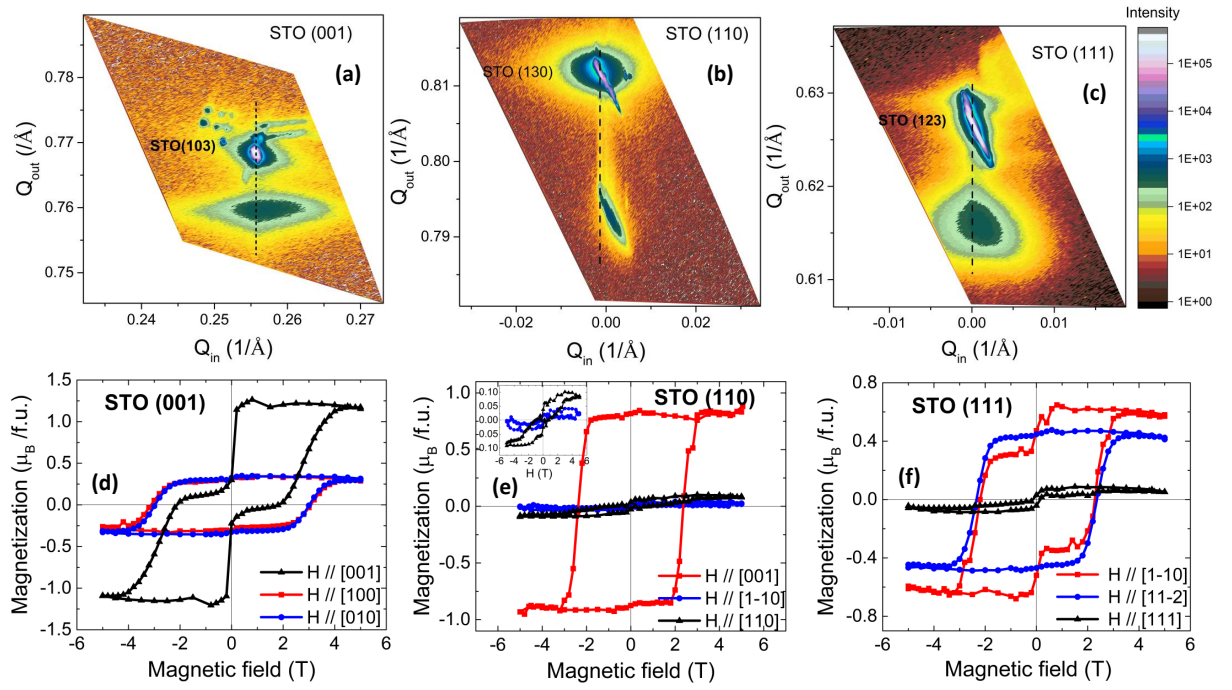


Figure 4.19: X-ray reciprocal space mapping around asymmetrical (103), (130), and (123) plane of STO (001) (a), STO (110) (b), and STO (111) (c), respectively. Magnetic anisotropy measurements of PVO films on STO (001) (c), STO (110) (d), and STO (111) (e) substrates. The magnetic field directions refer to the direction of the substrates.

not possible for $[001]_o$ PVO direction to align along $[1-10]$ of STO due to enormous mismatch between the two directions (see Table 4.1). (2) The significant difference in M vs H along two in-plane directions is itself a key proof that the strain along two in-plane directions is not of the same sign. Thus, as the $[001]_o$ PVO is already under tensile strain (see Table 4.1) and is the direction of easy axis, the other in-plane crystal direction of PVO has to be under a small tensile or a compressive strain. As a result, the two in-plane $[001]_o$ and $[010]_o$ crystal directions under tensile and compressive strain, respectively, should explain the experimentally observed uniaxial anisotropy along $[001]_o$, due to magnetoelastic and magnetocrystalline anisotropy. Finally, for (111)-oriented STO, the easy axis of magnetization is along any of the in-plane directions of STO substrate and the hard axis remains along $[111]$ direction. The remanence of two in-plane directions is almost same, although saturation magnetization remains higher along $[1-10]$ direction. Also, given the six fold symmetry of STO (111), the easy axis could lie along any of the in-plane axis besides $[1-10]$ and $[11-2]$ which stabilizes the energy balance between magnetocrystalline energy, and both magnetostatic and magnetostriction energy.

Finally, by comparing the saturation magnetization values for $t = 35$ nm, and 75 nm (Fig. 4.15 and Fig. 4.19), we observe that the M_s has decreased significantly for the (110)- and (111)-oriented STO substrates with increase in film thickness, whereas, change in M_s value is small for (001)-oriented STO between two thicknesses. Thus, the magnetic properties of PVO films on (110)- and (111)-oriented STO substrates are much sensitive to the film relaxation, as compared to (001)-oriented STO. In addition, the shape, and/or number of jumps in the hysteresis cycles are changed between $t = 35$ nm and 75 nm, specially for (111)-oriented STO. This could be due to partially relaxed behavior of latter $t = 75$ nm films, which could have crystallographic and magnetic domains different from those of former $t = 35$ nm films.

Generally, a compressive strain enhances the out-of-plane magnetization, while a tensile strain increases the in-plane magnetization [111, 112, 113]. The resulting deformation of oxygen octahedra surrounding V, being elongated (compressed) along out-of-plane direction for a compressive (tensile) strain, could be the cause of the anisotropy. Moreover, for PVO films grown on the (110)- and (111)-oriented STO substrates, the in-plane strains are unequal in two in-plane orthogonal directions (Table 4.1), giving rise to a further in-plane deformation of the octahedra,

and thus causing an in-plane uniaxial anisotropy.

Discussion

In this part of the chapter, we studied the structural, microstructural and magnetic properties of PrVO_3 (PVO) thin films grown on the SrTiO_3 (STO) substrates with different crystal orientations. A cube-on-cube epitaxy of PVO films is seen on all kinds of orientations of the substrate. The local microstructural study reveals a single domain growth along $[100]_o$ / $[010]_o$ of PVO on STO (110), while two domains oriented 60° to each other are seen on STO (111) substrate. The different oriented substrates impose different strains in PVO films, as seen by using XRD, and thus have direct influence on the magnetic properties thereof. A surprising enhancement of saturation magnetization is seen in 35 nm PVO film on (111)-oriented STO substrate. The in-plane and out-of-plane magnetic anisotropy for two film thicknesses, 35 nm and 75 nm, is also investigated. While the easy axis of magnetization for PVO films grown on (001)-oriented STO is found to be along out-of-plane direction, it lies along in-plane direction of the film for (110)-, and (111)-oriented STO substrates. The thick film on (001)-oriented STO exhibits in-plane magnetic isotropy. Thick PVO film on (110)-oriented STO show a strong uniaxial in-plane anisotropy with easy axis along $[001]$ of STO, while film on (111)-oriented STO show a weak uniaxial anisotropy. Therefore, controlling the orientation of film out-of-plane using different oriented substrates is a very efficient technique to tune the anisotropy of the magnetic materials.

Chapter 5

CONCLUSIONS AND OUTLOOK

This thesis work focussed on the study of PrVO_3 opens a route to unveil hidden novel phases in thin films by using the versatile strain engineering technique. The thesis is segmented into three different parts, where the strain engineering is realized through different means of imparting the epitaxial strain in PVO thin films.

In first of the manuscript, various single crystal substrates of different lattice parameters are used to introduce a range of strain levels in PrVO_3 thin films. The film has the highest level of strain on the LaAlO_3 (LAO) substrate, around 2.4 %, whereas the lowest on the SrTiO_3 (STO) substrate, around 0.5 %. This strain is accommodated via a change in the lattice constants of PVO, distortion of octahedra through tilting or rotation as evidenced by the DFT, and even through creation of oxygen vacancies. The calculations based on the lattice mismatch and the Poisson ratio show an expansion of PVO unit cell when grown on the STO substrate, in contrast to the compression of unit cell volume for the other substrates. This has been explained by the presence of oxygen vacancies in PVO film grown under tensile strain, in agreement with other studies [58, 59]. The different levels of strains in the films directly affect their physical properties. Tuning of the strain from 0.5 % to 2.4 % in PVO films leads to change in T_N by ~ 70 K. In addition, the PVO films exhibit new magnetic features at low temperatures which are absent from the parent bulk compound. The DFT calculations are also performed in order to validate the experimental

observed trend of T_N versus strain in PVO films. They do not only confirm the experiments, but also predict a change of the electronic structure of PVO with the change of strain. For the low mismatched substrates *i.e.* STO and LSAT, a large Jahn-Teller distortion is extracted, while for large mismatched substrates *i.e.* LAO and YAO, a change in the V-O-V bond angle is more favourable. More important is the remarkable difference in the T_N of films on STO and LAO substrates, which clearly indicates that a compressive strain in PVO films favors the super-exchange interactions.

In the second part of manuscript, the strain engineering in PVO films is further investigated by varying film thickness in range of 10 – 100 nm. On one hand, PVO films on the LAO substrates show a relaxation effect with increase of film thickness, due to large mismatch between PVO and the LAO substrate. On second hand, PVO films on the LSAT substrates are strained, even at a film thickness of ~ 110 nm, most probably due to small lattice mismatch imparted by the LSAT substrate. Moreover, the PVO films display very intriguing magnetic properties as a function of film thickness. Thin PVO films show a paramagnetic-like behavior with a large M_s and small H_c , whereas with increase of film thickness, the M_s decreases and H_c increases. This behavior is explained by the presence of a dead layer at the surface of film, which is also responsible for soft magnetic phase in M vs H. The XPS results indeed confirm a higher concentration of V^{4+} at the film surface, and with increase of probing depth, V^{4+} sharply decreases and concentration of V^{3+} increases. Furthermore, in order to verify that the soft component is related to the film surface, and also to revive the dead layer, the PVO film has been capped, which robustly reduces the soft component in M vs H, and the XPS results clearly show an enhancement in the concentration of V^{3+} . In a nutshell, the thinner films possess a larger soft magnetic phase (paramagnetic) with large saturated magnetization, and with increase in film thickness, the fraction of film that is made of paramagnetic phase reduces and the relative contribution of PVO increases.

In the final part of manuscript, $SrTiO_3$ substrates with different crystal orientations are used to tune the strain in PVO films. Through x-ray diffraction and electron diffraction, it is observed that the PVO film has a quite smooth and parallel interface with the (110)-oriented STO (even without surface treatment), compared to other two orientations of the substrate, and allocated to the absence of polar discontinuity at the interface for the (110)-oriented STO substrate. All the films

have grown coherently, with cube-on-cube epitaxy with the substrates. On the magnetism front, first, a whopping enhancement of magnetization is observed by changing the substrate orientation between STO (001) and STO (111). Second, the easy axis of magnetization is successfully tuned from *out-of-plane* to *in-plane* direction of film by adopting (110)- and (111)-oriented STO substrates. A strong uniaxial *in-plane* magnetic anisotropy is also observed for the film grown on (110)-oriented STO substrates. This is explained by the unequal lattice mismatches along two in-plane directions of PVO, producing in-plane deformation of the octahedra, thus causing uniaxial anisotropy.

This material presents new properties thanks to the spin-orbit-lattice coupling, offering multiple outlooks to the spintronics community. Since, large compressive strain reduces exchange interactions in our films, our next step would be the examination of PVO films under extreme tensile strain, and try-out neutron diffraction for realizing new magnetic features, which would allow to construct a complete phase diagram of our films. After evidencing that different in-plane and out-of-plane magnetic anisotropies can be observed in our films, a more fine tuning of those properties would be more desirable. This can be achieved by using stacks of PVO with another material vanadate SrVO_3 (SVO), the so called superlattices, allowing complications of interfacial anisotropy. A further approach would also be to conduct MOKE experiments on the oriented films which remain untested at the moment.

Bibliography

- [1] J.M. Lock , Philos. Trans. R. Soc. London, Ser. A 208, 391 (1951).
- [2] J. W. Matthews and A. E. Blakeslee, J. Cryst. Growth 27, 118 (1974).
- [3] G. Rose, Ann. Phys. 48 (1839) 558.
- [4] Z. Cheng and J. Lin, CrystEngComm 12, 2646 (2010).
- [5] O. Muller, R. Roy, The Major Ternary Structural Families, Springer, New York-Heidelberg-Berlin, 1974.
- [6] J.H. Haeni, P. Irvin, W. Chang, R. Uecker, P. Reiche, Y.L. Li, S. Choudhury, W. Tian, M.E. Hawley, B. Craigo, A.K. Tagantsev, X.Q. Pan, S.K. Streiffer, L.Q. Chen, S.W. Kirchoefer, J. Levy, and D.G. Schlom, 430, 4 (2004).
- [7] A.P. Mackenzie, S.R. Julian, A.J. Diver, G.J. McMullan, M.P. Ray, G.G. Lonzarich, Y. Maeno, S. Nishizaki, and T. Fujita, Physical Review Letters 76, 3786 (1996).
- [8] M. Musa Saad H.-E., Materials Chemistry and Physics 204, 350 (2018).
- [9] J.C. Albornoz, D.A. Landínez Téllez, J. Roa-Rojas, J.A. Munévar, and E. Baggio-Saitovich, Journal of Superconductivity and Novel Magnetism 26, 2313 (2013).
- [10] J.B. Goodenough, Reports on Progress in Physics 67, 1915 (2004).
- [11] E. Dagotto, Science, New Series 309, 257 (2005).

- [12] Y. Ren, T.T.M. Palstra, D.I. Khomskii, E. Pellegrin, A.A. Nugroho, A.A. Menovsky, and G.A. Sawatzky, *Nature* 396, 441 (1998).
- [13] H. Uwe and T. Sakudo, *Physical Review B* 13, 271 (1976).
- [14] R. H. Mitchell, *Perovskites, Modern and Ancient*, Almaz Press (Thunder Bay), 2013.
- [15] A. S. Bhalla, R. Guo and R. Roy, *Mater. Res. Innovations*, 2000, 4, 3–26.
- [16] L. Goncalves-Ferreira, S.A.T. Redfern, E. Artacho, and E.K.H. Salje, *Physical Review Letters* 101, 097602 (2008).
- [17] A.M. Glazer, *Acta Crystallographica Section B Structural Crystallography and Crystal Chemistry* 28, 3384 (1972).
- [18] S. Miyasaka, Y. Okimoto, M. Iwama, and Y. Tokura, *Physical Review B* 68, 100406 (2003).
- [19] J. Fujioka, T. Yasue, S. Miyasaka, Y. Yamasaki, T. Arima, H. Sagayama, T. Inami, K. Ishii, and Y. Tokura, *Physical Review B* 82, 144425 (2010).
- [20] M. Reehuis, C. Ulrich, P. Pattison, B. Ouladdiaf, M.C. Rheinstädter, M. Ohl, L.P. Regnault, M. Miyasaka, Y. Tokura, and B. Keimer, *Physical Review B* 73, 094440 (2006).
- [21] Bersucker, I. et al. *The Jahn-Teller Effect: Fundamentals and Implications for Physics and Chemistry* Vol. 97 (eds. Köppel, H., Yarkony, D. R. & Barentzen, H.) (Springer, 2009).
- [22] J. Varignon, N.C. Bristowe, E. Bousquet, and P. Ghosez, *Scientific Reports* 5, 15364 (2015).
- [23] Q. Zhang, K. Singh, C. Simon, L.D. Tung, G. Balakrishnan, and V. Hardy, *Physical Review B* 90, 024418 (2014).
- [24] T. Sakai, G. Adachi, J. Shiokawa, and T. Shin-ike, *Journal of Applied Physics* 48, 379 (1977).

- [25] J.-S. Zhou, J.B. Goodenough, J.-Q. Yan, J.-G. Cheng, K. Matsubayashi, Y. Uwatoko, and Y. Ren, *Physical Review B* 80, 224422 (2009).
- [26] T. Sarkar, S.A. Ivanov, G.V. Bazuev, P. Nordblad, and R. Mathieu, *Journal of Physics D: Applied Physics* 48, 345003 (2015).
- [27] G.R. Blake, T.T.M. Palstra, Y. Ren, A.A. Nugroho, and A.A. Menovsky, *Physical Review Letters* 87, 245501 (2001).
- [28] *Introduction to Quantum Mechanics: David J. Griffiths* (2nd Edition).
- [29] *Introduction to Electrodynamics, David J. Griffiths* (3rd Edition).
- [30] *Introduction to Solid State Physics, Charles Kittel* (8th Edition).
- [31] *Introduction to Magnetic Materials, B. D. Cullity* (2nd Edition).
- [32] M. Onoda and H. Nagasawa, *Solid State Communications* 99, 487 (1996).
- [33] J. Fujioka, S. Miyasaka, and Y. Tokura, *Physical Review B* 72, 024460 (2005).
- [34] M. Reehuis, C. Ulrich, P.M. Abdala, P. Pattison, G. Khaliullin, J. Fujioka, S. Miyasaka, Y. Tokura, and B. Keimer, *Physical Review B* 94, 104436 (2016).
- [35] A. Ohtomo and H.Y. Hwang, *Nature* 427, 423 (2004).
- [36] N. Nakagawa, H.Y. Hwang, and D.A. Muller, *Nature Materials* 5, 204 (2006).
- [37] W. Choi, T. Sands, and K.-Y. Kim, *Journal of Materials Research* 15, 1 (2000).
- [38] Y. Hotta, H. Wadati, A. Fujimori, T. Susaki, and H.Y. Hwang, *Applied Physics Letters* 89, 251916 (2006).
- [39] H. Rotella, U. Lüders, P.-E. Janolin, V.H. Dao, D. Chateigner, R. Feyerherm, E. Dudzik, and W. Prellier, *Physical Review B* 85, 184101 (2012).

- [40] H. Rotella, O. Copie, G. Steciuk, H. Ouerdane, P. Boullay, P. Roussel, M. Morales, A. David, A. Pautrat, B. Mercey, L. Lutterotti, D. Chateigner, and W. Prellier, *Journal of Physics: Condensed Matter* 27, 175001 (2015).
- [41] O. Copie, H. Rotella, P. Boullay, M. Morales, A. Pautrat, P.-E. Janolin, I.C. Infante, D. Pravathana, U. Lüders, and W. Prellier, *Journal of Physics: Condensed Matter* 25, 492201 (2013).
- [42] O. Copie, J. Varignon, H. Rotella, G. Steciuk, P. Boullay, A. Pautrat, A. David, B. Mercey, P. Ghosez, and W. Prellier, *Advanced Materials* 29, 1604112 (2017).
- [43] L.D. Tung, *Physical Review B* 72, 054414 (2005).
- [44] J.H. Haeni, P. Irvin, W. Chang, R. Uecker, P. Reiche, Y.L. Li, S. Choudhury, W. Tian, M.E. Hawley, B. Craigo, A.K. Tagantsev, X.Q. Pan, S.K. Streiffer, L.Q. Chen, S.W. Kirchoefer, J. Levy, and D.G. Schlom, *Nature* 430, 4 (2004).
- [45] D. Sando, A. Barthélémy, M. Bibes, *Journal of Physics: Condensed Matter* 26, 473201 (2014).
- [46] M. Culo, M. Basletić, E. Tafra, A. Hamzić, S. Tomić, F. Fischgrabe, V. Moshnyaga, B. Korin-Hamzić, *Thin Solid Films* 631, 205 (2017).
- [47] J. Fontcuberta, *Comptes Rendus, Physique* 16, 204 (2015).
- [48] Y. Wang, W. Chen, B. Wang, and Y. Zheng, *Materials* 7, 6377 (2014).
- [49] D. Dijkkamp, T. Venkatesan, X.D. Wu, S.A. Shaheen, N. Jisrawi, Y.H. Min-Lee, W.L. McLean, and M. Croft, *Applied Physics Letters* 51, 619 (1987).
- [50] F. Laquai, P.E. Keivanidis, S. Balushev, J. Jacob, K. Müllen, and G. Wegner, *Applied Physics Letters* 87, 261917 (2005).
- [51] Broglie, L. (1928) "La nouvelle dynamique des quanta". *Electrons et Photons: Rapports et Discussions du Cinquième Conseil de Physique*, Solvay.

- [52] H. Topsoe, Semicond. Div., Bull. 472 (1968) 13.
- [53] M. Khalid, A. Setzer, M. Ziese, P. Esquinazi, D. Spemann, A. Pöpl, and E. Goering, Physical Review B 81, 214414 (2010).
- [54] J.M.D. Coey, M. Venkatesan, and P. Stamenov, Journal of Physics: Condensed Matter 28, 485001 (2016).
- [55] U. Aschauer, R. Pfenninger, S. M. Selbach, T. Grande, N. A. Spaldin, Physical Review B 88, 054111 (2013).
- [56] M.H. Sage, G.R. Blake, C. Marquina, and T.T.M. Palstra, Physical Review B 76, 195102 (2007).
- [57] J.A. Moyer, C. Eaton, and R. Engel-Herbert, Advanced Materials 25, 3578 (2013).
- [58] U. Aschauer, R. Pfenninger, S. M. Selbach, T. Grande, N. A. Spaldin, Physical Review B 88, 054111 (2013).
- [59] P. Agrawal, J. Guo, P. Yu, C. Hébert, D. Passerone, R. Erni, and M.D. Rossell, Physical Review B 94, 104101 (2016).
- [60] H. Rotella, O. Copie, A. Pautrat, P. Boullay, A. David, D. Pelloquin, C. Labbé, C. Frilay, and W. Prellier, Journal of Physics: Condensed Matter 27, 095603 (2015).
- [61] M.H. Sage, G.R. Blake, and T.T.M. Palstra, Physical Review B 77, 155121 (2008).
- [62] D.S. Schmool, N. Keller, M. Guyot, R. Krishnan, and M. Tessier, Journal of Magnetism and Magnetic Materials 195, 291 (1999).
- [63] S. Choudhury, Y.L. Li, L.Q. Chen, and Q.X. Jia, Applied Physics Letters 92, 142907 (2008).
- [64] O. Copie, H. Rotella, P. Boullay, M. Morales, A. Pautrat, P.-E. Janolin, I.C. Infante, D. Pravathana, U. Lüders, and W. Prellier, Journal of Physics: Condensed Matter 25, 492201 (2013).

- [65] O. Copie, J. Varignon, H. Rotella, G. Steciuk, P. Boullay, A. Pautrat, A. David, B. Mercey, P. Ghosez, and W. Prellier, *Advanced Materials* 29, 1604112 (2017).
- [66] D. Kumar, A. David, A. Fouchet, A. Pautrat, J. Varignon, C.U. Jung, U. Lüders, B. Domengès, O. Copie, P. Ghosez, and W. Prellier, *Physical Review B* 99, 224405 (2019).
- [67] S. Miyasaka, Y. Okimoto, M. Iwama, and Y. Tokura, *Physical Review B* 68, 100406 (2003).
- [68] T. Sarkar, S. A. Ivanov, G. V. Bazuev, P. Nordblad, R. Mathieu, *Journal of Physics D: Applied Physics* 48, 345003 (2015).
- [69] T. Sakai, G. Adachi, J. Shiokawa, T. Shinike, *Journal of Applied Physics* 48, 379 (1977).
- [70] Q. Zhang, K. Singh, C. Simon, L. D. Tung, G. Balakrishnan, V. Hardy, *Physical Review B* 90, 024418 (2014).
- [71] M. Reehuis, C. Ulrich, P. M. Abdala, P. Pattison, G. Khaliullin, J. Fujioka, S. Miyasaka, Y. Tokura, B. Keimer, *Physical Review B* 94, 104436 (2016).
- [72] A. Y. Borisevich, H. J. Chang, M. Huijben, M. P. Oxley, S. Okamoto, M. K. Niranjan, J. D. Burton, E. Y. Tsymbal, Y. H. Chu, P. Yu, R. Ramesh, S. V. Kalinin, S. J. Pennycook, *Physical Review Letters* 105, 087204 (2010).
- [73] H. Rotella, U. Lüders, P.-E. Janolin, V. H. Dao, D. Chateigner, R. Feyerherm, E. Dudzik, W. Prellier, *Physical Review B* 85, 184101 (2012).
- [74] J. M. Rondinelli, N. A. Spaldin, *Physical Review B* 82, 113402 (2010).
- [75] S. J. May, J.-W. Kim, J. M. Rondinelli, E. Karapetrova, N. A. Spaldin, A. Bhattacharya, P. J. Ryan, *Physical Review B* 82, 014110 (2010).
- [76] A. Vailionis, H. Boschker, W. Siemons, E. P. Houwman, D. H. A. Blank, G. Rijnders, G. Koster, *Physical Review B* 83, 064101 (2011).
- [77] D.S. Schmool, N. Keller, M. Guyot, R. Krishnan, and M. Tessier, *Journal of Applied Physics* 86, 5712 (1999).

- [78] J. Scola, P. Boullay, W. Noun, E. Popova, Y. Dumont, A. Fouchet, and N. Keller, *Journal of Applied Physics* 110, 043928 (2011).
- [79] J. Scola, W. Noun, E. Popova, A. Fouchet, Y. Dumont, N. Keller, P. Lejay, I. Sheikin, A. Demuer, and A. Pautrat, *Physical Review B* 81, 174409 (2010).
- [80] D. M. Korotin, V. V. Mazurenko, V. I. Anisimov, S. V. Streltsov, *Physical Review B* 91, 224405 (2015).
- [81] C.-J. Cheng, C. Lu, Z. Chen, L. You, L. Chen, J. Wang, and T. Wu, *Applied Physics Letters* 98, 242502 (2011).
- [82] S. Valencia, L. Balcells, B. Martínez, and J. Fontcuberta, *Journal of Applied Physics* 93, 8059 (2003).
- [83] P. Kaur, K.K. Sharma, R. Pandit, R.J. Choudhary, and R. Kumar, *Applied Physics Letters* 104, 081608 (2014).
- [84] O. Copie, H. Rotella, P. Boullay, M. Morales, A. Pautrat, P.-E. Janolin, I.C. Infante, D. Pravathana, U. Lüders, and W. Prellier, *Journal of Physics: Condensed Matter* 25, 492201 (2013).
- [85] R. Aeschlimann, D. Preziosi, P. Scheiderer, M. Sing, S. Valencia, J. Santamaria, C. Luo, H. Ryll, F. Radu, R. Claessen, C. Piamonteze, and M. Bibes, *Advanced Materials* 30, 1707489 (2018).
- [86] A. Fouchet, J.E. Rault, M. Allain, B. Bérini, J.-P. Rueff, Y. Dumont, and N. Keller, *Journal of Applied Physics* 123, 055302 (2018).
- [87] S. Liang, J.R. Sun, J. Wang, and B.G. Shen, *Applied Physics Letters* 95, 182509 (2009).
- [88] F. Wang, J. Zhang, P. Yuan, Q. Yan, and P. Zhang, *Journal of Physics: Condensed Matter* 12, 3037 (2000).

- [89] M.H. Sage, G.R. Blake, C. Marquina, and T.T.M. Palstra, *Physical Review B* 76, 195102 (2007).
- [90] O. Copie, J. Varignon, H. Rotella, G. Steciuk, P. Boullay, A. Pautrat, A. David, B. Mercey, P. Ghosez, and W. Prellier, *Advanced Materials* 29, 1604112 (2017).
- [91] M. Reehuis, C. Ulrich, K. Prokeš, S. Mat'aš, J. Fujioka, S. Miyasaka, Y. Tokura, and B. Keimer, *Physical Review B* 83, 064404 (2011).
- [92] M. Reehuis, C. Ulrich, P. Pattison, B. Ouladdiaf, M.C. Rheinstädter, M. Ohl, L.P. Regnault, M. Miyasaka, Y. Tokura, and B. Keimer, *Physical Review B* 73, 094440 (2006).
- [93] M. Reehuis, C. Ulrich, P. Pattison, M. Miyasaka, Y. Tokura, and B. Keimer, *The European Physical Journal B* 64, 27 (2008).
- [94] M. Reehuis, C. Ulrich, P.M. Abdala, P. Pattison, G. Khaliullin, J. Fujioka, S. Miyasaka, Y. Tokura, and B. Keimer, *Physical Review B* 94, 104436 (2016).
- [95] X. Zhou, Z. Wang, S. Ge, D. Wang, J. Yu, and D. Yao, *Physica Status Solidi (A)* 211, 2839 (2014).
- [96] F. Zhang, S. Ge, Z. Wang, X. Zhou, G. Wang, Z. Yu, and F. Li, *Journal of Alloys and Compounds* 506, 109 (2010).
- [97] D. Kumar, A. David, A. Fouchet, A. Pautrat, J. Varignon, C.U. Jung, U. Lüders, B. Domengès, O. Copie, P. Ghosez, and W. Prellier, *Physical Review B* 99, 224405 (2019).
- [98] H. Rotella, U. Lüders, P.-E. Janolin, V.H. Dao, D. Chateigner, R. Feyerherm, E. Dudzik, and W. Prellier, *Physical Review B* 85, (2012).
- [99] G. Herranz, F. Sánchez, N. Dix, M. Scigaj, and J. Fontcuberta, *Scientific Reports* 2, 758 (2012).
- [100] J. Chang, Y.-S. Park, and S.-K. Kim, *Applied Physics Letters* 92, 152910 (2008).
- [101] S. Sekiguchi, *Solid State Ionics* 108, 73 (1998).

- [102] J.L. Blok, X. Wan, G. Koster, D.H.A. Blank, and G. Rijnders, *Applied Physics Letters* 99, 151917 (2011).
- [103] E.J. Moon, B.A. Gray, A. Pimpinelli, M. Kareev, D. Meyers, and J. Chakhalian, *Crystal Growth & Design* 13, 2256 (2013).
- [104] S. Chen, M.G. Mason, H.J. Gysling, G.R. Paz-Pujalt, T.N. Blanton, T. Castro, K.M. Chen, C.P. Fictorie, W.L. Gladfelter, A. Franciosi, P.I. Cohen, and J.F. Evans, *Journal of Vacuum Science & Technology A: Vacuum, Surfaces, and Films* 11, 2419 (1993).
- [105] O.Yu. Gorbenko, S.V. Samoilentov, I.E. Graboy, and A.R. Kaul, *Chemistry of Materials* 14, 4026 (2002).
- [106] N.B. Uriev, *Russian Chemical Reviews* 73, 37 (2004).
- [107] D.J. Shu, F. Liu, and X.G. Gong, *Physical Review B* 64, 245410 (2001).
- [108] L. Huang, F. Liu, and X.G. Gong, *Physical Review B* 70, 155320 (2004).
- [109] A. Grutter, F. Wong, E. Arenholz, M. Liberati, A. Vailionis, and Y. Suzuki, *Applied Physics Letters* 96, 082509 (2010).
- [110] L.D. Tung, *Physical Review B* 72, 054414 (2005).
- [111] F. Tsui, M.C. Smoak, T.K. Nath, and C.B. Eom, *Appl. Phys. Lett.* 76, 2421 (2000).
- [112] J. Dho, Y.N. Kim, Y.S. Hwang, J.C. Kim, and N.H. Hur, *Appl. Phys. Lett.* 82, 1434 (2003).
- [113] H. Boschker, M. Mathews, E.P. Houwman, H. Nishikawa, A. Vailionis, G. Koster, G. Rijnders, and D.H.A. Blank, *Physical Review B* 79, 214425 (2009).

Chapter 6

ANNEX A

6.1 Calculation of uncertainty in the estimation of lattice constants

From Bragg's diffraction equation:

$$d = \frac{\lambda}{2 \sin \theta};$$

After differentiation on both sides,

$$\frac{\Delta d}{\Delta \theta} = \frac{\lambda}{2} \cdot \operatorname{cosec} \theta \cdot \cot \theta;$$

Then,

$$\frac{\Delta d}{d} = \cot \theta \cdot \Delta \theta;$$

This implies,

$$\Delta d = \frac{\Delta \theta}{\tan \theta} \cdot d$$

Here, Δd , and $\Delta \theta$ represent the error in lattice constant and error in the Bragg's angle (θ).